Backtracking potential mantle sources of North American kimberlites through kinematic models to constrain their origin

by

Esther Lee

B.S., California State University, Fullerton, 2019

A THESIS

submitted in partial fulfillment of the requirements for the degree

MASTER OF SCIENCE

Department of Geology
College of Arts and Sciences

KANSAS STATE UNIVERSITY
Manhattan, Kansas

2023

Approved by:

Major Professor
Claudia Adam

Copyright

Abstract

Kimberlites are relatively rare ultramafic igneous rocks that are most commonly emplaced on Archean cratons. However, in the North American continent they are widely distributed, including numerous occurrences within younger Proterozoic terranes. Several hypotheses have seen proposed to explain this widespread distribution: entrainment by mantle plumes, fluids derived from subducting slabs, large low shear velocity provinces, and edge-driven convection. In this study, we provide new constraints on North American kimberlite emplacement by backtracking the locus of their emplacement over time using GPlates software to make this reconstruction. We also consider constraints from mantle tomography models and lithosphere-asthenosphere boundary (LAB) models. We show that the youngest kimberlites (ages < 110 Ma) were emplaced through edge-driven convection, while the emplacement of older kimberlites (ages 110-660 Ma) can be accounted for by upwellings originating from LLSVPs. More precisely, kimberlites with ages between 110 and 300 Ma were emplaced over the Atlantic LLSVPs, while older kimberlites (ages 350-660 Ma) were emplaced over the Pacific LLSVPs. The backtracked locations of kimberlites in the Pacific display a westward increase in age. Such a pattern can be created by the drifting of the North America plate over the fixed mantle source and is therefore in agreement with the hypothesis that the emplacement of these kimberlites is related to LLSVPs.

Table of Contents

List of Figures

Acknowledgements

I thank Dr. Adam for your support, advice, and time for my research. I also thank Dr. Kempton for her advice and support. Lastly, I thank Dr. Goldberg for her comments and consistent support for me.

Dedication

I dedicate this Master's thesis to my family, who are living in California. I am thankful for their encouragement, as well, during my graduate studies.

Chapter 1 - Introduction

Kimberlites are volatile-rich ultramafic rocks that have been formed deep in the mantle (Golovin et al., 2018). They are alkaline and silica-poor (Francis and Patterson, 2009) and often carry diamonds and crustal and/or mantle xenoliths (Kopylova and Caro, 2004; Liu et al., 2018). Kimberlites normally form at depths greater than 150 km (Tappe et al., 2018). They form at high temperatures and pressures, but the proposed ranges in temperature and pressure vary according to the different authors. For example, according to Jollands et al. (2018), kimberlites can form at temperatures ranging from 1100-1300°C, whereas Stamm and Schmidt (2017), at temperatures of 1400-1650°C. Pressures at which kimberlite melts form range from 2.5 GPa according to Russell et al. (2012) to 8-10 GPa (Francis and Patterson, 2009).

Kimberlites are economically important for the diamonds that are found in them. Indeed, the name "kimberlite" comes from the town in South Africa called Kimberley where it was first mined for diamonds (Smit and Shirey, 2019). The presence of diamonds as inclusions indicate that kimberlite melts form within the field of diamonds stability of the mantle (Mitchell, 1991). Furthermore, diamonds are also associated with thick cratonic lithosphere, as they are interpreted to have formed at the base of the lithosphere within the asthenospheric mantle (Mitchell, 1991). Moreover, several studies on peridotite xenoliths entrained in kimberlites suggest that they are emplaced in regions associated with thick lithospheric mantle (150-200 km) (Kopylova and Caro, 2004; Golovin et al., 2018; Liu et al., 2018). Generally, kimberlites are found within Archaean cratons (Mitchell, 1991).

The emplacement of kimberlites on the North American continent is then puzzling. Models show that lithosphere thickness is 250 km under the northern North American craton, around 100-200 km in the central US, and reaches values of less than 100 km beneath the

western US (Artemieva, 2009) (Figure 1.1). These data were found using the lithosphere-asthenosphere boundary model of Artemieva (2009), which is based on thermal modeling using global statistical data and mantle temperatures, surface-wave seismic tomography, and body-wave seismic tomography. In addition, the emplacement of kimberlites is scattered across the continent (Figure 1.1). Kimberlite emplacements have been found in the Arctic Canada (such as Nunavut, and Northwest Territories), northern North American craton (such as Alberta and Saskatchewan), eastern North America (such as Ontario, Québec, New York, and Pennsylvania), central United States, and even in the western United States (such as Wyoming and Colorado). Thus, the distribution of the kimberlites shows that their emplacement is not exclusively associated with thick cratonic lithosphere.

In this project, we investigate the possible relationship between the kimberlite emplacement in the North American continent, and the underlying mantle structure and dynamics. We also investigate whether the structure of the lithosphere may affect kimberlite emplacements. We use kinematic models to backtrack the location of individual kimberlites at the time of their emplacements, i.e. the backtracked position shows the position today of the deep mantle that would have been directly beneath the kimberlite at its time of emplacement. We compare their locations with the character of that underlying mantle and lithosphere structure as we see it today.

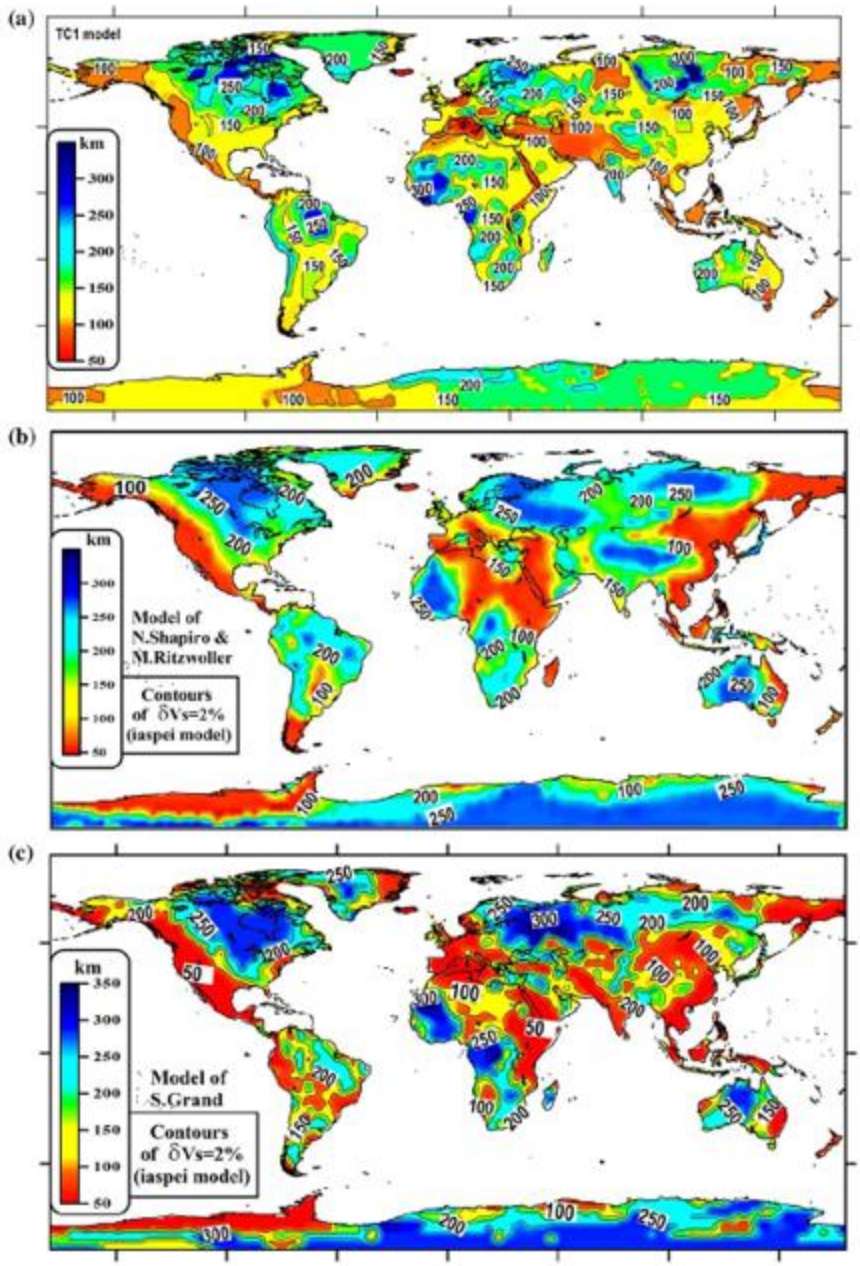

Figure 1.1. Thickness of the continental lithosphere.

a) Lithosphere thickness based on thermal modeling of mantle temperature. b) Lithosphere thickness based on surface-wave seismic tomography. c) Lithosphere thickness based on body-wave seismic tomography (from Artemieva, 2009).

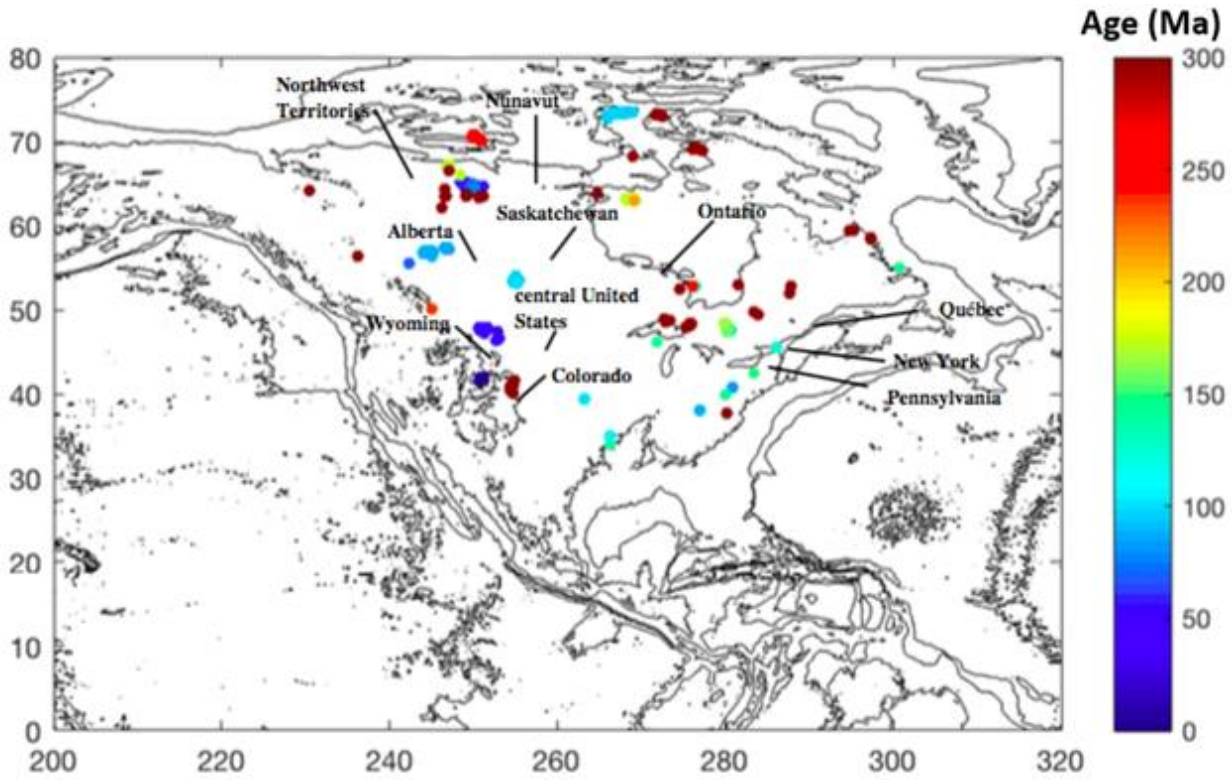

Figure 1.2. Ages of kimberlites, lamproites, melilitite and other types of ultramafic intrusions along the North American continent.

The color bar explains the colors of the plotted symbols, with ages in Ma (Faure et al., 2010).

Chapter 2 - Background

Several models have been proposed in the literature to account for kimberlite emplacement. Some of these models include hotspots (Heaman and Kjarsgaard, 2000; Heaman et al., 2003), fluids released by low-angle subduction (Currie and Beaumont, 2011), large low shear velocity provinces (LLSVP) (Davies et al., 2015), and edge-driven convection (EDC) (King and Anderson, 1998). In addition, petrological studies provide constraints on the formation of kimberlite melts. In the following, we provide a brief summary of the main previous results.

2.1. Previous models proposed for kimberlites emplacement

2.1.1. Mantle plumes

Heaman and Kjarsgaard (2000) hypothesize that kimberlites are entrained by mantle plumes. For example, according to Heaman and Kjarsgaard (2000), the emplacement of kimberlites in Rankin, Attawapiskat, and related locations in eastern Canada near the Hudson Bay is due to the Great Meteor plume (Figure 2.1). The authors note an obvious trend of an increasing age progression toward the Rankin Inlet, the northernmost part along the kimberlite occurrences. The linear increase in kimberlite ages in this region has lead other authors to propose that plumes may have facilitated the kimberlite emplacement (Crough, 1981; England and Houseman, 1984; Sleep, 1990). According to Crough et al. (1980) entrainment of kimberlites by plumes is an acceptable mechanism for the formation of these rocks, and they have shown this by inverting volcanic traces formed by three hotspots Great Meteor, Tristan da Cunha, and Trindade and reconstructing the kimberlite positions within 150 m.y. using hotspot reference frame. This hypothesis is agreed upon by Heaman and Kjarsgaard (2000) as kimberlites are formed deep in the mantle.

Figure 2.1. Great Meteor hotspot track and the emplacement of Rankin, Attawapiskat, and Kirkland Lake kimberlites (scenario proposed by Heaman and Kjarsgaard, 2000).

2.1.2. Subduction fluids

Other models state that the genesis of kimberlites is related to subduction processes. According to Currie and Beaumont (2011), subduction of the Farallon plate beneath the North American plate caused the lithosphere to be hydrated and therefore allowed partial melting to occur. The kimberlites in their study are in the Cretaceous kimberlite corridor in western North America (Figure 2.2). This region stretches roughly north-south for 1000-1500 km inland from the western edge of the North American continent (Currie and Beaumont, 2011). The Farallon

plate consisted of a thickened, low-angled oceanic crust, and due to fast subduction rates, it cooled the overlying continental lithosphere (Currie and Beaumont, 2011). Therefore, the kimberlites are emplaced as a result of dehydration and partial melting from the hydrated mantle (Currie and Beaumont, 2011).

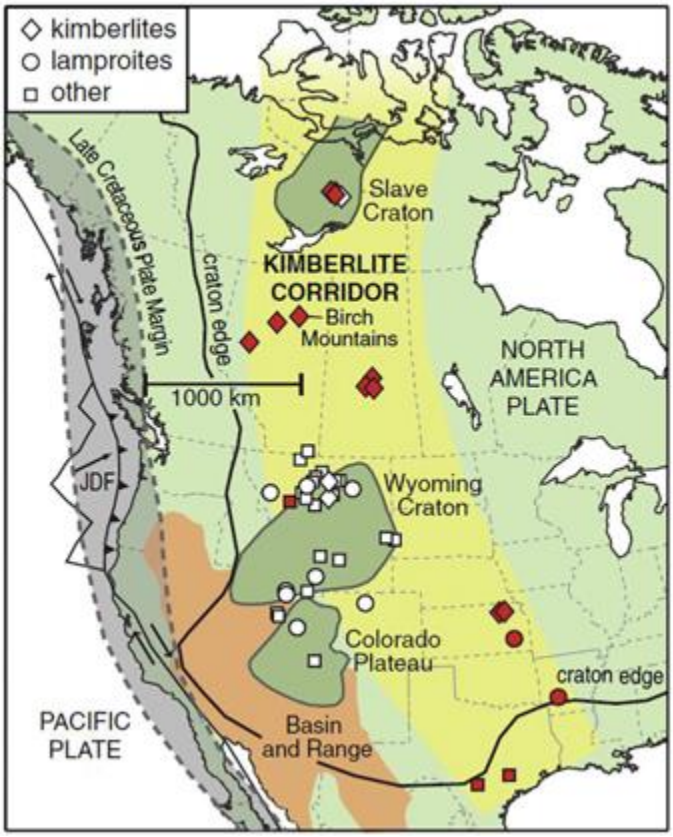

Figure 2.2. Kimberlite corridor and distribution of kimberlites, lamproites, and volcanics on the North American plate, with the possible location of the Juan de Fuca (JDF) plate. Red symbols indicate Cretaceous ages; white symbols indicate Cenozoic ages (Currie and Beaumont, 2011).

2.1.3. Large low shear velocity provinces (LLSVP)

Another hypothesis is that kimberlites originate in large low shear velocity provinces (LLSVP). LLSVPs are regions in the core-mantle boundary associated with slow seismic

velocities (Davies et al., 2015). Giuliani et al. (2020) and Torsvik et al. (2014) state that the location of kimberlites at the surface correlates with the LLSVPs locations. Both studies use GPlates, a software designed for implementing, visualizing and quantitatively taking into account the motion of tectonic plates (see section 3.3 for a detailed description). In Giuliani et al. (2020), the kimberlites are backtracked to a LLSVP in the eastern North Atlantic Ocean (Figure 2.3). Sr, Nd, and Hf ratios are used to show that kimberlites share common characteristics with the prevalent mantle (PREMA) and ocean-island basalts (OIBs) (Giuliani et al., 2020). Giuliani et al. (2020) say that kimberlites are the results of early Earth differentiation due to isotopic similarities with PREMA and thus that PREMA could be originated in the LLSVPs which may have formed during early this early Earth time period. Torsvik et al. (2014) also do a similar study as Giuliani et al. (2020), but they also provide a reference frame in the mantle that is corrected for the true polar wander.

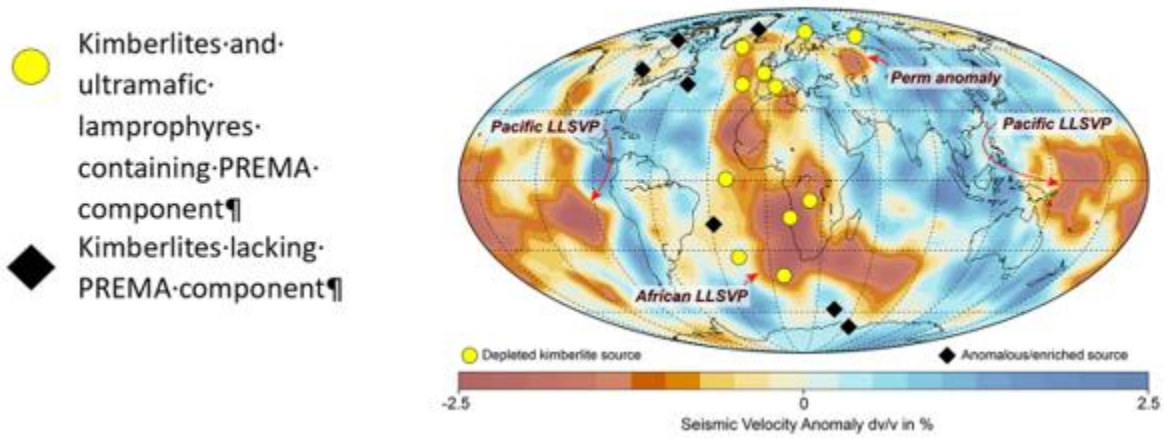

Figure 2.3. LLSVPs and the reconstructed locations of kimberlites by Giuliani et al. (2020) using rotation poles by Torsvik et al. (2014).

The colored bar shows seismic velocity anomalies. Red is for the lowest seismic velocity, and blue is the for the highest seismic velocity. Perm anomaly is the name for a small low shear velocity region in the Eurasian plate. Modified from Giuliani et al. (2020).

2.1.4. Edge-driven convection (EDC)

The transition from thick lithosphere to thin lithosphere generates a convection cell provided that the transition is not associated with a condition such as a subducting plate boundary. In edge driven convection, downwellings occur along thicker lithosphere, and upwellings occur beneath the thinner lithosphere (King and Anderson, 1998) (Figure 2.4). For example, such a pattern has been invoked to account for the emplacement of the Bermuda Rise, located 600 km from the eastern margin of the North American continent (King and Anderson, 1998). In another scenario, EDC's can be common at the boundary of the oceanic lithosphere and the continental lithosphere (Manjón-Cabeza Córdoba and Ballmer, 2021) (Figure 2.5). The model of edge-driven convection by Manjón-Cabeza Córdoba and Ballmer (2021) supposes that the strength of the magmatism caused by the EDC is relatively weak and can only sustain volcanism such as in the Canary Islands. In Ballmer et al. (2015), edge-driven convection is used to explain volcanism on the Colorado Plateau. According to Kempton et al. (2019), edge driven convection can account for the kimberlites emplacement in Kansas.

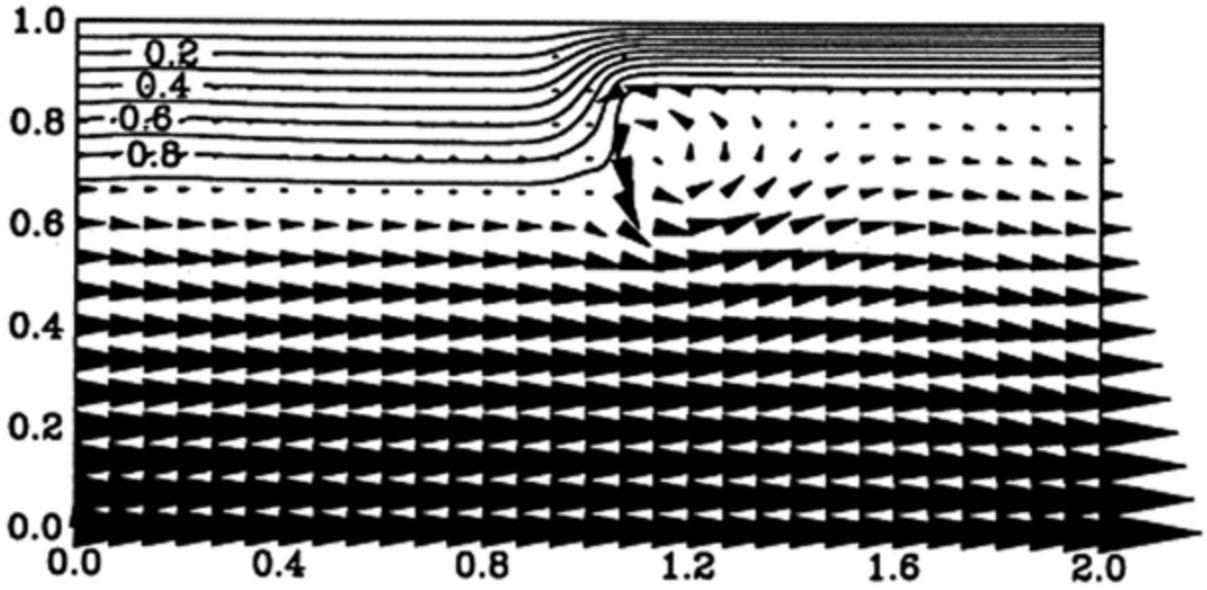

Figure 2.4. Model of flow fields (arrows) for edge-driven convection. Figure from King and Anderson (1998).

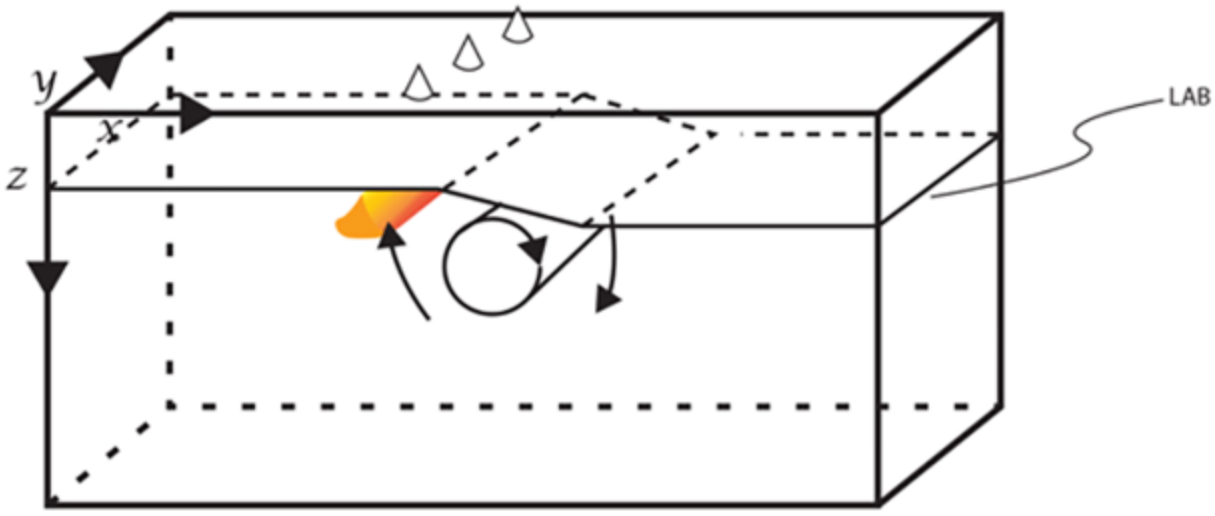

Figure 2.5. Model of edge-driven convection. The arrows represent the downwelling occurring along the thick continental lithosphere and the upwelling occurring along the thin oceanic lithosphere. Figure from Manjón-Cabeza Córdoba and Ballmer (2021).

2.2. Petrological and geochemical implications of the origins of kimberlite melts

2.2.1. Mineralogical geochemistry of kimberlites and the entrained xenoliths

Detailed petrological studies provide the mineralogy and the chemical components of the kimberlites. Kimberlite mineralogy includes olivine, phlogopite, calcite, apatite, and oxides (Golovin et al., 2018). They may also contain spinel, perovskite, and serpentine (Mitchell, 2008). A more general overview of the chemical nature of kimberlites is discussed in Francis and Patterson (2009). These authors discuss the carbonate and magnesian characteristics of kimberlites, which led these authors to suggest that they were sourced from the lithospheric mantle beneath the continental cratons. Francis and Patterson (2009) also propose that the high $Mg^{\#}$ in the kimberlites reflect the magnesian character of harzburgite in the lithospheric mantle, rather than the more fertile (lherzolitic) composition of asthenospheric mantle. ($Mg^{\#}$ is Mg/(Fe+Mg), and it shows the partitioning between Mg and Fe in the melt (Francis and

Pattersonn, 2009)). In addition, mantle xenoliths in kimberlites indicate the minimum pressures and temperatures at which the kimberlites formed (i.e. the kimberlites must have formed at greater pressures and temperatures than the xenoliths they entrain). For example, Liu et al. (2018) calculated a lithospheric mantle geotherm using clinopyroxenes from peridotite xenoliths entrained in kimberlites from Parry Peninsula and the Central Victoria Island in northern Canada. Their calculations suggest that the thicknesses of the lithosphere in the respective regions are 180 ± 20 km and 215 ± 30 km, respectively. Peridotite xenoliths from southeastern Slave Craton in Canada show by geobarometry that the magma formed beneath a 220- to 250-km-thick craton (Kopylova and Caro, 2004). Moreover, these studies show that chemical analyses of the peridotites reveal that this lithospheric mantle is depleted (Kopylova and Caro, 2004).

2.2.2. Evidence from Nd, Hf, and Sr isotopes

Many geochemical analyses of kimberlites suggest that kimberlites are either derived from or interacted with such depleted lithosphere. In contrast to earlier studies of the mineralogy of kimberlites and the xenoliths they entrain, several more recent studies based on Sr-Nd-Hf isotopic compositions show that the kimberlite parental melt must be derived from primitive mantle and/or in the convecting asthenosphere, e.g. Woodhead et al. (2019), Tappe et al. (2018), and Giuliani et al., (2020). Moreover, the isotopic analyses show that kimberlite melts are derived from a source that has undergone depletion. Derivation from by small degrees of partial melting of the convecting upper mantle in the asthenosphere just below the thick lithospheric cratons can explain the observations (Heaman et al., 2015; Tappe et al., 2014, 2017). This region below the thick lithospheric cratons can also be CO_2- and H_2O-rich, which provides the source of the volatiles of the kimberlite melts (Tappe et al., 2018). It is also where

redox reactions can occur and facilitate the generation of kimberlite melts through redox melting (Foley, 2011; Tappe et al., 2014; Yaxley et al., 2017).

As briefly mentioned in section 2.1.3, kimberlite Sr-Nd-Hf isotopic signatures are comparable to the hypothetical prevalent mantle (PREMA) (Figure 2.6). Figure 2.6 from Giuliani et al. (2020) shows the ranges of $^{143}Nd/^{144}/Nd$, $^{176}Hf/^{177}Hf$, and $^{87}Sr/^{86}Sr$ in ocean-island basalt and mid-ocean ridge basalts. According their study, PREMA has $^{143}Nd/^{144}Nd$ that range from ~0.5129 to 0.513 based on ocean island basalt samples (Zindler and Hart, 1986; Giuliani et al., 2020; Stracke et al., 2022). The graph in Figure 2.6 also show the field where PREMA and depleted kimberlite compositions lie on graphs (a) and (b). PREMA is a component in the mantle, and ocean-island basalts and mid-ocean ridge basalts show isotopic compositions of PREMA (Giuliani et al., 2020). The isotopic compositions of PREMA show that melts are derived from mixtures of depleted mantle that contains enriched components (such as EMI or EMII), but the melting dynamics reproducibly produce this averaged melt in the vicinity of PREMA (Stracke et al., 2022). In particular, kimberlites show that $^{143}Nd/^{144}Nd$ anomalies are small, and this could be explained by silicate differentiation in the Early Hadean. Furthermore, kimberlites are related to the locations of LLVSPs by plate reconstructions, and it can be hypothesized that the PREMA component is related to the LLSVPs (Giuliani et al., 2020).

Thus long-term and relatively stable depleted mantle structures can be responsible for the kimberlite melts (Tappe et al., 2014; Torsvik et al., 2014). In both Tappe et al. (2014) and Tappe et al. (2018), it is argued that low-degrees of partial melting beneath thick lithospheric cratons were induced by secular cooling after 2 Ga combined with increased CO_2 and H_2O concentrations in the shallow asthenosphere due to recycling of surficial sediments via subduction after 1.2 Ga. The mantle began to cool in the Archaean eon, and this is shown by

models of mantle temperatures that are dependent on redox conditions (Ganne and Feng, 2017; Tappe et al., 2018). According to Tappe et al. (2018), increasing velocities of the plates and the supercontinent cause the carbonate, volatile protokimberlite melts to move ascend through critical paths in the cratonic lithosphere due to the buoyancy of the depleted kimberlite melts and the pressure between the melt and the overlying lithosphere. The kimberlite melts ascend as swarms of dikes through the crust (Grégoire al., 2006; Tappe et al., 2014). The ascent of kimberlite melt as dikes can also be propelled by tensile stress in the crustal lithosphere (Wilson and Head, 2007; Barnett et al., 2013; Tappe et al., 2018). The latter of dikes penetrating through the crust and being instigated by tensile stress could have been triggered by the changing velocities when modern plate tectonics began to occur, and cycles of supercontinent have been related to the frequency of kimberlite emplacements such as the splitting of Pangaea in ~250 Ma (Tappe et al., 2014; Tappe et al., 2018). According to Tappe et al. (2014) and Flament (2010), modern plate tectonics began to occur around 3 Ga. Figure 2.6 shows how plate tectonics is related to the occurrence of kimberlite emplacements.

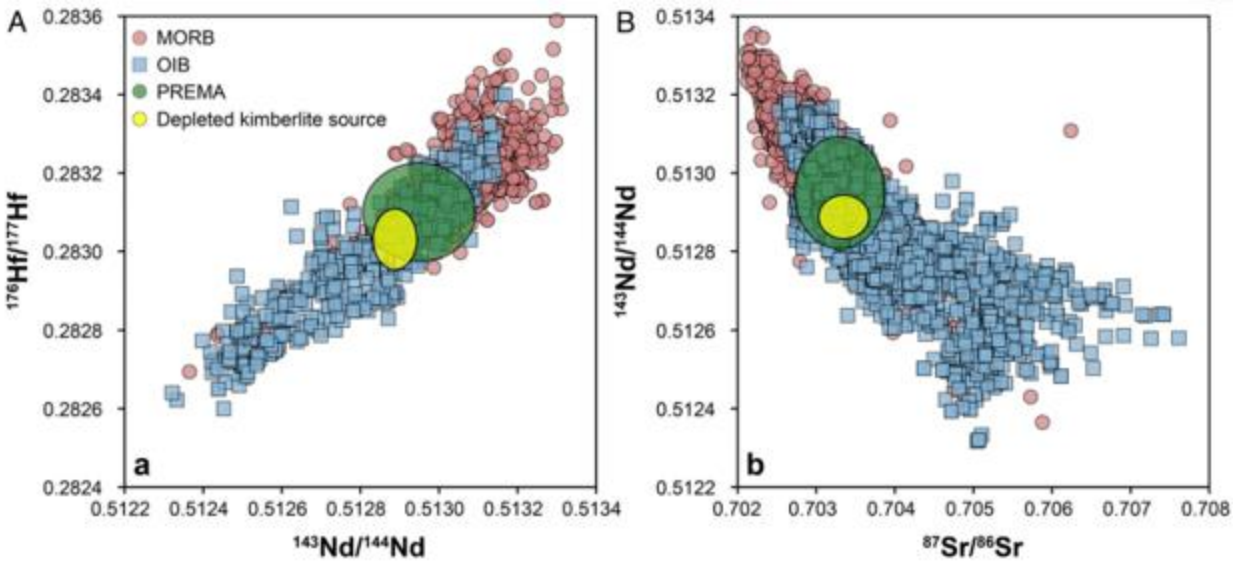

Figure 2.6. Graphs of (a) 143Nd/144/Nd vs 176Hf/177Hf and (b) 87Sr/86Sr vs. 143Nd/144Nd from Giuliani et al. (2020).

The blue squares and the red circles plot the isotopic compositions for mid-ocean ridge (MORB) and ocean island basalt (OIB) samples, respectively. The green ellipses indicate the field of isotopic compositions for PREMA, and the yellow ellipses indicate the field of isotopic compositions for the kimberlites in the study.

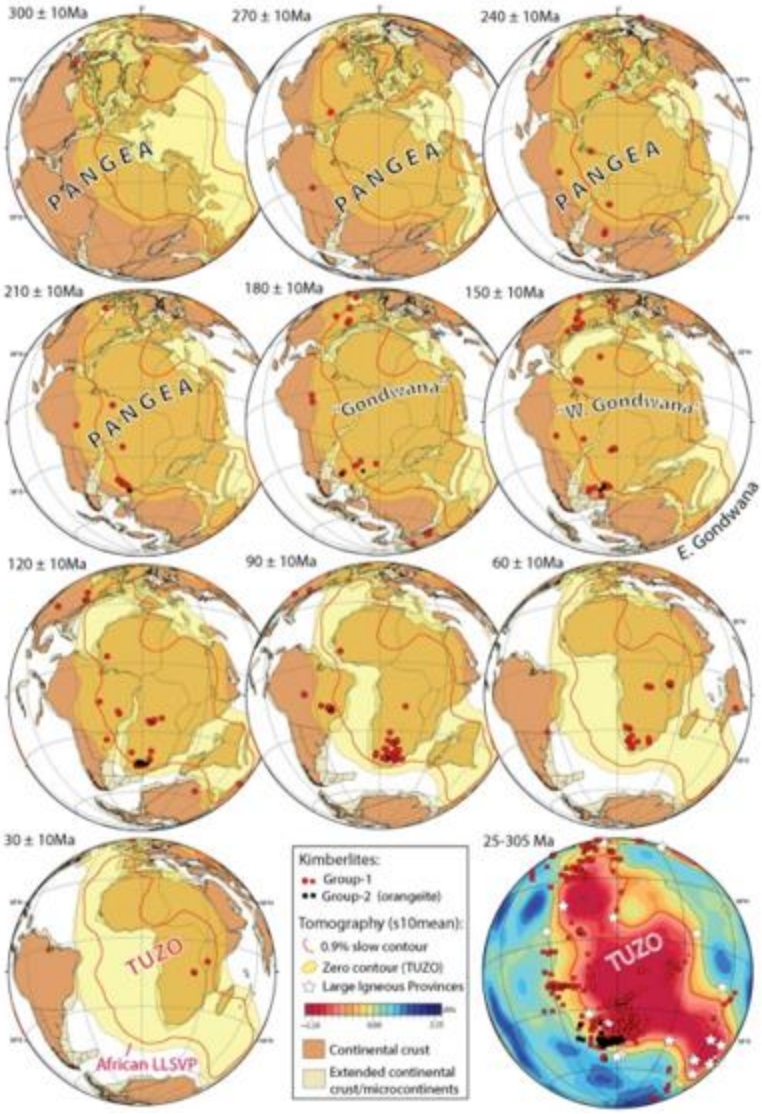

Figure 2.7. Kimberlites and plates reconstructed from 300±10-30±10 Ma using moving hotspot frame, true polar wander, and paleomagnetism (from Tappe et al., 2018).

The kimberlites and plates are reconstructed using Doubrovine et al. (2012) and Torsvik et al. (2012) plate rotation models. At 300±10 Ma, the model shows Pangaea as a stable supercontinent and the locations of two kimberlite clusters (red closed circles). As the plates are reconstructed to the present time, more clusters of kimberlites occur (red and black circles). The red line forming an irregular shape is the boundary and location of the African LLSVP, referred to as Tuzo (Burke, 2011). From 300±10-30±10 Ma, Pangaea splits into different plates, and the plates drifts farther away from each other. The last model shows kimberlites reconstructed for

ages 25-305 Ma (red and black squares) and the African LLSVP using a seismic tomography by Doubrovine et al. (2016).

Chapter 3 - Methods

In this project, we backtrack the locations of the kimberlites found on the North American continent to better constrain their origin. We use the ages and locations of kimberlites (Faure et al., 2010), and kinematic models (Muller et al., 2019; Young et al, 2019; Merdith et al., 2021).

3.1. Kimberlite locations and ages

One of the first tasks of this project was to make a database containing the locations and the ages of the kimberlites over the North American continent. Numerous articles focus on the petrology of kimberlites. They generally report the age of kimberlites but do not provide the precise locations (latitude and longitude). To obtain the data required for this project we contacted several authors who worked on the kimberlites located over the North American continent, including Larry Heaman, Richard Carlson, David Bailey, Claire Currie, and Christopher Beaumont. We found three articles that mentions the location of the kimberlites and integrated these in a database (Crough et al., 1980; Heaman and Kjarsgaard, 2000; Tappe et al., 2018). We also found a mining database (Faure et al., 2010) that compiles a large amount of information on the geospatial coordinates of the locations of the kimberlites throughout the world, including the North American plate. We provide the database of the locations of kimberlites in Appendix A. The location and ages of the kimberlites used in this study are reported in Figure 1.2.

3.2. Kinematic models, data, and reference frames

Kinematic models are those describe the present and past motion of the tectonic plates (Cox and Hart, 1986). In order to backtrack the kimberlite locations we used kinematic models. The design of kinematic models requires several datasets, including estimates of instantaneous

tectonic plate velocities from Global Positioning Systems (GPS), rates of seafloor spreading and azimuths of oceanic transform faults, earthquake slip directions, hotspot tracks, and plate boundaries (DeMets et al., 2010; Kreemer et al., 2014; Müller et al., 2019). Numerous kinematic models have been proposed in the literature (DeMets et al., 2010; Kreemer et al., 2014; Altamimi et al., 2016; Müller et al., 2019).

In this study we consider the kinematic models proposed by Merdith et al. (2021), Young et al. (2019), and Müller et al. (2019). Merdith et al. (2021) provide a kinematic model that reconstructs plate motions back to 1 Ga. It uses paleomagnetic data and geologic data, and thus incorporates a paleomagnetic reference frame by adding geologic data when available (Merdith et al, 2021). Paleomagnetic data are based on the positions of the continents with respect to the Earth's spin axis (Merdith et al., 2021). Paleomagnetic data give constraint to plate motions on a primary scale. The type of geologic data used by Merdith et al. (2021) is plate boundaries based on rifts and arcs. For plate motions before the Mesozoic, less geologic data on divergence, convergence, and transform movements are available, and more paleomagnetic data are used (Merdith et al., 2021). But for the Mesozoic and Cenozoic, more geologic data exist for plate motions and provide more accurate models for plate motions (Merdith et al., 2021).

Young et al. (2019) use both a paleomagnetic reference frame and a mantle reference frame. It reconstructs plate motions back to 410 Ma. For 70-0 Ma, it uses a hybrid reference frame assuming a moving hotspot frame. For ~90-70 Ma, it uses a hybrid reference frame using various absolute reference frames such as mantle reference frame and paleomagnetic reference frame by Müller et al. (2016), but corrects the stage rotations for the subduction dynamics in the period of the breakup of Gondwana. For 230-100 Ma, it uses a paleomagnetic reference frame

by Matthews et al. (2016). For 250-230 Ma, it uses a paleomagnetic reference frame by Domeier et al. (2012). For 410-250 Ma, it uses paleopoles combined with apparent polar wander paths by Torsvik and Van der Voo (2002). The geologic data that Young et al. (2019) use are closing plate boundaries and hotspot tracks.

Müller et al. (2019) reconstruct the motion of the lithospheric plates in the last 240 m.y. by integrating previous results of tectonic models and associated geological and geophysical data, and a joint global inversion using hot spot tracks for the last 80 m.y. Müller et al. (2019) also model the crustal deformation using geological strain markers, seismic refraction and reflection data, crustal thickness, paleomagnetic data, and thermochronology. Müller et al. (2019) attempt to approximate the deformation in the lithosphere by using an approach that involves pure shear, uniform extension, and compression. Because ductile deformation is difficult to input in plate reconstructions, they use the brittle property of the upper lithosphere to assume that the crust is deforming in kinematic small rigid blocks (Müller et al., 2019).

For the interpretation, we use only the model developed by Merdith et al. (2021), as it is the most recent one, and the model that allows us to extend our analysis farther back in time. Young and Müller are co-authors in Merdith et al. (2021).

3.3. Kinematic models and GPlates

GPlates is free software created by the EarthByte Project, Caltech, and Norwegian Geological Survey (Boyden et al., 2011). The version that is used for this project is GPlates 2.3. It is used to visualize the relative motions of tectonic plates, make models of plate motions, and reconstruct past plate motions (Boyden et al., 2011).

Polygons, lines, and points are used to shape the different landmasses and other features such as mid-ocean ridges and hotspots and are associated with their respective plates (Boyden et

al., 2011). The different plates are identified by unique plate ID's, which are numbers that represent the plates (Boyden et al., 2011). Each of the landmasses and features is assigned a plate ID number (Müller et al., 2018). GPlates also uses geometry files called GPML and GPMLZ to display the contours of landmasses (Müller et al., 2018). Polygons, lines, and points can be created directly on GPlates using the drawing tools (Müller et al., 2018).

GPlates incorporates the structure of rotation hierarchy to link motions of each plate to another (Boyden et al., 2011). A rotation hierarchy in modeling the motions of plates is a tree-like structure. One plate is at the top of the hierarchy structure and is fixed as a reference plate for other plates. Changing the rotation poles of the plates higher on the hierarchy changes the rotation components of all the plates that are coded as sublevels to the higher plate (Boyden et al., 2011). In this way, plates on the higher levels of the hierarchy are considered roots for the motions of plates at the lower levels. In general, large plates move relative to one another, and smaller plates move relative to the larger plates. The rotation poles that model the plate motions are written in rotation files (ROT) (Müller et al., 2018), and these include information on plate ID, ages in Ma, latitudes, longitudes, angles of rotation, fixed plate ID, and comments. The rotation files used in this research are by Merdith et al. (2021), Young et al. (2019), and Müller et al. (2019). With GPlates, we make point features representing the locations of kimberlites on the North American plate. The points are digitized and assigned to a plate ID of 101, which is the plate ID of the North American plate. GPlates allows an anchored plate to be selected for the reference plate (Boyden et al., 2011), and 0 is selected. The plate ID of 0 represents the absolute reference frame such as hotspots (Boyden et al., 2011). To create the point feature, the time of appearance is assigned to the point that corresponds to the age of the kimberlite at that location reported in the referred articles. Then the point feature is saved as a GPML file. The latitudes

and longitudes of the plotted point is recorded in GPlates (Figure 3.1). The point feature is used to export the positions that backtrack or reconstruct the location of the kimberlite from the present to a time of its origin in the past. These data are exported as GMT files that are in XY format (Müller et al., 2018) and include the latitude and longitude of each reconstructed point. The reconstructed points extracted from the GMT files are put together in a separate XY file containing the reconstructed points of a location of the kimberlite. Matlab (Matlab R2016b, Mathworks®) is used to plot the coordinates of the track modeled with GPlates on a bathymetry or topography map to allow visual comparisons between the modeled track and geological features.

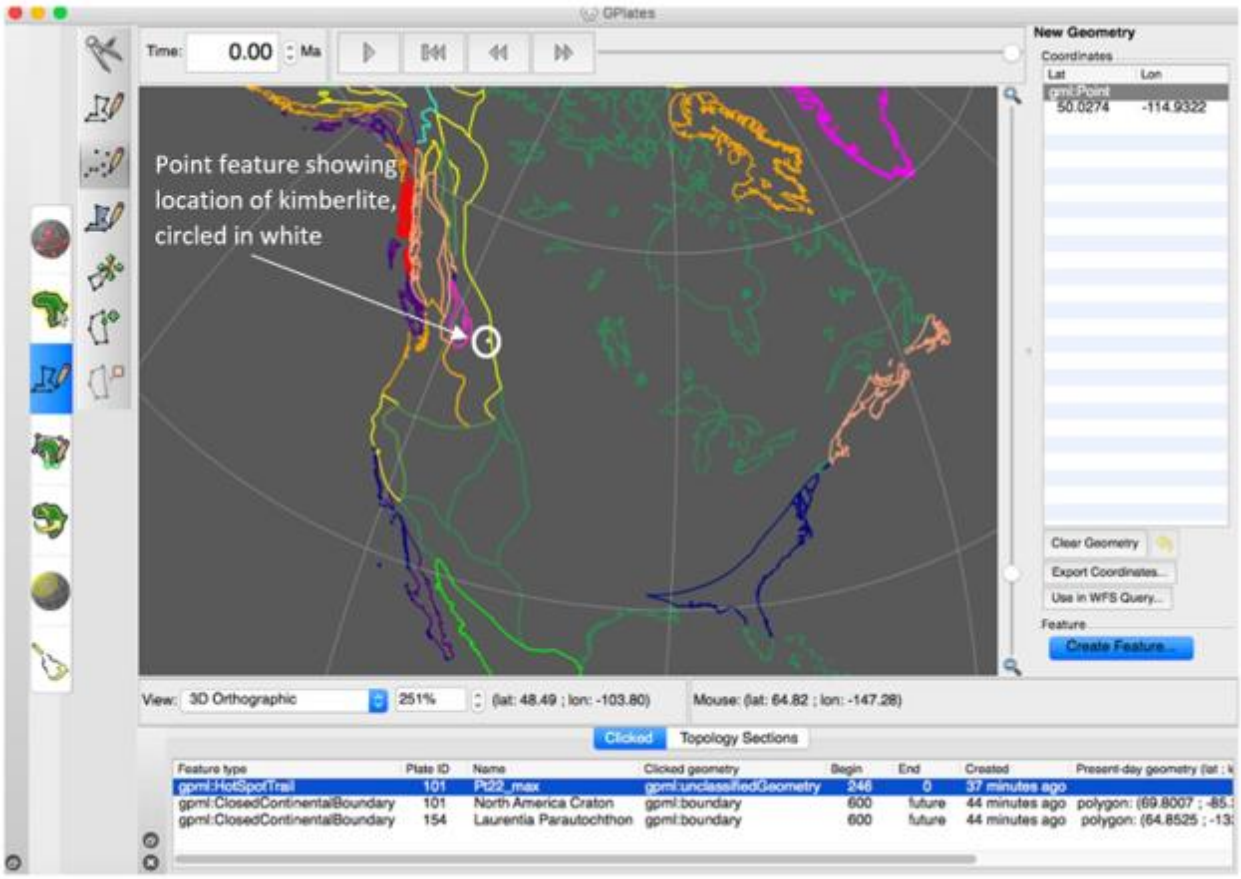

Figure 3.1. Digitizing coordinate location of kimberlite using the drawing tool in GPlates. The kimberlite is the white point feature (modified from GPlates 2.3, EarthByte, 2021). The lines displayed are outlines of the polygons of plates, and the different colors represent the different plates.

3.4. Trajectories design

We have reconstructed several kimberlite emplacements using the previously discussed models (Müller et al., 2019; Young et al., 2019; Merdith et al., 2021). The kimberlite trajectories are reconstructed with an increment of 1 m.y. and using the maximum ages from Faure et al. (2010). As an example, we display in Figure 3.2 the modeled trajectories while backtracking the position of the Victoria Island kimberlite, which is 273.8 Ma. The trajectories noticeably differ from each other. However, according to these models the backtracked location

falls in the vicinity of Madeira Islands, which is a hotspot chain (Ito and Vankeken, 2007). More precisely, the backtracked locations are within a 1000 km radius around Madeira Islands. In the results section (section 4), we will compare the results of these three models in more details.

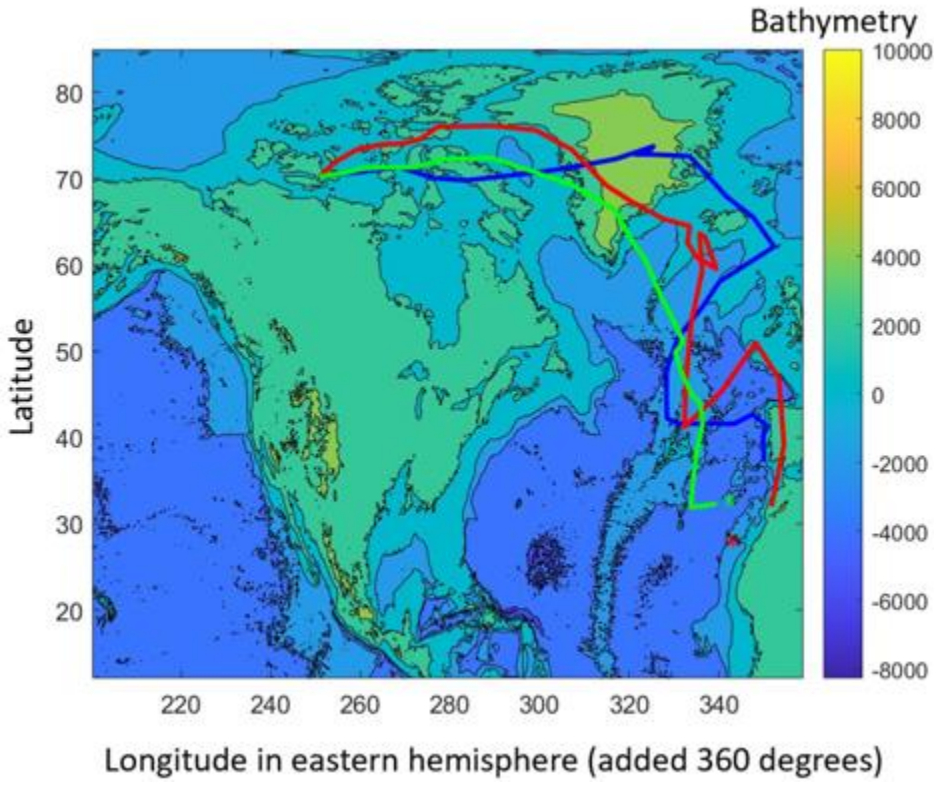

Figure 3.2. Trajectory of reconstruction of kimberlite emplacement.
Kimberlite trajectories computed with GPlates. The green line has been obtained using the model developed by Müller et al. (2019), the red line using the model developed by Merdith et al. (2021), and the blue line using the model developed by Young et al. (2019). The green asterisk shows the Madeira Islands, and the red asterisk shows the Canary Islands. The colored map is the bathymetry/topography (data from Tozer et al., 2019). In this kimberlite reconstruction, the age of the kimberlite is 273.8 Ma, and it is located at 70.199 N 109.146 W (Faure et al., 2010). Figure designed with Matlab (Matlab R2016b, Mathworks®)

3.5. Geophysical data

Lastly, we incorporate geophysical data in our study. In particular, we use seismic tomography models and models assessing the lithosphere-asthenosphere boundary (LAB).

3.5.1. Tomography models

Seismic tomography models provide the 3D structure of the Earth in terms of seismic velocity anomalies, *dvs*. To investigate whether the kimberlite emplacement may be related to specific mantle sources, such as the LLSVPs, we study the correlation between the reconstruction of kimberlite sources and mantle structure. Two tomography models have been considered in this study: SEMUCB-WM1 (French and Romanowicz, 2014) and SAVANI (Auer et al., 2014). We have developed several Matlab (Matlab R2016b, Mathworks®) programs to study these correlations (see Appendix C for an example of a Matlab script for SEMUCB-WM1).

3.5.2. Lithosphere-asthenosphere boundary (LAB)

Several models describe the lithosphere-asthenosphere boundary. LAB's show the depths to the boundary between the lithosphere and the asthenosphere (Artemieva, 2009). We used the CAM2016 (Priestley et al., 2018) and LITHO1.0 (Pasyanos et al., 2014) models. CAM2016 (Priestley et al., 2018) uses waveforms extracted from seismic data. LITHO1.0 (Pasyanos et al., 2014) uses data from surface wave dataset of dispersion measurements. We are taking the gradient of the LAB. We have developed several Matlab (Matlab R2016b, Mathworks®) programs to process these data (see Appendices D, E, F, and G).

Chapter 4 - Results

4.1. Backtracked kimberlite locations

The backtracked kimberlite locations are displayed in Figure 4.1. We use the kimberlite ages published by Faure et al. (2010), and the rotation poles designed by Merdith et al. (2021). Although several kinematic models have been proposed, as discussed in Chapter 3, the model developed by Merdith et al. (2021) is one of the most recent models. It is an update of other recent and widely used models (e.g., Young et al., 2019, Müller et al., 2019). Therefore, in Chapters 4 and 5, we discuss the results obtained with the model developed by Merdith et al. (2021). In appendix B, we show a comparison between the backtracked kimberlite locations using several other recent kinematic models (i.e. Young et al., 2019 and Müller et al., 2019). The kinematic model designed by Merdith et al. (2021) is the model that allows us to go the farthest back in time. It allows us to reconstruct the tectonic plate motions during the last 1,000 Ma. The oldest kimberlites emplaced over the North American continent are about 660 Ma (Faure et al., 2010), (Figure 4.1). In Figure 4.2 we report the backtracked kimberlite locations, as well as the present-day location of kimberlites. These two locations are connected by a black line.

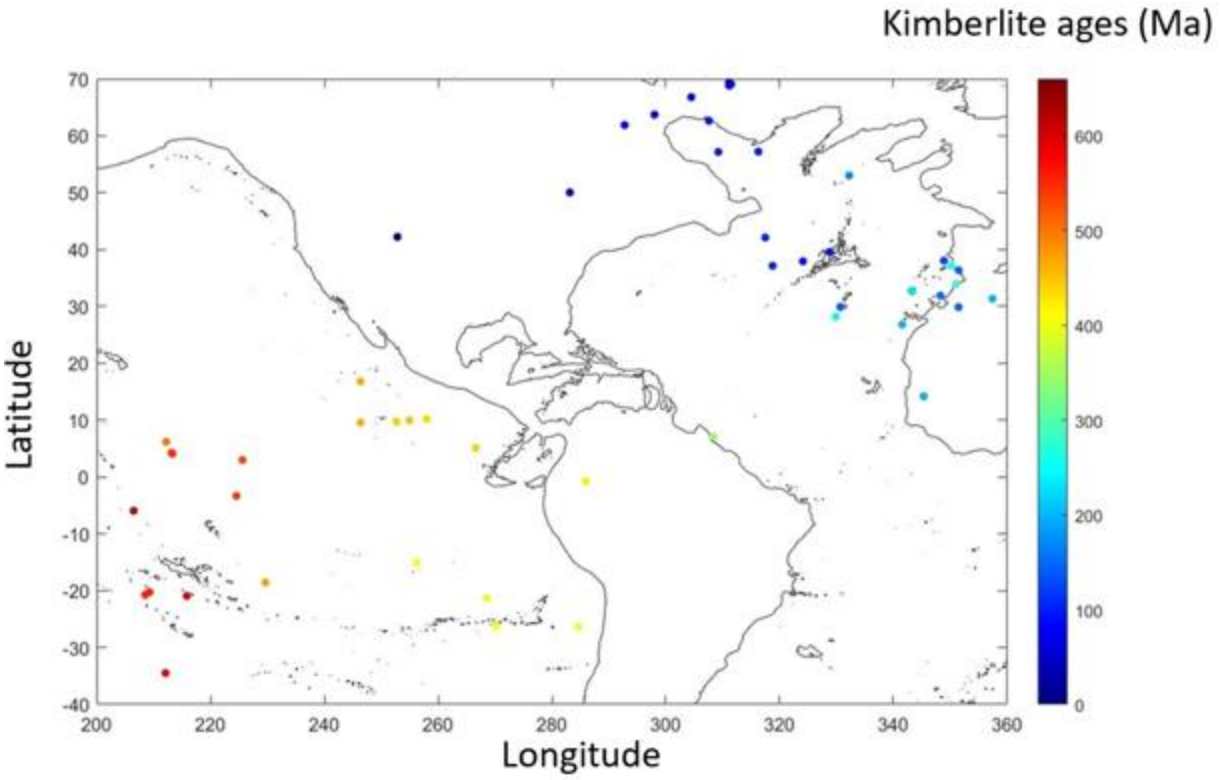

Figure 4.1. Backtracked kimberlite locations computed with the rotation poles of Merdith et al. (2021).

The computation has been done with the GPlates software (GPlates 2.3, EarthByte, 2021). The kimberlite ages are taken from Faure et al. (2010), and vary between 0 and 660 Ma.

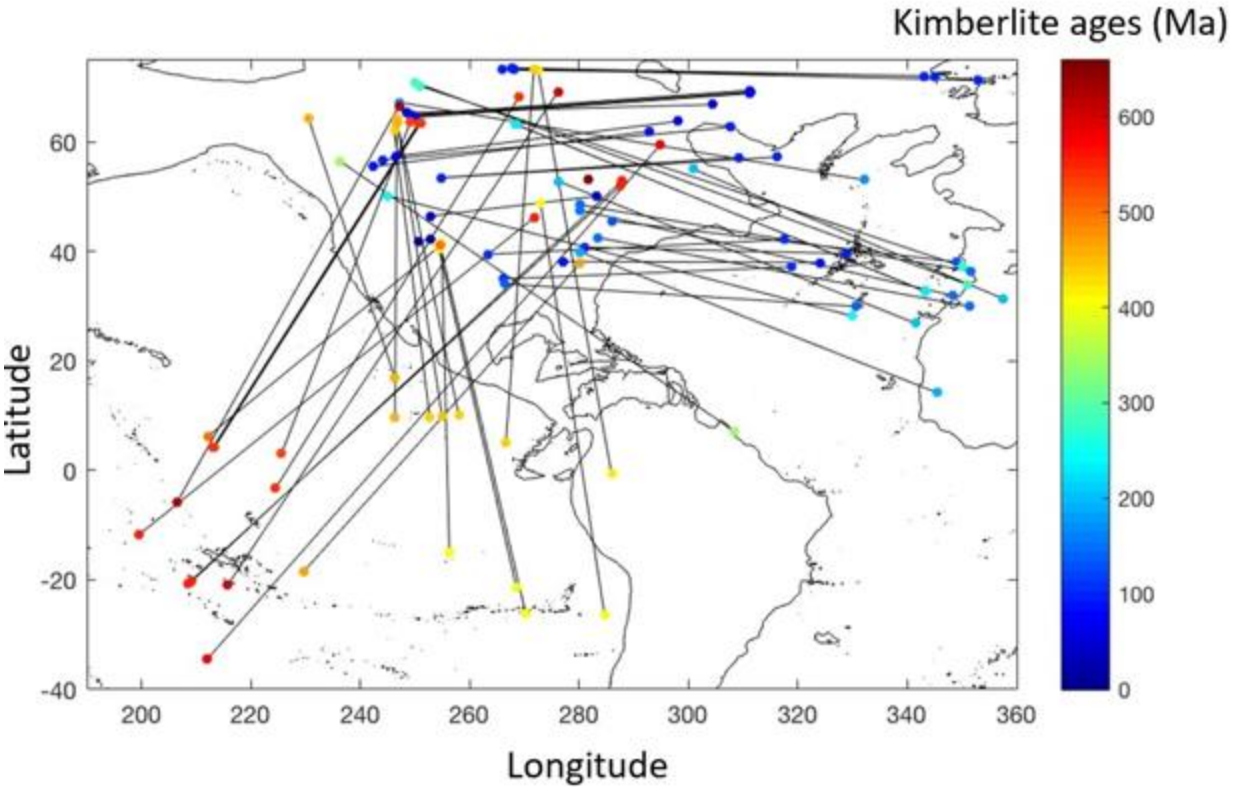

Figure 4.2. Present-day and backtracked kimberlite locations over the North American continent.

The kimberlite ages are taken from Faure et al. (2010). The backtracked locations have been computed with the rotation poles of Merdith et al. (2021) and GPlates software. The present-day and backtracked locations are connected by a black line.

4.2. LLSVP and backtracked kimberlite locations

We investigate the relationship between the backtracked kimberlite locations and the large low shear velocity provinces (LLSVP). The LLSVPs are found at the base of the lower mantle, near the core-mantle boundary (Davies et al., 2015). We use two tomography models to investigate this correlation: the SEMUCB-WM1 model, developed by French and Romanowicz (2014), (Figure 4.3), and the SAVANI model, developed by Auer et al. (2014) (Figure 4.4).

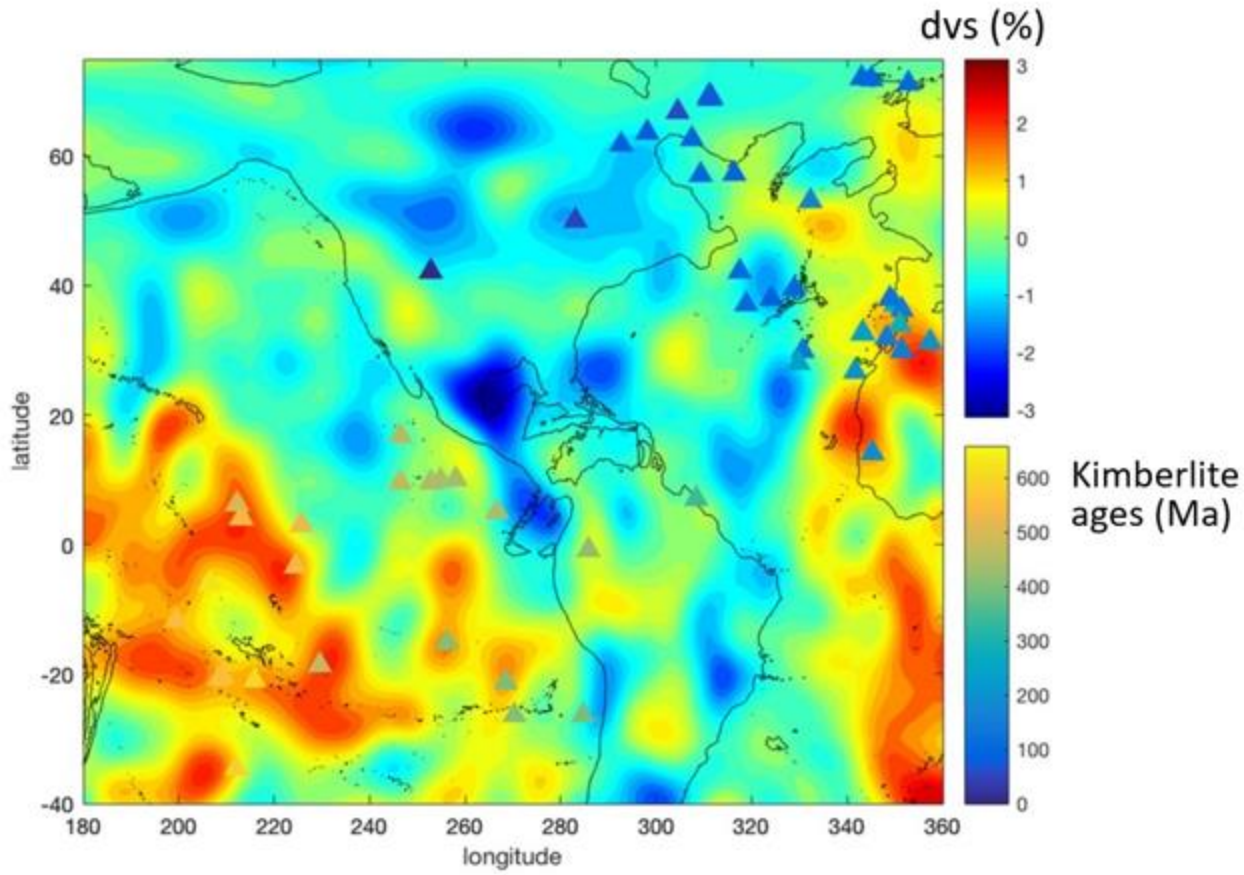

Figure 4.3. LLSVPs constrained with the SEMUCB-WM1 tomography model (French and Romanowicz, 2014) and backtracked kimberlite locations.

The colored map represents the seismic velocity anomaly, *dvs,* at depth ~2800 km. The kimberlite ages are taken from Faure et al. (2010). The backtracked locations have been computed with the rotation poles of Merdith et al. (2021) and GPlates software. The backtracked locations are reported as triangles, the color of which represents the ages of the kimberlites.

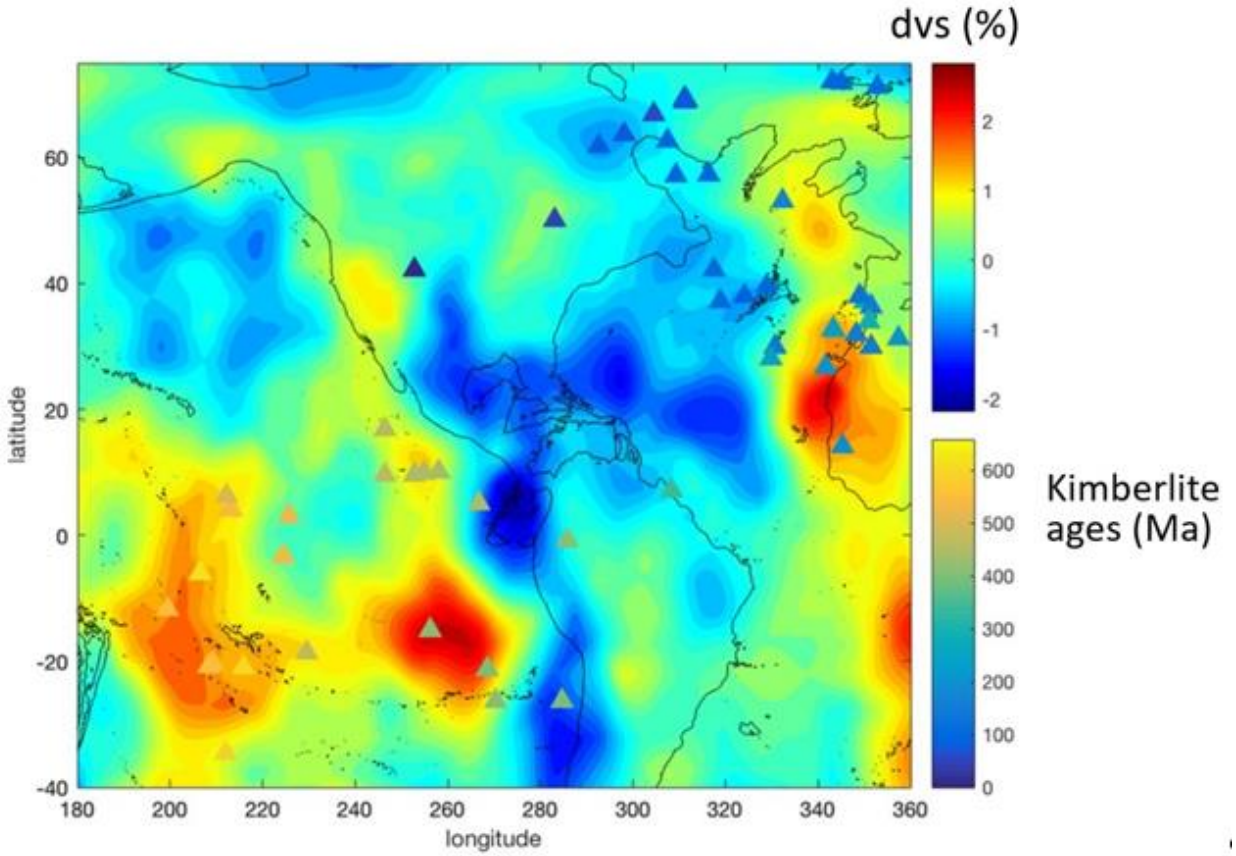

Figure 4.4. LLSVPs constrained with the SAVANI tomography model (Auer et al., 2014) and backtracked kimberlite locations.

The colored map represents the seismic velocity anomaly, *dvs*, at depth ~2800 km. The kimberlite ages are taken from Faure et al. (2010). The backtracked locations have been computed with the rotation poles of Merdith et al. (2021) and GPlates software. The backtracked locations are reported as triangles, the color of which represents the ages of the kimberlites.

4.3. LAB, LAB gradients, and present-day kimberlite locations

We investigate the relationship between the lithosphere-asthenosphere boundary (LAB) and the present-day kimberlite locations. Two LAB models have been considered in this study: the CAM2016 model, developed by Priestley et al. (2018),(Figure 4.5), and the LITHO1.0 model, developed by Pasyanos et al. (2014) (Figure 4.6). CAM2016 uses waveforms extracted

from seismic data and LITHO1.0 uses data from surface wave dataset. As discussed in Chapter 2, according to some authors, the edge-driven convection (EDC), induced from transition from thick lithosphere to thin lithosphere, may account for kimberlites and/or other types of volcanic emplacements (e.g., King and Anderson, 1998; Kempton et al., 2019; Manjón-Cabeza Córdoba and Ballmer, 2021). To investigate this hypothesis, we also examine the correlation between the present-day kimberlite locations and the LAB gradient (Figures 4.7 and 4.8).

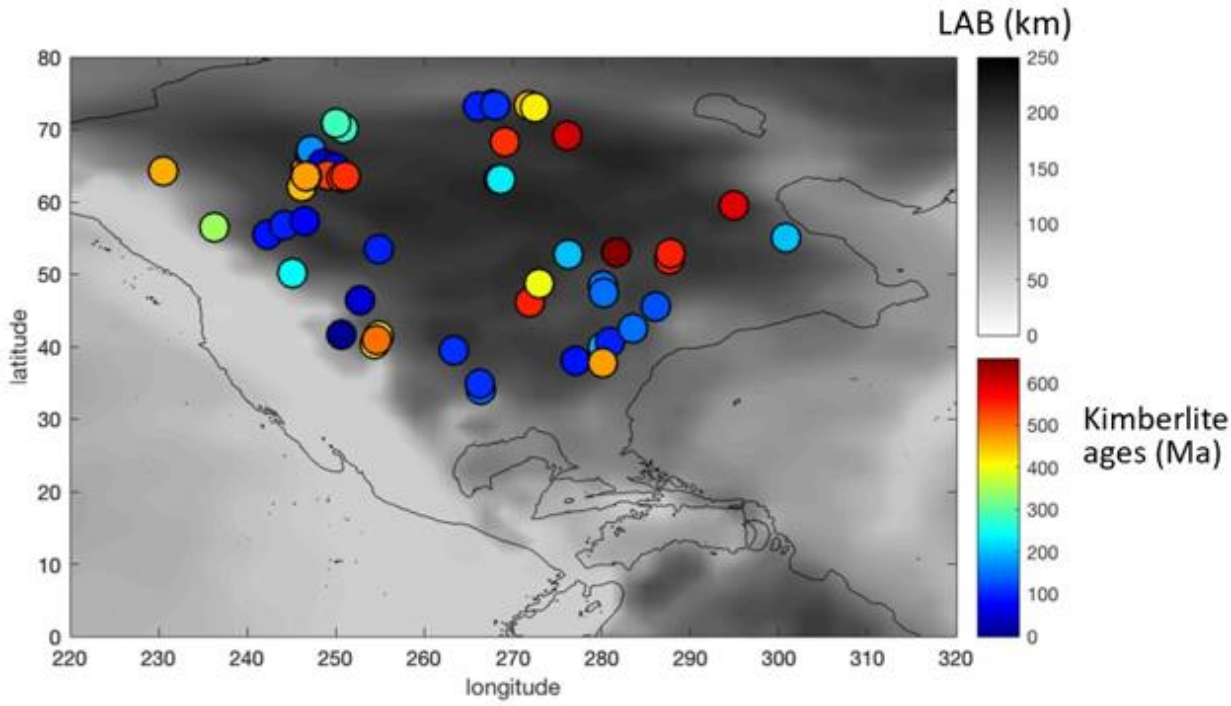

Figure 4.5. CAM2016 LAB and present-day locations of kimberlites.
The black and white map represents the LAB according to the CAM2016 model (Priestley et al., 2018). The circles show the positions and ages of the North American kimberlites (data from Faure et al., 2010).

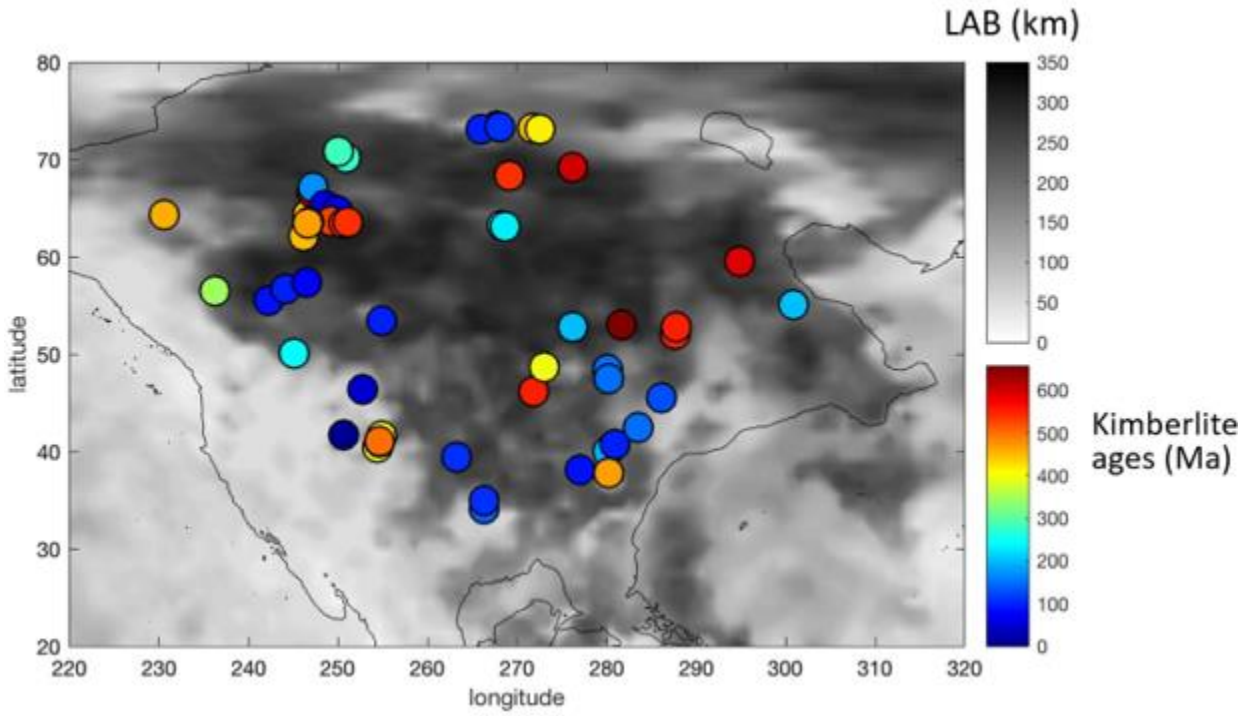

Figure 4.6. LITHO1.0 LAB and present-day locations of kimberlites.

The black and white map represents the LAB according to the LITHO1.0 model (Pasyanos et al., 2014). The circles show the positions and ages of the North American kimberlites (data from Faure et al., 2010).

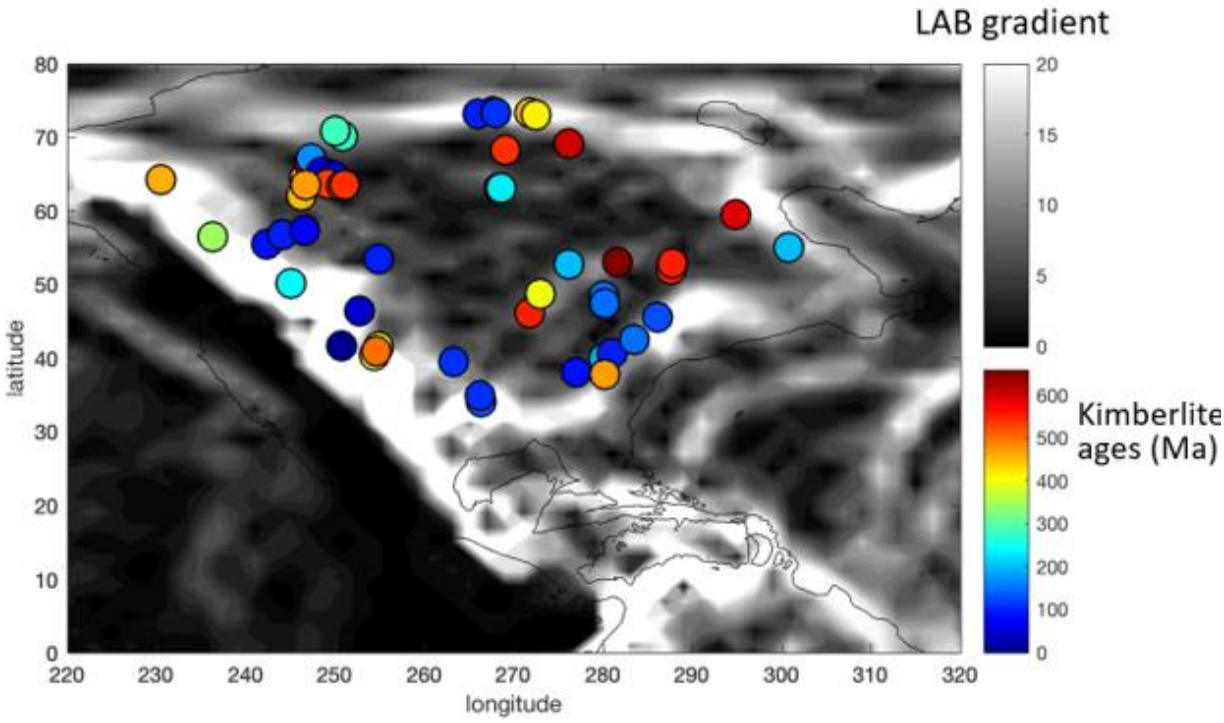

Figure 4.7. Gradient of LAB according to the CAM2016 model, and present-day locations of kimberlites.

The black and white map represents the LAB gradient while considering the LAB provided by the CAM2016 model (Priestley et al., 2018). LAB gradient is the derivative of the depths to the lithosphere-asthenosphere boundary with respect to the x-axis or the longitudinal axis. Therefore, it has no units as the derivatives are taken for the depths (km) with respect to the horizontal distance (km). The circles show the positions and ages of the North American kimberlites (data from Faure et al., 2010).

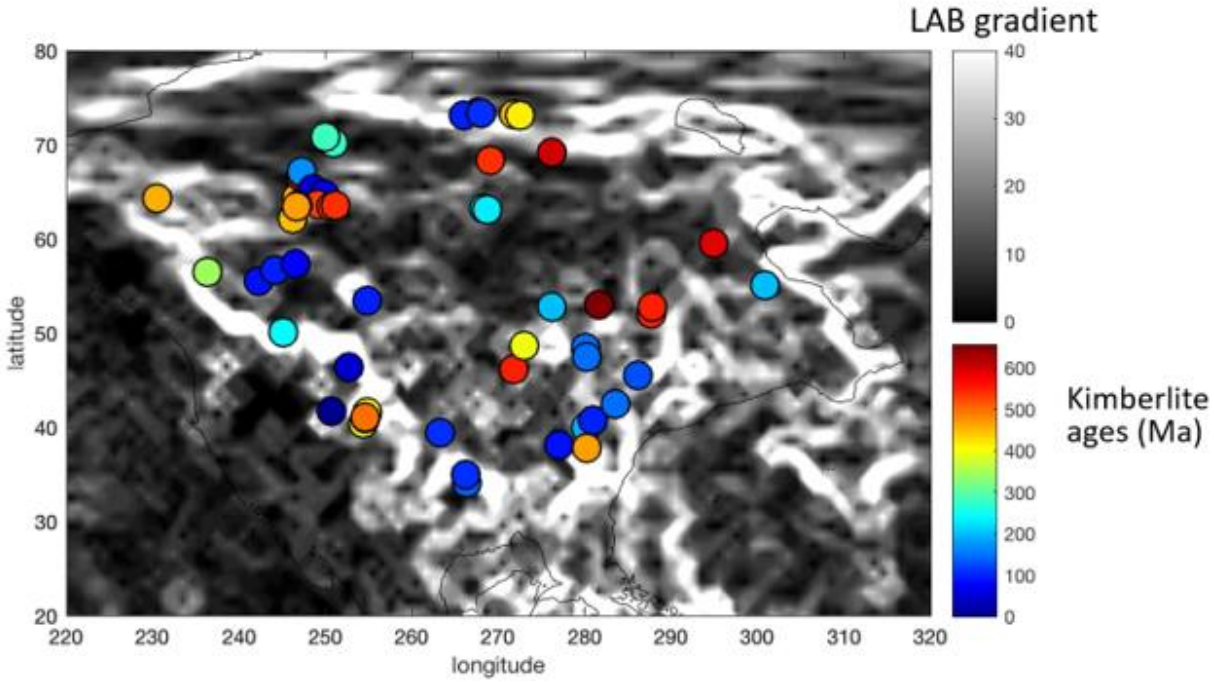

Figure 4.8. Gradient of LAB according to the LITHO1.0 model, and present-day locations of kimberlites.

The black and white map represents the LAB gradient while considering the LAB provided by the LITHO1.0 model (Pasyanos et al., 2014). The circles show the positions and ages of the North American kimberlites (data from Faure et al., 2010).

Chapter 5 - Discussion

In this chapter we discuss our results and interpret them in the context of hypotheses for the origins of kimberlites previously discussed in the literature.

5.1. Spatio-temporal distribution of backtracked kimberlite locations

The kimberlite ages and locations considered in this study are displayed in Figure 5.1. The data are extracted from the Faure et al. (2010) database. The figure also shows the names of the regions, states, and localities where these kimberlites occur. The backtracked and present-day positions are reported in Figures 5.2 to 5.6. We have identified five distinct periods in which the backtracked kimberlite locations display different patterns. Each period is displayed in a separate figure below: 0-110 Ma (Figure 5.2), 110-300 Ma (Figure 5.3), 300-350 Ma (Figure 5.4), 350-620 Ma (Figure 5.5), and 620-660 Ma (Figure 5.6).

The backtracked positions of the young kimberlites (ages < 110 Ma) are on the location where the Atlantic Ocean basin currently lies, and also where the North American plate currently lies (Figure 5.2). These kimberlites occur in Montana, Wyoming, Kansas, Arkansas, Kentucky, Pennsylvania, Alberta, Saskatchewan, Slave Craton, and Somerset Island. The kimberlites with ages between 110 and 300 Ma were emplaced on the North American continent when this continent was located over the present-day location of the North Atlantic 110-300 my ago. Specifically, this area lies in the regions in the Atlantic Ocean, west of the Mid-Atlantic Ridge, and on the westernmost part of the continental Eurasian and African plates (Figure 5.2). These 110 to 300 Ma old kimberlites are found in Cranbrook, British Columbia; Victoria Island; Slave Craton; Rankin Inlet; Newfoundland/Labrador; Lake Abitibi; Lake Timiskaming; Attawapiskat; New York; and Pennsylvania (Figure 5.1). Between ages 300 and 350 Ma, there seems to be a quiet period, as only one sample from the Faure et al. (2010)

database is found in this age range. This sample is from the Ospika pipe region in British Columbia, and its backtracked position is Northern Brazil (Figure 5.4). As this sample appears to be unique to this time period, we have investigated its origin in more detail. According to Pell and Ijewliw (2003), this sample is actually not a kimberlite but an ultramafic lamprophyre. We, therefore, do not consider this sample further. For ages 350-620 Ma, the backtracked kimberlite locations associated with the mantle that was underneath the North American continent when the North American continent was over the location of the present-day Pacific Ocean (Figure 5.5). Present-day locations of kimberlites in this age group occur all over the North American continent (e.g., Slave Craton, Wyoming, Colorado, Lake Ellen area in Michigan, and Brodeur Peninsula in Baffin Island). We have only one sample with an age greater than 620 Ma (Figure 5.6). This 658-Ma kimberlite is found in Wemindji adjacent to the east side of Hudson Bay, and its backtracked location was on the North American continent when the continent was over the mantle as it interacted with this lithosphere which was at a geographical location where the Australian plate now resides.

To better understand the phenomena at the origin of these kimberlite emplacements, we investigate the correlation between the kimberlites' backtracked locations and the positions of the LLSVPs.

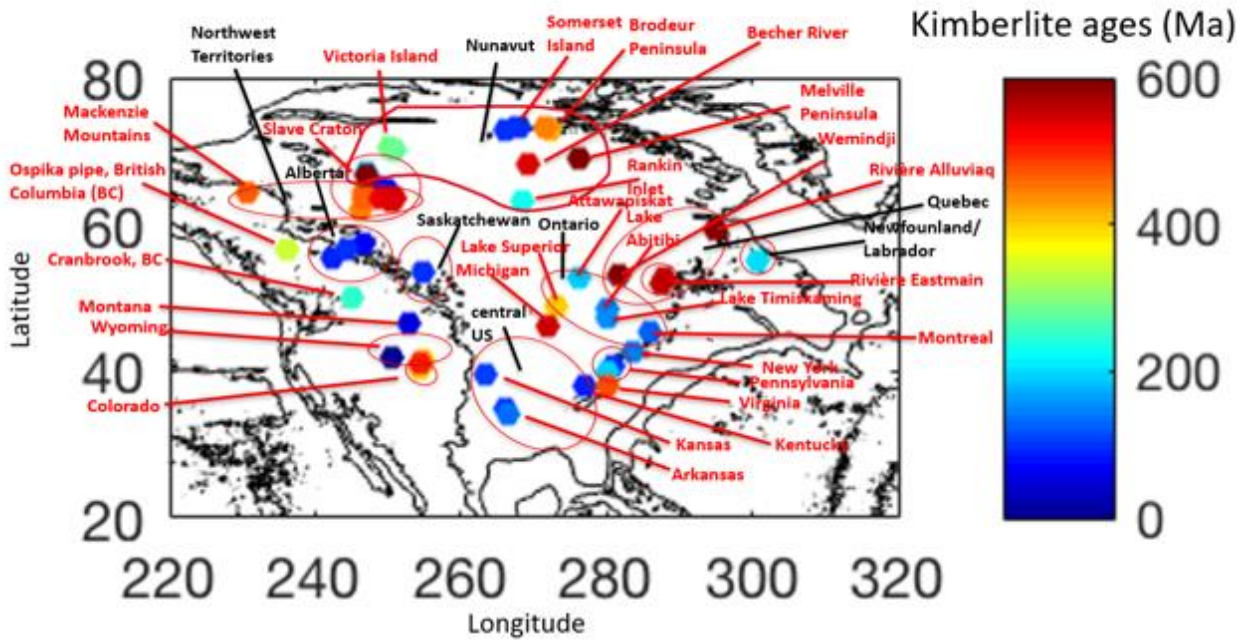

Figure 5.1. Locations and ages of the kimberlites considered in this study. The data are taken from Faure et al. (2010).

The names of the regions are reported in black, and the names of the states are reported in red. We also report in red smaller regions such as islands, peninsulas, small rivers, villages, and lakes. For each time period, the backtracked location indicates where the mantle source was (in relation to the current geography). The mantle source is fixed, and during kimberlite emplacement, the North American plate was lying above it.

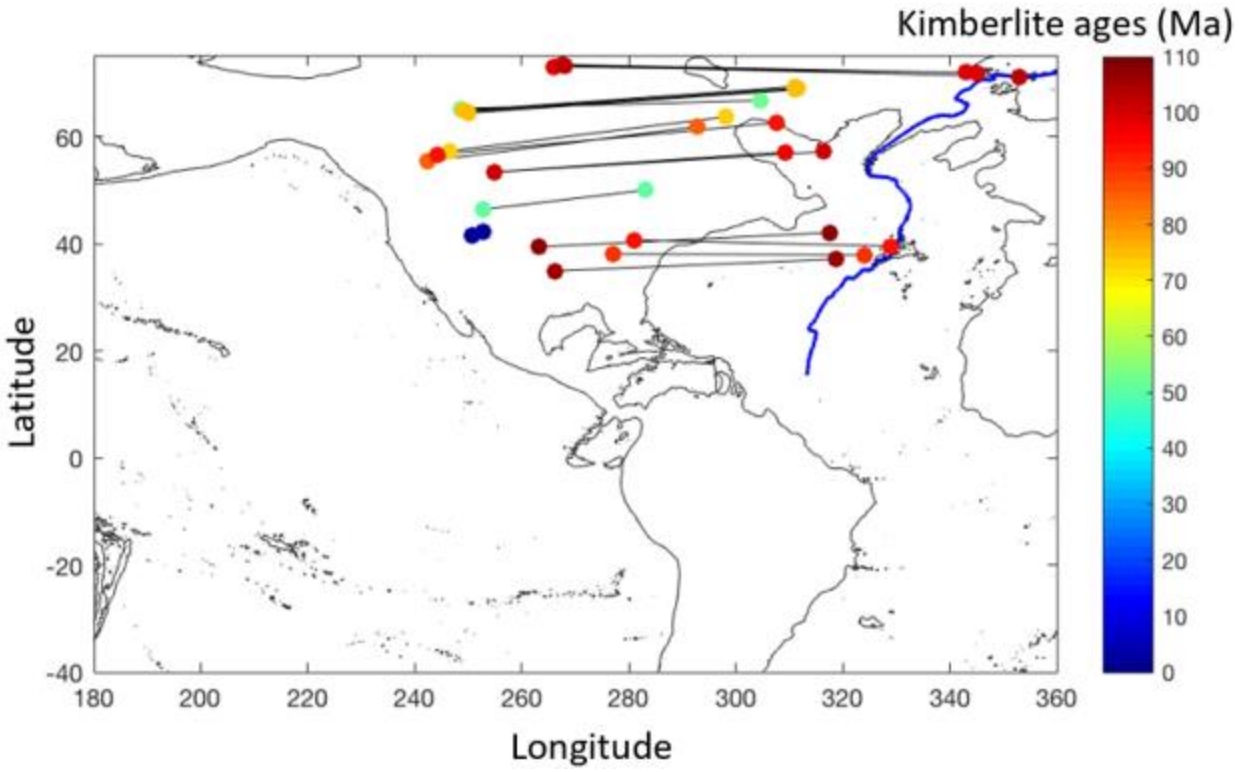

Figure 5.2. Present-day and backtracked kimberlite locations for the kimberlites emplaced on the North American continent during the period 0-110 Ma.

Kimberlite ages are from Faure et al. (2010). The backtracked locations have been computed with the rotation poles of Merdith et al. (2021) and GPlates software. The present-day and backtracked locations are connected by a black line. The northern part of the Mid-Atlantic ridge (data from Adam et al., 2015) is reported in blue.

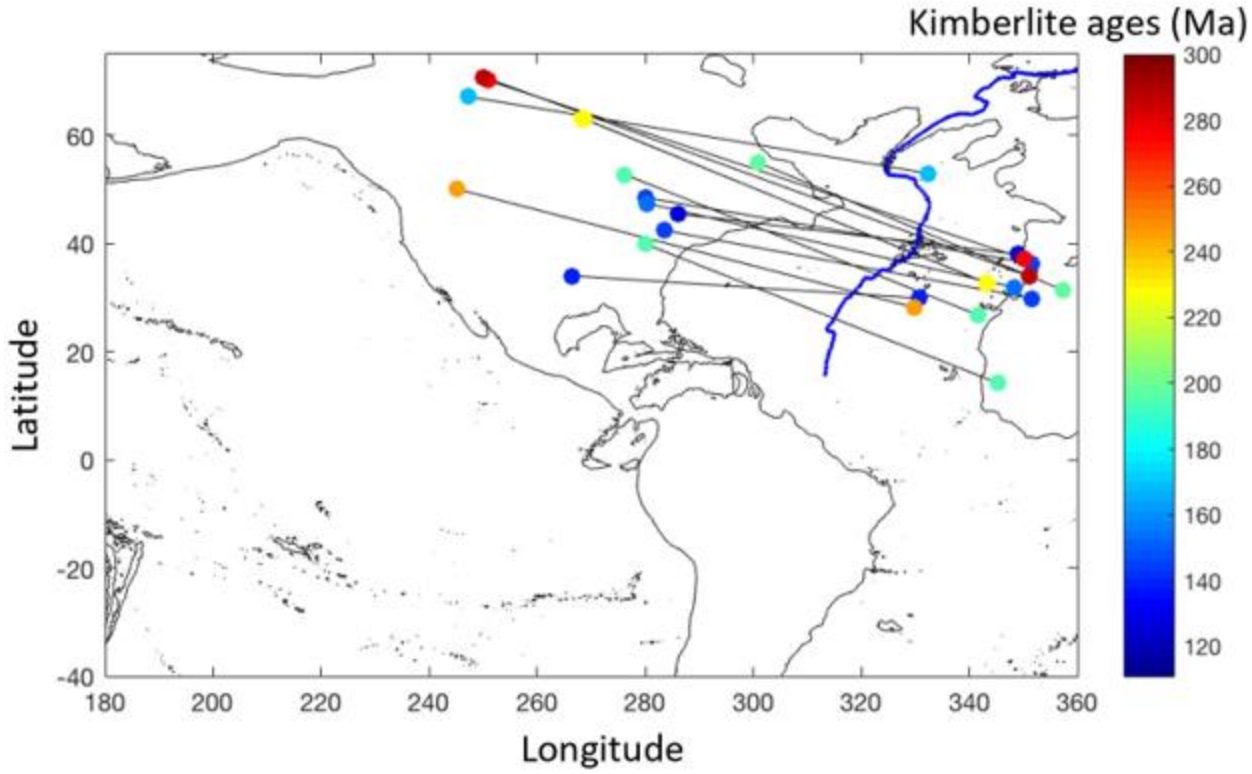

Figure 5.3. Present-day and backtracked kimberlite locations for the kimberlites emplaced on the North American continent during the period 110-300 Ma.

Kimberlites ages are from Faure et al. (2010). The backtracked locations have been computed with the rotation poles of Merdith et al. (2021) and GPlates software. The present-day and backtracked locations are connected by a black line. The northern part of the Mid-Atlantic ridge (data from Adam et al., 2015) is reported in blue.

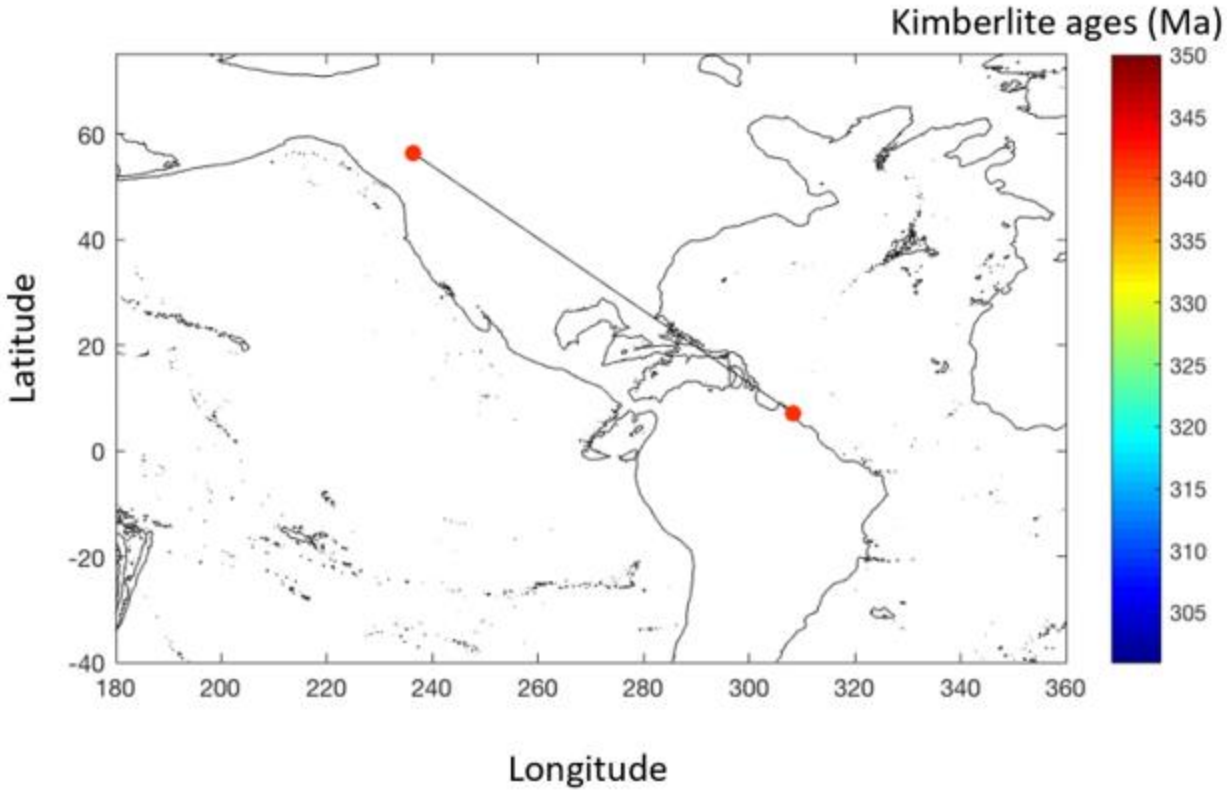

Figure 5.4. Present-day and backtracked kimberlite locations for the kimberlites emplaced on the North American continent during the period 300-350 Ma.

Kimberlite ages are from Faure et al. (2010). The backtracked location has been computed with the rotation poles of Merdith et al. (2021) and GPlates software. The present-day and backtracked locations are connected by a black line.

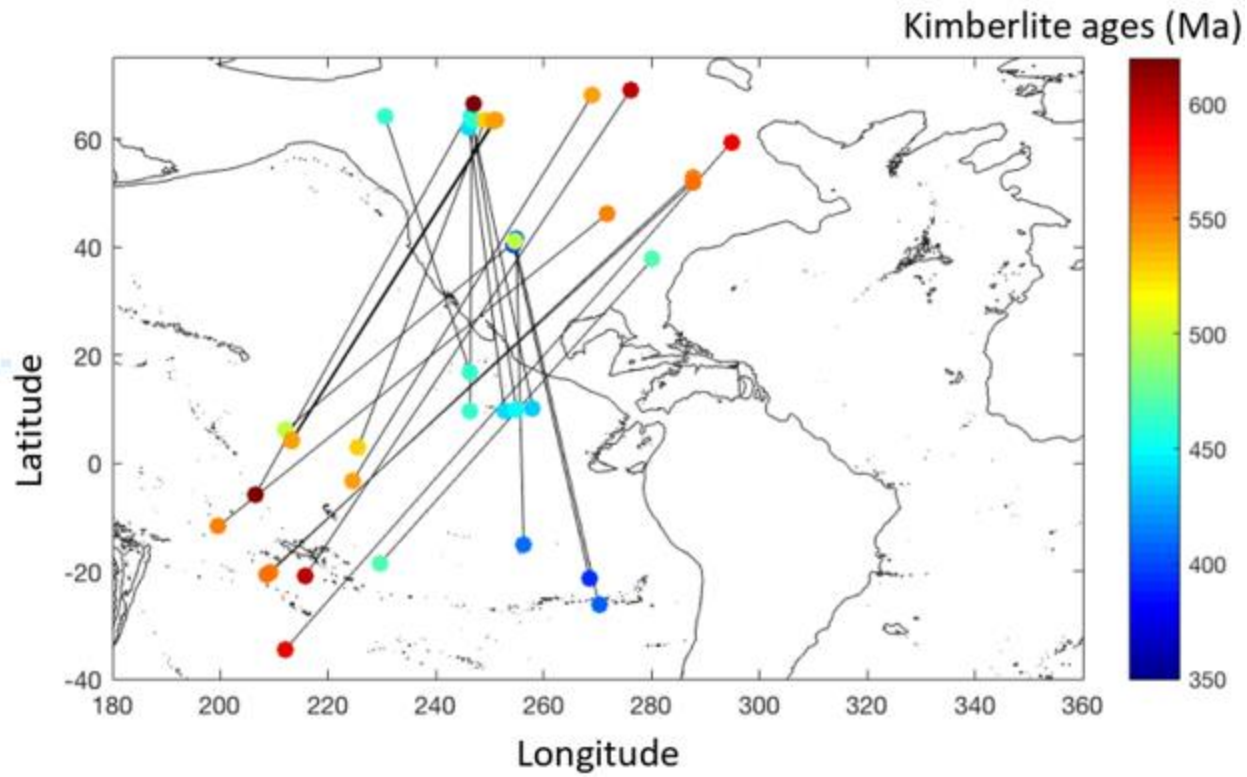

Figure 5.5. Present-day and backtracked kimberlite locations for the kimberlites emplaced over the North American continent during the period 350-620 Ma.

Kimberlites ages are from Faure et al. (2010). The backtracked locations have been computed with the rotation poles of Merdith et al. (2021) and GPlates software. The present-day and backtracked locations are connected by a black line.

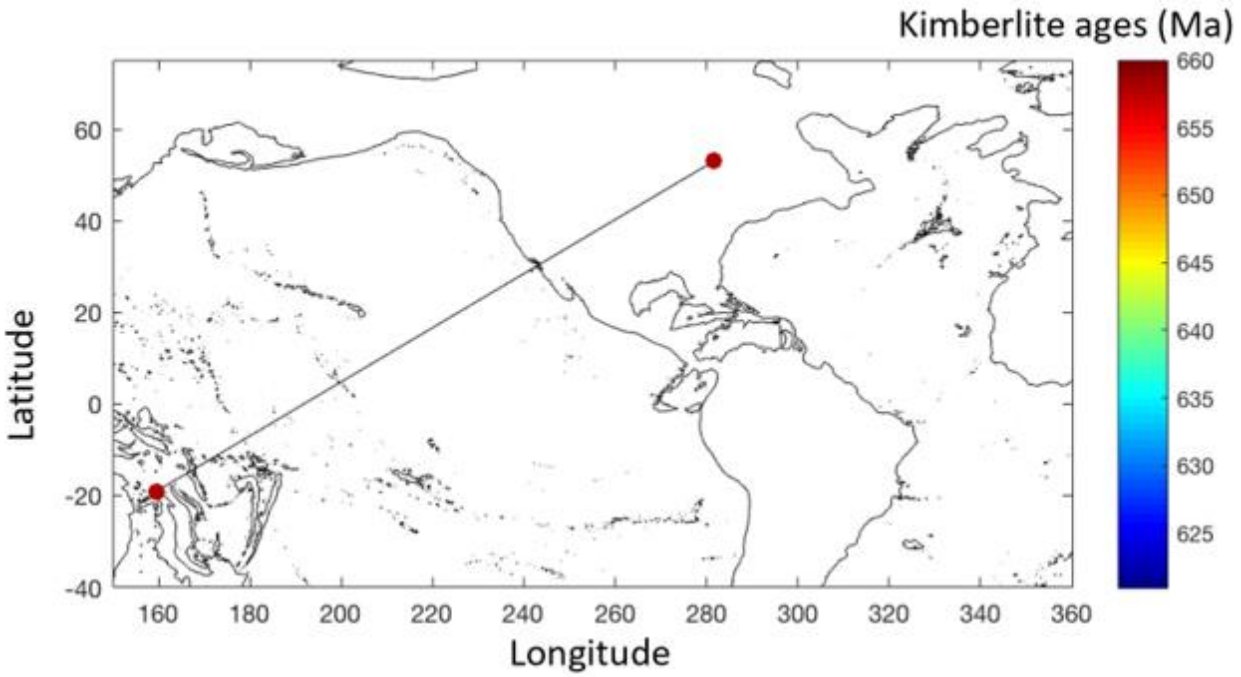

Figure 5.6. Present-day and backtracked kimberlite locations for the kimberlites emplaced over the North American continent during the period 620-660 Ma.

Kimberlites ages are from Faure et al. (2010). The backtracked location has been computed with the rotation poles of Merdith et al. (2021) and GPlates software. The present-day and backtracked locations are connected by a black line.

5.2. LLSVPs and spatio-temporal distribution of backtracked kimberlite locations

The Large Low Shear Velocity Provinces (LLSVPs) are two broad regions of the lowermost mantle beneath the Pacific and Atlantic Oceans, associated with slow seismic velocities (Davies et al., 2015; McNamara, 2019; Davaille and Romanowicz, 2020). The lateral and vertical extent of the LLSVPs is in the order of thousands and hundreds of kilometers, respectively (McNamara, 2019, and references therein). The position and extent of the LLSVPs are generally constrained from tomography models (Torsvik et al., 2014; McNamara, 2019; Giuliani et al., 2020). Tomography models may differ from one another, as they are derived

from different datasets, using different inversion methods. In this study we consider two widely used tomography models: the SEMUCB-WM1 model, developed by French and Romanowicz (2014) (Figures 5.7 to 5.11), and the SAVANI model, developed by Auer et al. (2014) (Figures 5.12 to 5.16). In Figures 5.7 to 5.16, we display the lateral seismic velocity anomaly, *dvs*, provided by the tomography models near the core-mantle boundary (depth~ 2800 km) as well as the backtracked kimberlite locations from this study. The aim is to investigate whether there is any relationship between the LLSVPs and the backtracked kimberlite locations. As discussed in section 5.1, we have identified five distinct time periods for which the backtracked kimberlite locations display different patterns: 0-110 Ma, 110-300 Ma, 300-350 Ma, 350-620 Ma, and 620-660 Ma (Figures 5.7 to 5.16).

The backtracked positions of the youngest kimberlites (ages < 110 Ma) do not correlate with LLSVPs (Figures 5.7 and 5.12), but the backtracked kimberlite locations for ages 110-300 Ma are located over the Atlantic LLSVP, between latitudes 10 and 60^{o}N (Figures 5.8 and 5.13). Similarly, the backtracked positions of the kimberlites with ages between 350 and 620 Ma all correlate with the location of the Pacific LLSVP today (Figures 5.10 and 5.15). The oldest kimberlite is 658 Ma, and its backtracked position also correlates with the Pacific LLSVP, although its backtracked position is 40^{o} west (~ 4000 km west) of the younger kimberlites (Figures 5.11 and 5.16). Although the two tomography models display some differences, the apparent association of the backtracked kimberlite locations, for kimberlites older than 110 Ma, with the position of LLSVPs today is striking.

Some previous studies have already proposed that kimberlite emplacement is connected to the positions of LLSVPs (e.g., Torsvik et al., 2014; Giuliani et al., 2020). LLSVPs are large-scale heterogeneities at the bottom of the lower mantle, and they are separated from each other

by fast velocity regions (Davaille and Romanowicz, 2020). They are often thought to be large, thermochemical piles accumulated at the base of the mantle (Davies et al., 2015; Mulyukova et al., 2015; Kreielkamp et al., 2022). LLSVPs are also thought to be stable and long-standing structures (Mulyukova et al., 2015). According to several authors, various scales of mantle plumes may be derived from the LLSVPs (Kellogg et al., 1999; Davaille, 1999; Courtillot et al., 2003; Dziewonski et al., 2010; Torsvik et al., 2014) (Figure 5.17). This model has been proposed, because numerous hotspot chains appear to be located above the LLSVPs (Davies et al., 2015; Torsvik et al., 2016). The LLSVPs are found mainly at the core-mantle boundary that corresponds to locations of oceanic crust in the Atlantic and Pacific Oceans, and these LLSVPs are referred to as the Atlantic LLSVP and Pacific LLSVP, respectively (Davies et al., 2015; Davaille and Romanowicz, 2020). The Atlantic LLSVP is often referred to as the "African LLSVP," as the largest *dvs* values are found beneath the African continent. However, low *dvs* values extend into the region beneath the northern Atlantic as well (Torsvik et al., 2014; Giuliani et al., 2020).

LLSVPs are also thought of as zones of where subducted oceanic crust have accumulated since the early periods of subduction. Subducted oceanic crust are much more depleted in incompatible elements than ocean island basalts, and this is because the oceanic crust inherits its signatures of incompatible elements from the upper mantle (Hofmann, 1988; Niu and O'Hara, 2003). Niu (2018) says LLSVPs have been stable in structure for the last 300 m.y. because 95% of oceanic crust subducted in the deep mantle, subducted before 300 Ma. In addition, the LLSVPs have been stable because they are antipodal and the center of the mass of the LLSVPs aligns with the spin axis of the Earth (Niu, 2018).

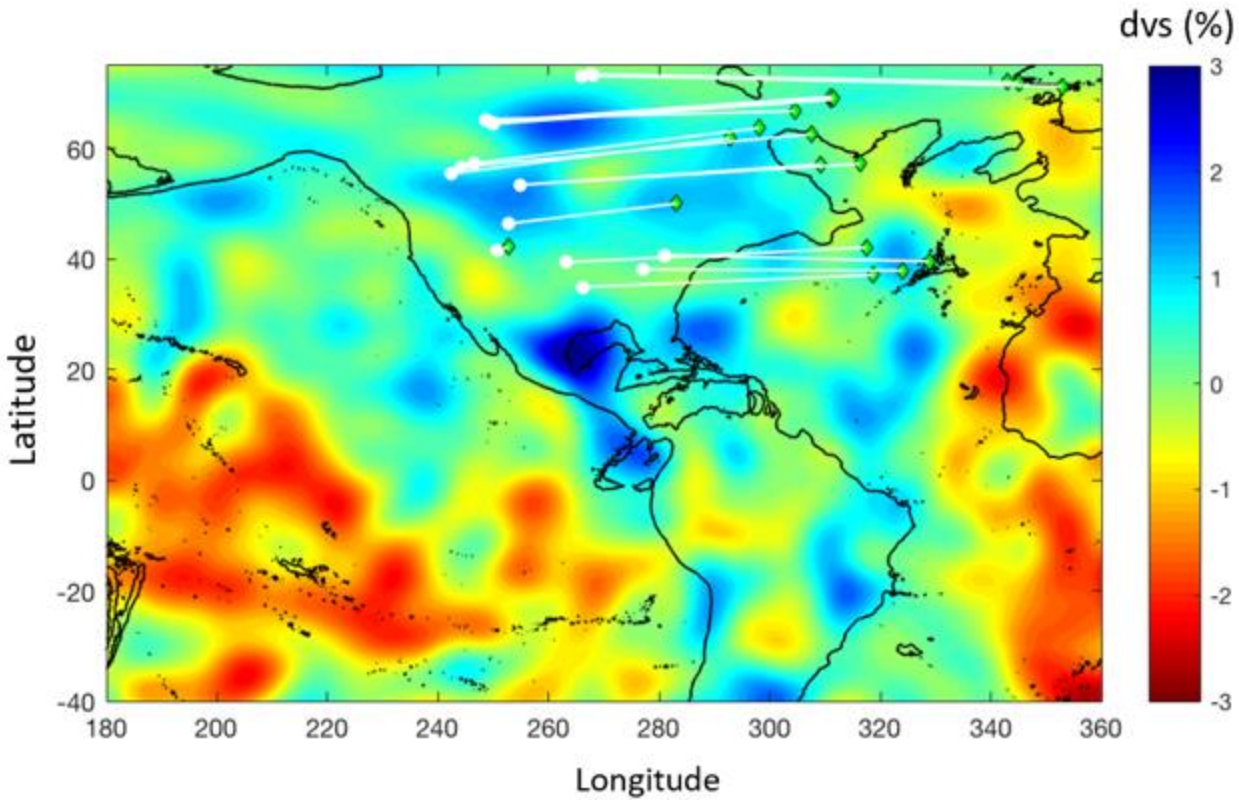

Figure 5.7. Seismic tomography SEMUCB-WM1 (French and Romanowicz, 2014) with the present-day and the backtracked kimberlites positions for the 0-110 Ma period.

The location and age data of the kimberlites are from Faure et al. (2010); the rotation poles used for the backtracking are from Merdith et al. (2021). The white filled circles show the present-day locations of kimberlites and the green diamonds their backtracked position. The present-day and backtracked locations are connected by a white line. The color map represents the seismic velocity anomaly, *dvs*, at ~2800 km depth.

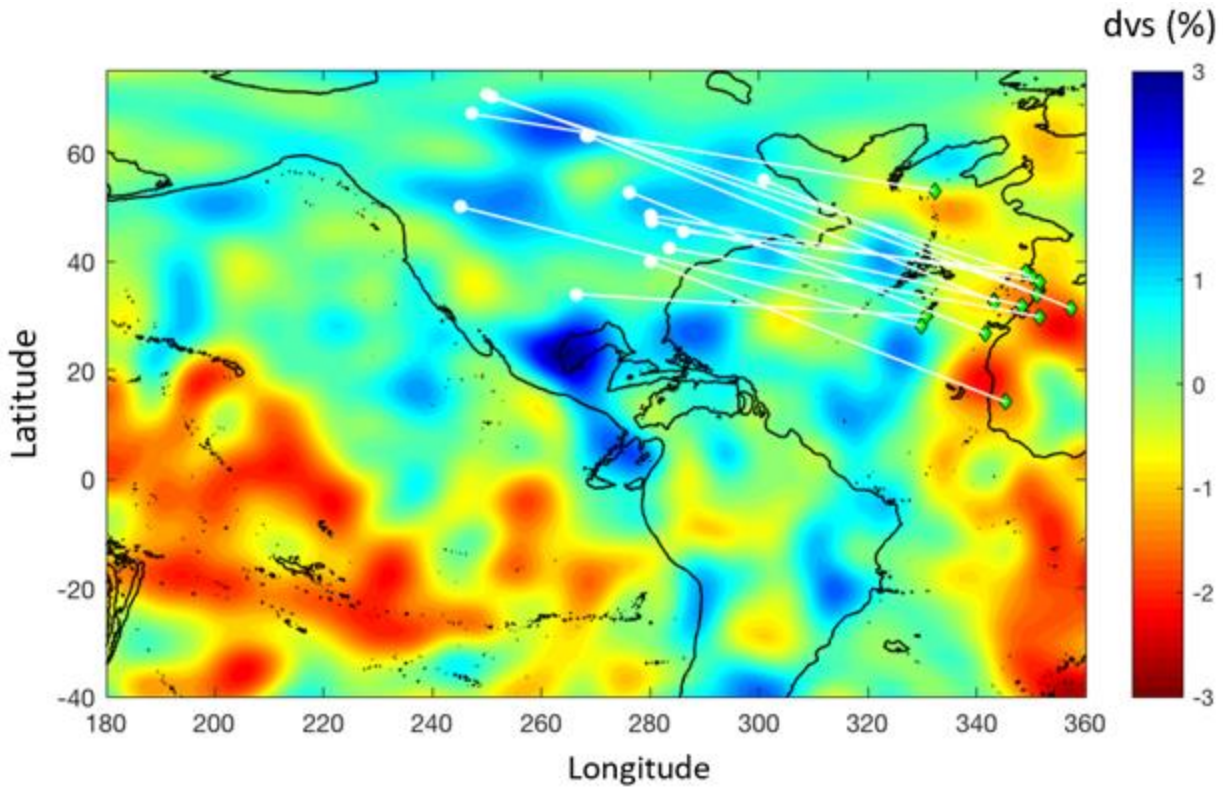

Figure 5.8. Seismic tomography SEMUCB-WM1 (French and Romanowicz, 2014) with present-day kimberlite positions and backtracked kimberlite positions for ages 110-300 Ma.

The location and age data of the kimberlites are from Faure et al. (2010); the rotation poles used for the backtracking are from Merdith et al. (2021). The white filled circles show the present-day locations of kimberlites and the green diamonds their backtracked position. The present-day and backtracked locations are connected by a white line. The color map represents the seismic velocity anomaly, *dvs*, at ~2800 km depth.

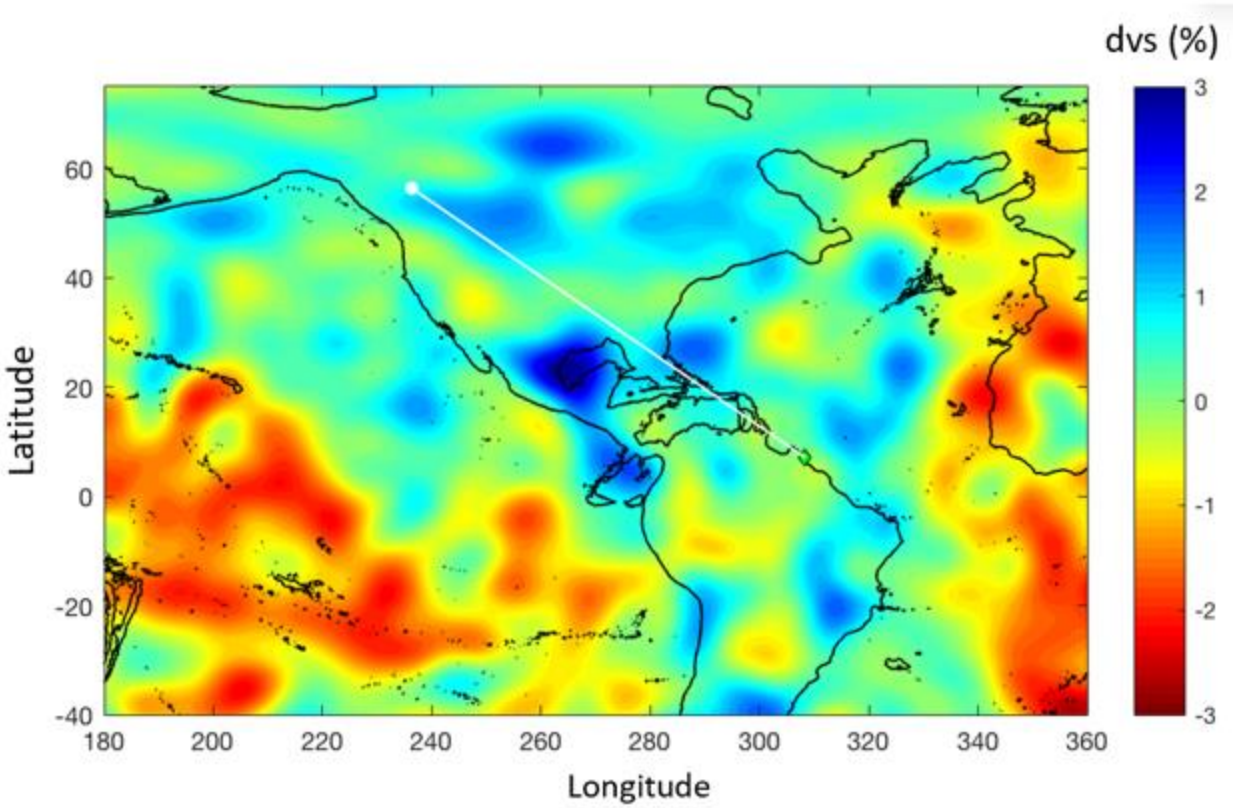

Figure 5.9. Seismic tomography SEMUCB-WM1 (French and Romanowicz, 2014) with present-day kimberlite position and backtracked kimberlite position for age 300-350 Ma.

The location and age data of the kimberlites are from Faure et al. (2010); the rotation poles used for the backtracking are from Merdith et al. (2021). The white filled circle shows the present-day locations of kimberlite and the green diamond its backtracked position. The present-day and backtracked locations are connected by a white line. The color map represents the seismic velocity anomaly, *dvs*, at ~2800 km depth.

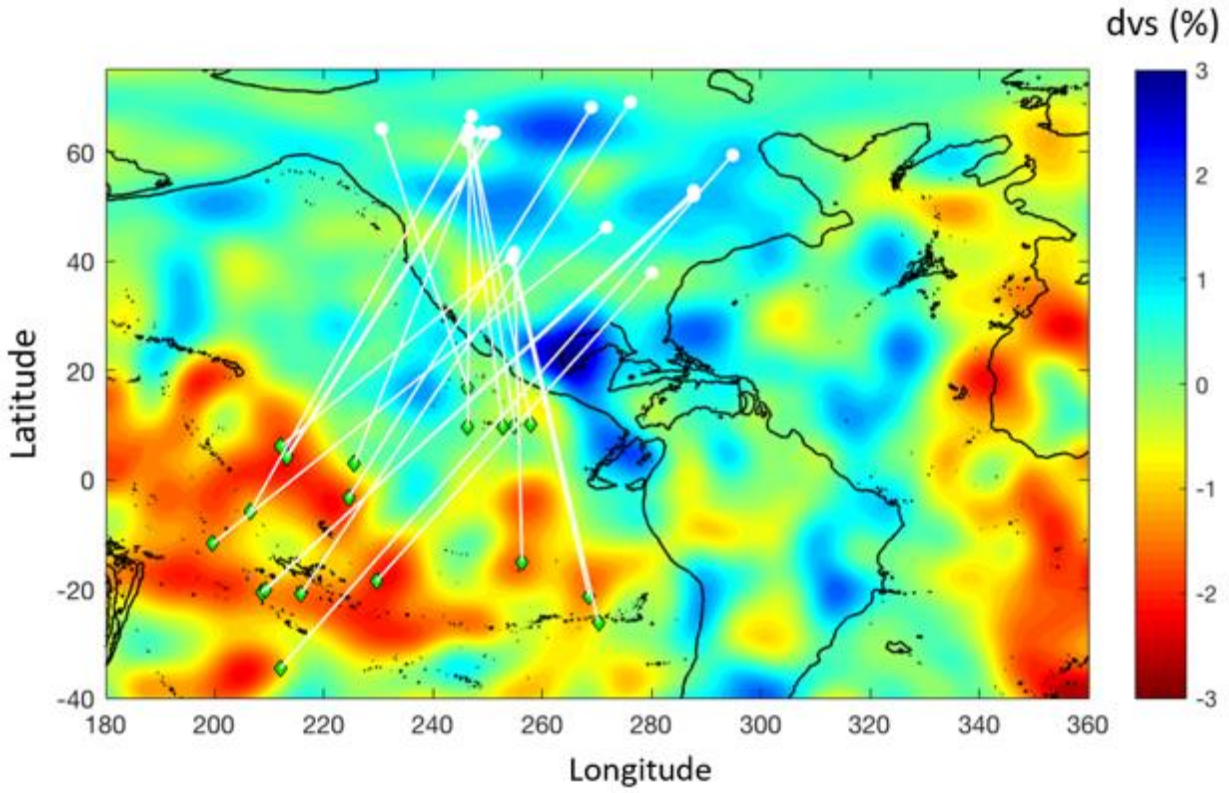

Figure 5.10. Seismic tomography SEMUCB-WM1 (French and Romanowicz, 2014) with present-day kimberlite positions and backtracked kimberlite positions for age 350-620 Ma.

The location and age data of the kimberlites are from Faure et al. (2010) the rotation poles used for the backtracking are from Merdith et al. (2021). The white filled circle shows the present-day locations of kimberlite and the green diamond its backtracked position. The present-day and backtracked locations are connected by a white line. The color map represents the seismic velocity anomaly, *dvs*, at ~2800 km depth.

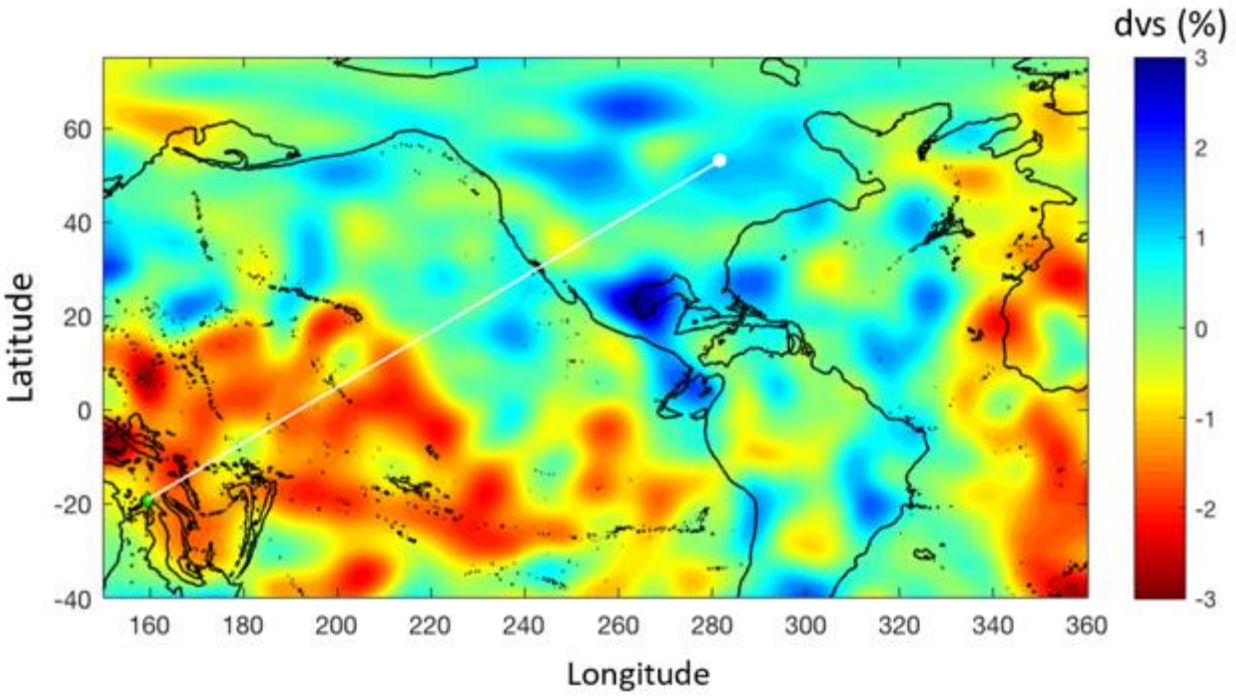

Figure 5.11. Seismic tomography SEMUCB-WM1 (French and Romanowicz, 2014) with present-day kimberlite position and backtracked kimberlite position for age 620-660 Ma.

The location and age data of the kimberlites are from Faure et al. (2010) the rotation poles used for the backtracking are from Merdith et al. (2021). The white filled circle shows the present-day locations of kimberlite and the green diamond its backtracked position. The present-day and backtracked locations are connected by a white line. The color map represents the seismic velocity anomaly, *dvs*, at ~2800 km depth.

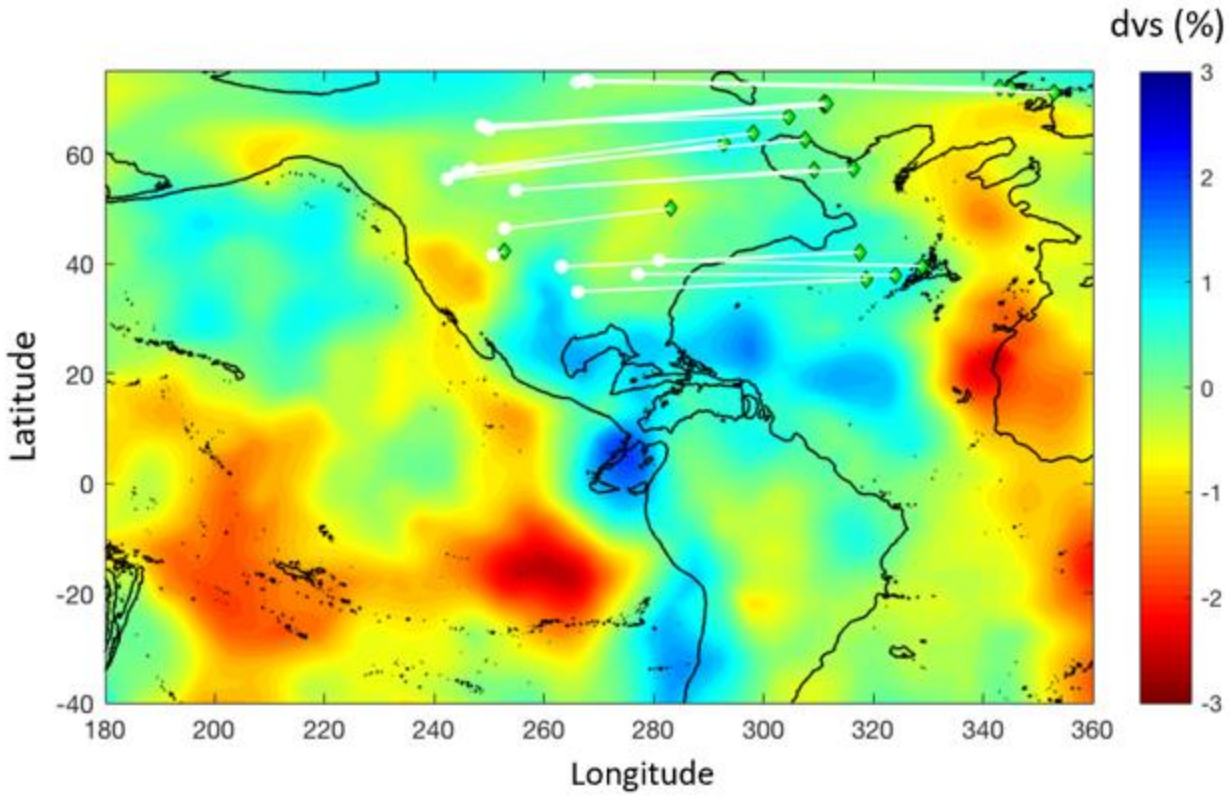

Figure 5.12. Seismic tomography SAVANI (Auer et al., 2014) with present-day kimberlite positions and backtracked kimberlite positions for age 0-110 Ma.

The location and age data of the kimberlites are from Faure et al. (2010); the rotation poles used for the backtracking are from Merdith et al. (2021). The white filled circle shows the present-day locations of kimberlite and the green diamond its backtracked position. The present-day and backtracked locations are connected by a white line. The color map represents the seismic velocity anomaly, *dvs*, at ~2800 km depth.

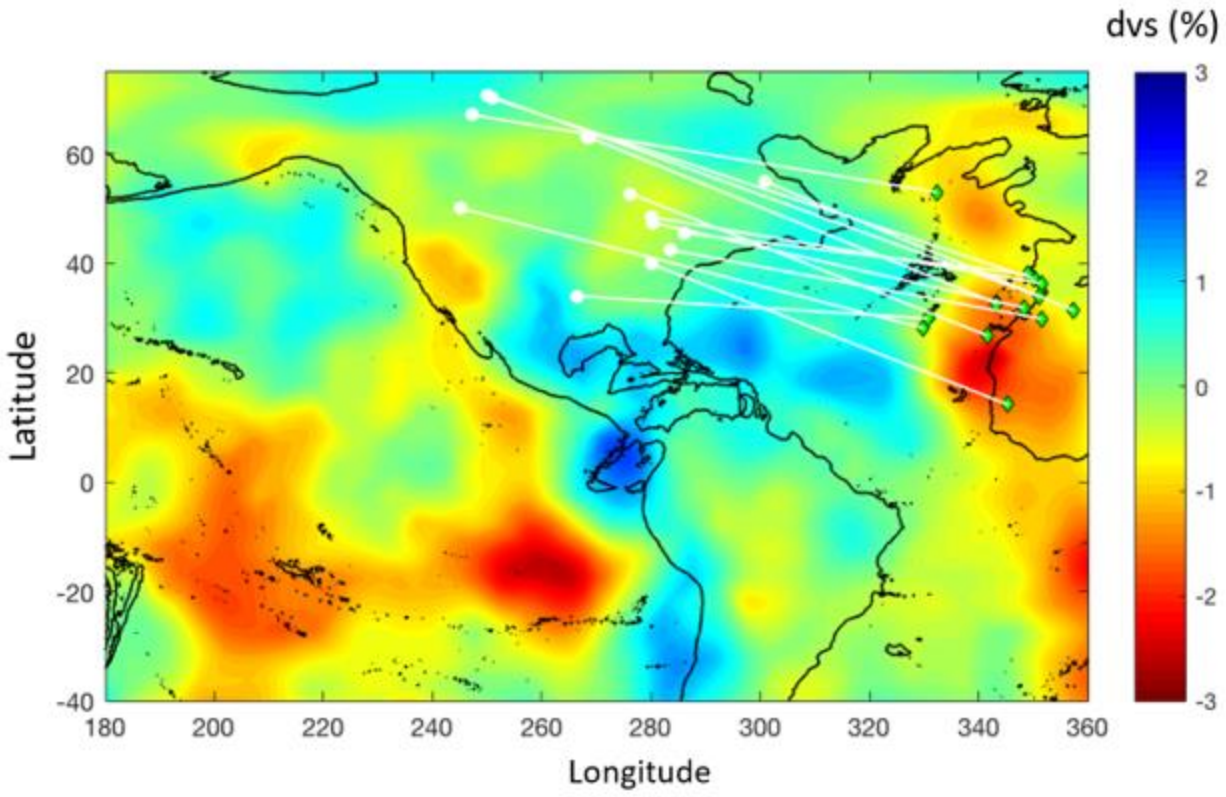

Figure 5.13. Seismic tomography SAVANI (Auer et al., 2014) with present-day kimberlite positions and backtracked kimberlite positions for age 110-300 Ma.

The location and age data of the kimberlites are from Faure et al. (2010); the rotation poles used for the backtracking are from Merdith et al. (2021). The white filled circle shows the present-day locations of kimberlite and the green diamond its backtracked position. The present-day and backtracked locations are connected by a white line. The color map represents the seismic velocity anomaly, *dvs*, at ~2800 km depth.

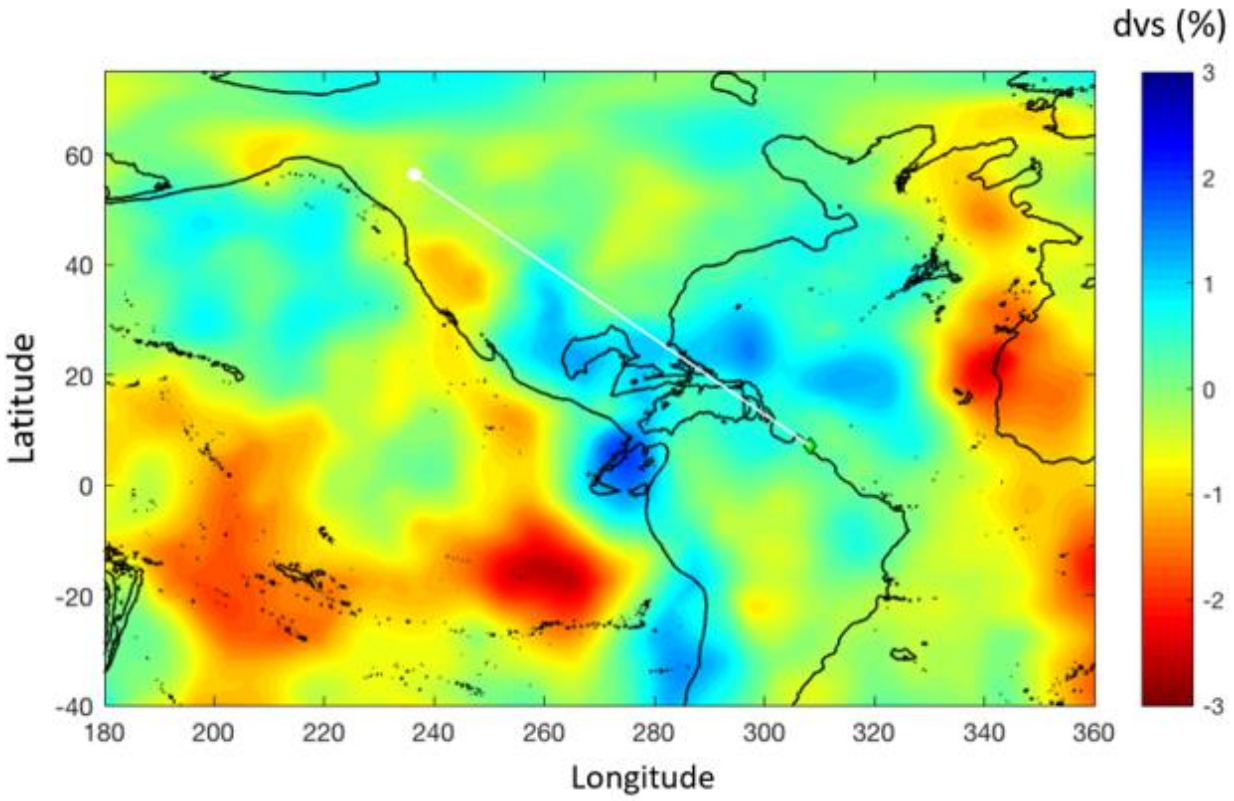

Figure 5.14. Seismic tomography SAVANI (Auer et al., 2014) with present-day kimberlite position and backtracked kimberlite position for age 300-350 Ma.

The location and age data of the kimberlites are from Faure et al. (2010): the rotation poles used for the backtracking are from Merdith et al. (2021). The white filled circle shows the present-day locations of kimberlite and the green diamond its backtracked position. The present-day and backtracked locations are connected by a white line. The color map represents the seismic velocity anomaly, *dvs*, at ~2800 km depth.

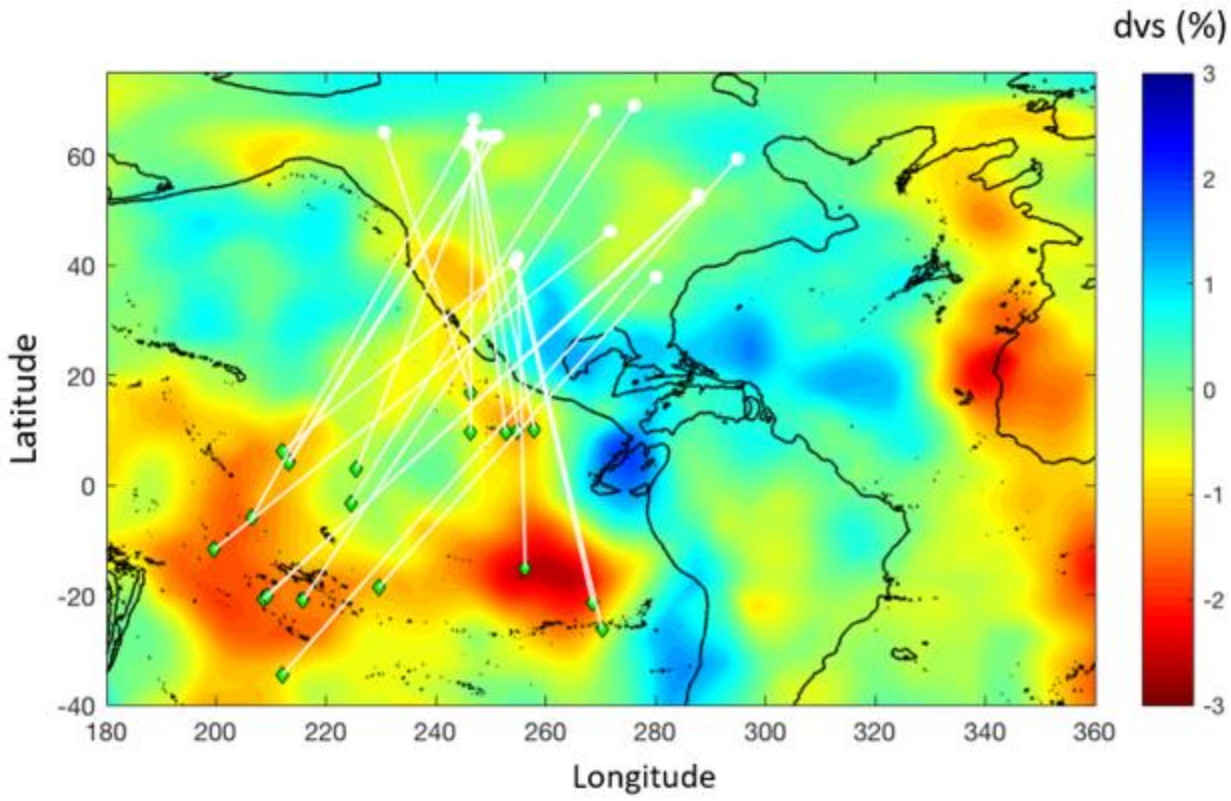

Figure 5.15. Seismic tomography SAVANI (Auer et al., 2014) with present-day kimberlite positions and backtracked kimberlite positions for age 350-620 Ma.

The location and age data of the kimberlites are from Faure et al. (2010); the rotation poles used for the backtracking are from Merdith et al. (2021). The white filled circle shows the present-day locations of kimberlite and the green diamond its backtracked position. The present-day and backtracked locations are connected by a white line. The color map represents the seismic velocity anomaly, *dvs*, at ~2800 km depth.

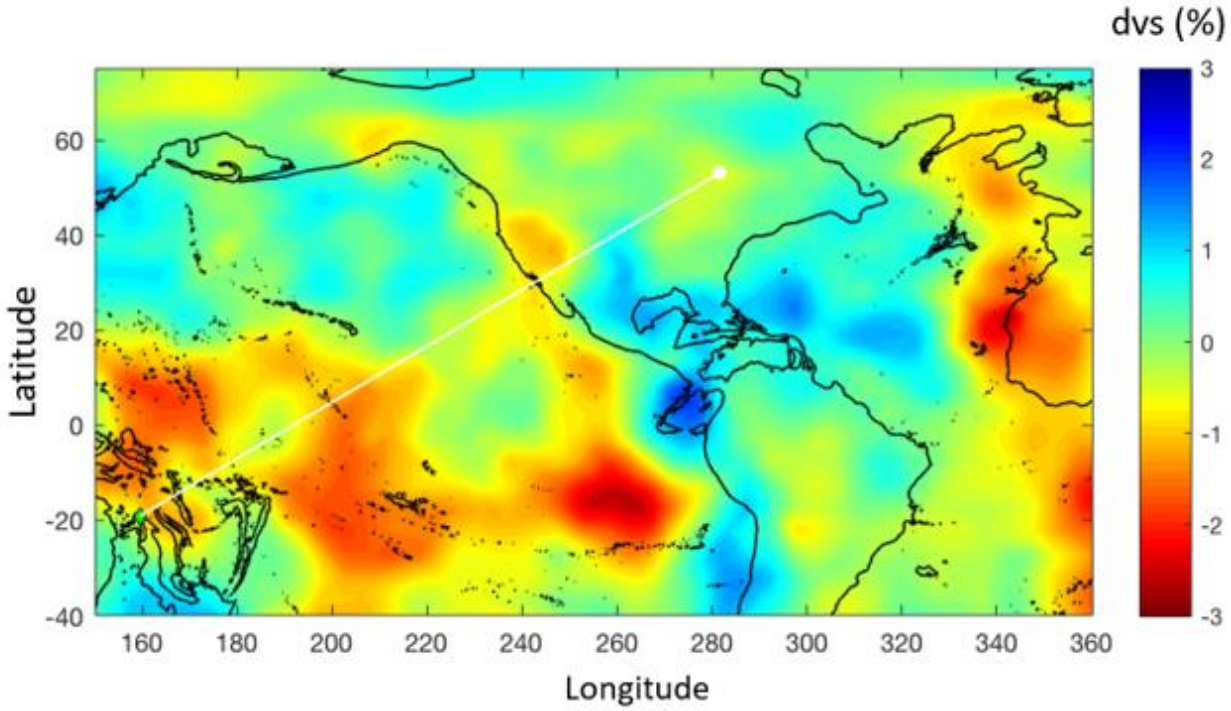

Figure 5.16. Seismic tomography SAVANI (Auer et al., 2014) with present-day kimberlite position and backtracked kimberlite position for age 620-660 Ma.

The location and age data of the kimberlites are from Faure et al. (2010); the rotation poles used for the backtracking are from Merdith et al. (2021). The white filled circle shows the present-day locations of kimberlite and the green diamond its backtracked position. The present-day and backtracked locations are connected by a white line. The color map represents the seismic velocity anomaly, *dvs*, at ~2800 km depth.

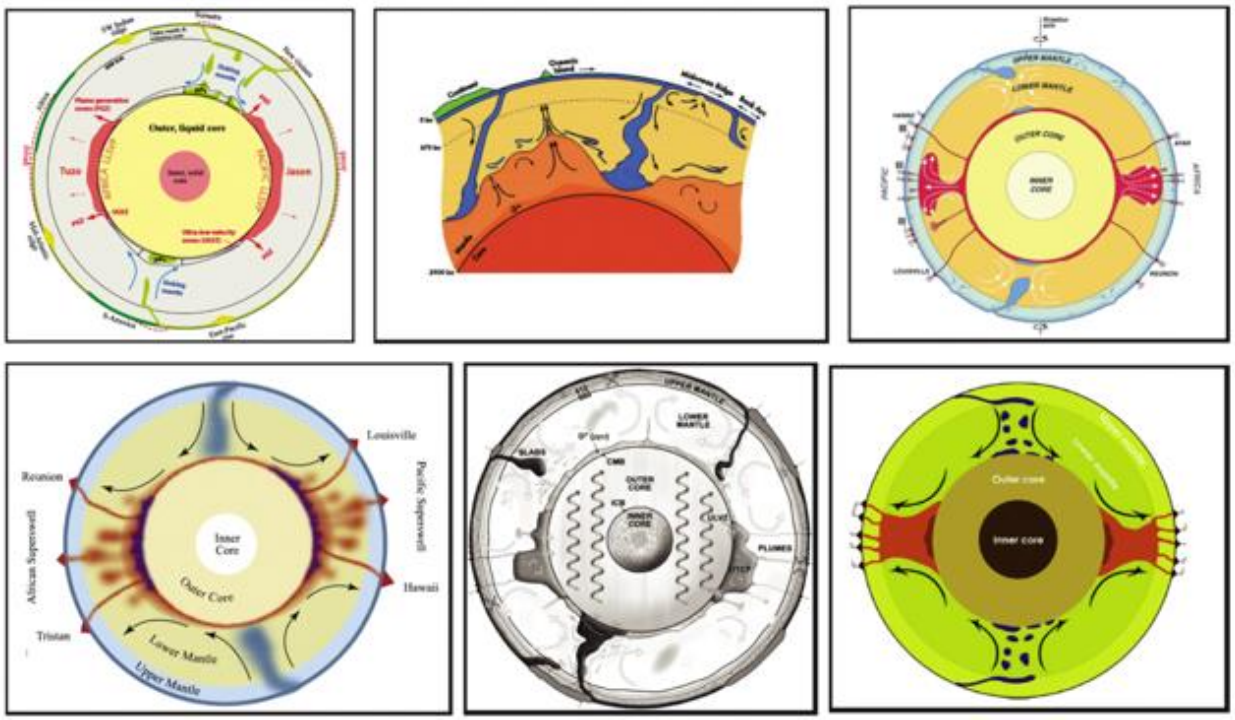

Figure 5.17. Conceptual models of LLSVPs (from McNamara, 2019).

Figures are modified from the following sources: top-left - Torsvik et al. (2014). This model shows the geoids of the Atlantic LLSVP and the Pacific LLSVP and the buoyant upwelling of the mantle in the LLSVP regions; top-middle - Kellogg et al. (1999). This model shows the dynamics of the lower mantle due to the deflection of the downwelling subducting slabs (the thermal circulation is driven by internal heat from the core-mantle boundary); top-right - Courtillot et al. (2003). This model shows the dynamics of the Earth's mantle by showing the sources of the three different type of hotspots and indicating the rotation of the Earth on its axis; bottom-left – Jellinek and Manga (2004). This model shows the thermodynamic interaction of the tectonic plates and the cooling core; bottom-middle – Garnero et al. (2005). This model shows the large convections in the mantle with subducted cool lithosphere and large thermochemical piles at the low shear velocity regions at the core-mantle-boundary; bottom-right – Dziewonski et al. (2010). This model shows the circulation within the Earth's mantle and of subducted slabs.

LLSVPs have been hypothesized as a potential source for generation of kimberlites (Tappe et al., 2014; Torsvik et al., 2014; Giuliani et al., 2020). This is because many kimberlites

are reconstructed to the margins of the LLSVPs (Torsvik et al., 2016). Not only that, large igneous provinces can also be accounted for eruptions using the same reason (Torsvik et al., 2016). According to some models, since 1 Ga, subduction led to recycling of lithospheric and crustal material into long-term storage in the lower mantle (e.g., Tappe et al., 2014; Stern et al., 2016; Torsvik et al., 2016). Giuliani et al. (2020) show that kimberlites are isotopically similar to some ocean island basalts (OIB) in that they both have Sr-Nd-Hf isotopic compositions within the range of PREMA. Nd-Hf isotope systematics have shown that kimberlites could be related to primitive mantle (Giuliani et al., 2020; Pearson et al., 2019; Woodhead et al., 2019), while Nd-Sr trends can show that kimberlites are at least sub-lithospheric mantle in origin (Pearson et al., 2019), although these authors do not specify whether that is from just below the lithosphere, within the transition zone, or as deep as the core–mantle boundary. When the Nd-Hf ratios of kimberlites are compared to those of mid-ocean ridge basalts and ocean island basalts, some kimberlites could be associated with the deep asthenosphere and even the transition zone (Pearson et al., 2019). The kimberlites tend to be associated with different depths in the mantle depending on their isotopic signatures (Pearson et al., 2019). Furthermore, partial melting of the mantle materials that are sub-lithospheric in origin can cause kimberlite melts beneath a thick continental lithosphere to form where volatiles can become enriched (Tappe et al., 2014; Pearson et al., 2019).

The hypothesis that kimberlites may originate from LLSVPs is in agreement with our results for kimberlites older than 110 Ma. Indeed, we find that the backtracked kimberlite locations correlate with LLSVPs for ages 110-660 Ma. Moreover, our results indicate a temporal evolution for kimberlite emplacement: kimberlites emplaced between 110-300 Ma were emplaced over the Atlantic LLSVP, whereas older kimberlites (ages 350-660 Ma) were

emplaced over the Pacific LLSVP. Although this spatial association is insufficient on its own to prove that kimberlites originate within LLSVPs, it is certainly consistent with this hypothesis. However, the youngest kimberlites, i.e. those with ages less than ~110 Ma, do not seem to correlate spatially with LLSVPs. This means that, even if the LLSVPs contribute in some way to the generation of kimberlites, this cannot be the only mechanism. In the next section, we investigate whether their emplacement may be accounted for by edge-driven convection.

5.3. LAB gradient and spatio-temporal distribution of backtracked kimberlite locations

Edge-driven convection (EDC) is a convection pattern induced by variation in lithosphere thickness (King and Anderson, 1998) (Figure 2.4). This setup creates a convection cell where upwellings occur along the transition between the thicker and thinner lithosphere. Edge-driven convection has been invoked to explain the origin of the volcanic emplacements of the Bermuda Rise (King and Anderson, 1998), Canary Island volcanism (Manjón-Cabeza Córdoba and Ballmer, 2021), and could even explain the emplacement of kimberlites in Kansas (Kempton et al., 2019). In this section, we investigate the potential correlation between the location of young kimberlites (age < 110 Ma) and the gradient of the lithosphere-asthenosphere boundary (LAB gradients). We consider two LAB models in this study: the CAM2016 model, developed by Priestley et al. (2018) (Figure 5.18) and the LITHO1.0 model, developed by Pasyanos et al. (2014) (Figure 5.19). In Figures 5.18 and 5.19, we show the gradient of these LAB models, as well as the ages and present-day locations of the kimberlites.

In Figure 5.18 we can see that most kimberlites are located over regions with a high LAB gradient (white regions). There are, however, a few exceptions, e.g. the kimberlites located in the Slave Craton. The CAM2016 model (Priestley et al., 2019) uses the inversion of surface-

wave waveforms and shows mainly long wavelength features (Love waves that are in the period range of 50-250 s) (Figure 4.5). The relationship between the seismic velocities in the LAB region and the temperatures of the upper mantle and the asthenosphere is the basis of the CAM2016 model, and this technique is used because the boundary between the shallow mantle and the lower mantle is not clear by compositional properties and temperature differences (Priestley et al., 2018). We, therefore, consider another model, the LITHO1.0 model (Pasyanos et al., 2014), which uses high-resolution surface wave dispersion maps and yields a lateral resolution of 1^{o} (~100 km), i.e., much shorter wavelengths (Figure 4.6). The gradient of the LAB according to the LITHO1.0 model is displayed in Figure 5.19. The figure shows that all the kimberlites with ages less than 110 Ma are located above regions with a high LAB gradient (white regions).

Location of these kimberlites above regions with steep LAB gradients is consistent with emplacement facilitated by EDC. EDC causes partial melting or decompression melting along the upwelling flow created by the LAB gradients (Figure 2.4) (King and Anderson, 1998; Kjarsgaard et al., 2017).

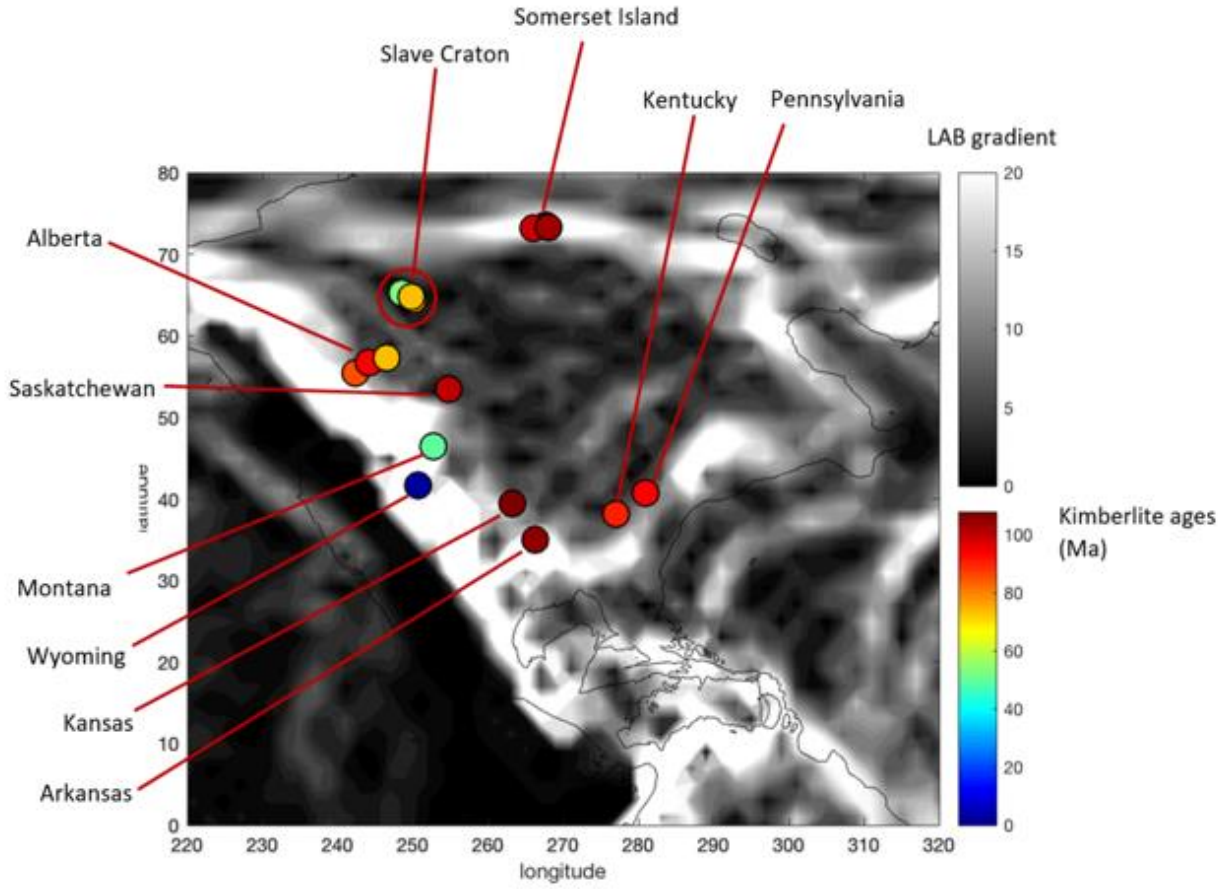

Figure 5.18. Gradient of LAB according to the CAM2016 model (Priestley et al., 2018) and present-day locations of kimberlites ages 0-110 Ma in North America.

The black and white map represents the LAB gradient while considering the LAB provided by the CAM2016 model (Priestley et al., 2018). The red open circle shows the location of kimberlites that are not on a high gradient. The colored circles show the positions and ages of the North American kimberlites for 0-110 Ma (data from Faure et al., 2010).

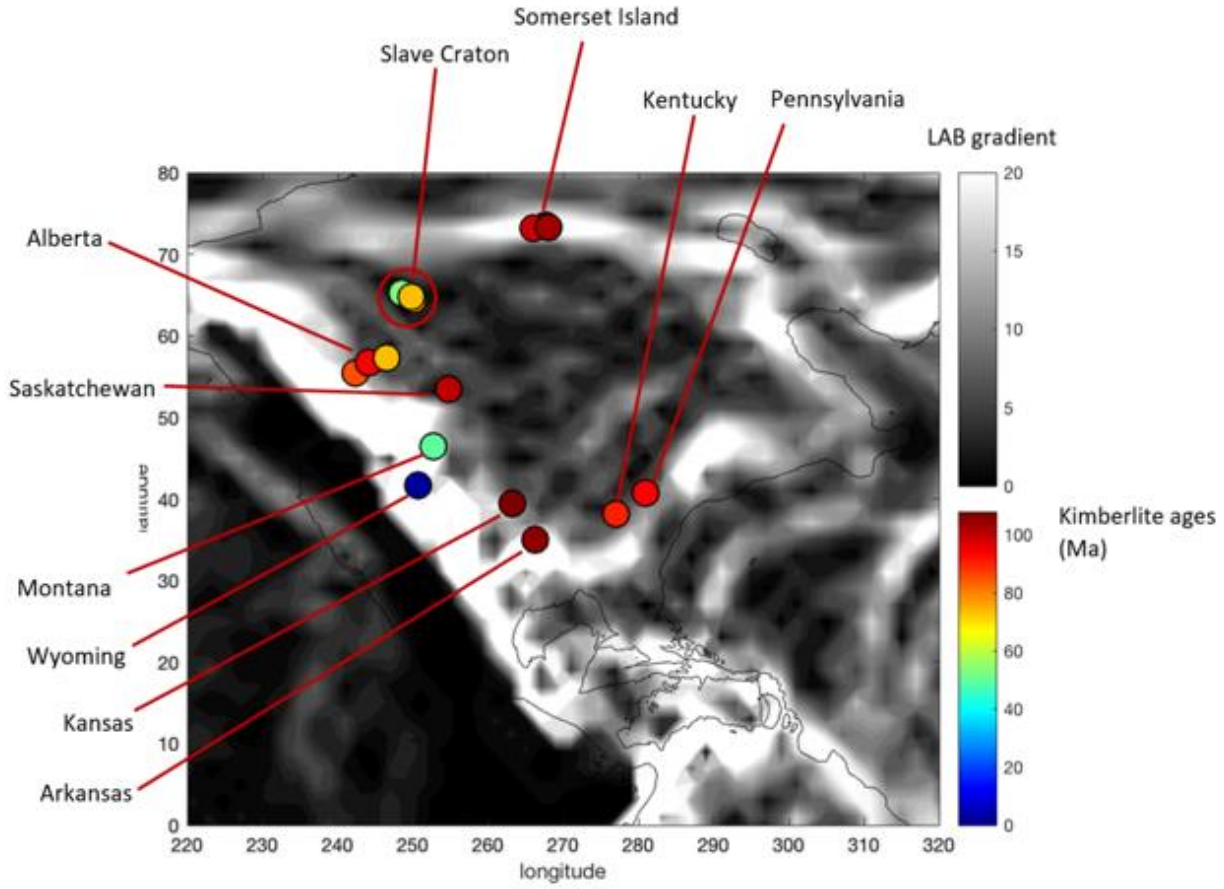

Figure 5.19. Gradient of LAB according to the LITHO1.0 model (Pasyanos et al., 2014) and the present-day locations of kimberlites ages 0-110 Ma in North America.

The black and white map represents the LAB gradient while considering the LAB provided by the LITHO1.0 model (Pasyanos et al., 2014). The red open circle shows the locations of kimberlites that are not on a high gradient. The colored circles show the positions and ages of the North American kimberlites for 0-110 Ma (data from Faure et al., 2010).

5.4. Plume hypothesis

Several studies state that the entrainment of kimberlites by a plume provides a plausible mechanism for generating kimberlites (Heaman and Kjarsgaard, 2000; Chu et al., 2013). Heaman and Kjarsgaard (2000) propose that the emplacement of kimberlites at Rankin, Attawapiskat, and Kirkland Lake is related to the passage of the Great Meteor plume beneath the region (Figure 5.20). Their interpretation is based on the observation that these localities are

aligned and also in alignment with the New England seamounts in the Atlantic, which are attributed to the Great Meteor hotspot. However, these authors did not perform kinematic modeling, such as that provided in this study. In order to see whether the Heaman and Kjarsgaard (2000) plume hypothesis is in agreement with the rotation poles describing the motion of the North American plate, we computed the track of the hotspot that would be at the origin of the Rankin kimberlites (Figure 5.20). The computation is similar to that described in section 2.1.1, and we use the rotation poles of Merdith et al. (2021).

Our trajectory, reconstructed for 200 Ma, is reported in blue in Figure 5.20b and c. The figure shows that the calculated track does not pass through the locations of the Attawapiskat and Kirkland Lake kimberlites (Figure 20b), although its easternmost extremity corresponds to the present-day location of the Great Meteor hotspot (Figure 5.20c). This means that, although the Great Meteor plume could have been beneath the location of the Rankin kimberlites, it does not underlie Attawapiskat and Kirkland Lake at the time of their emplacement.

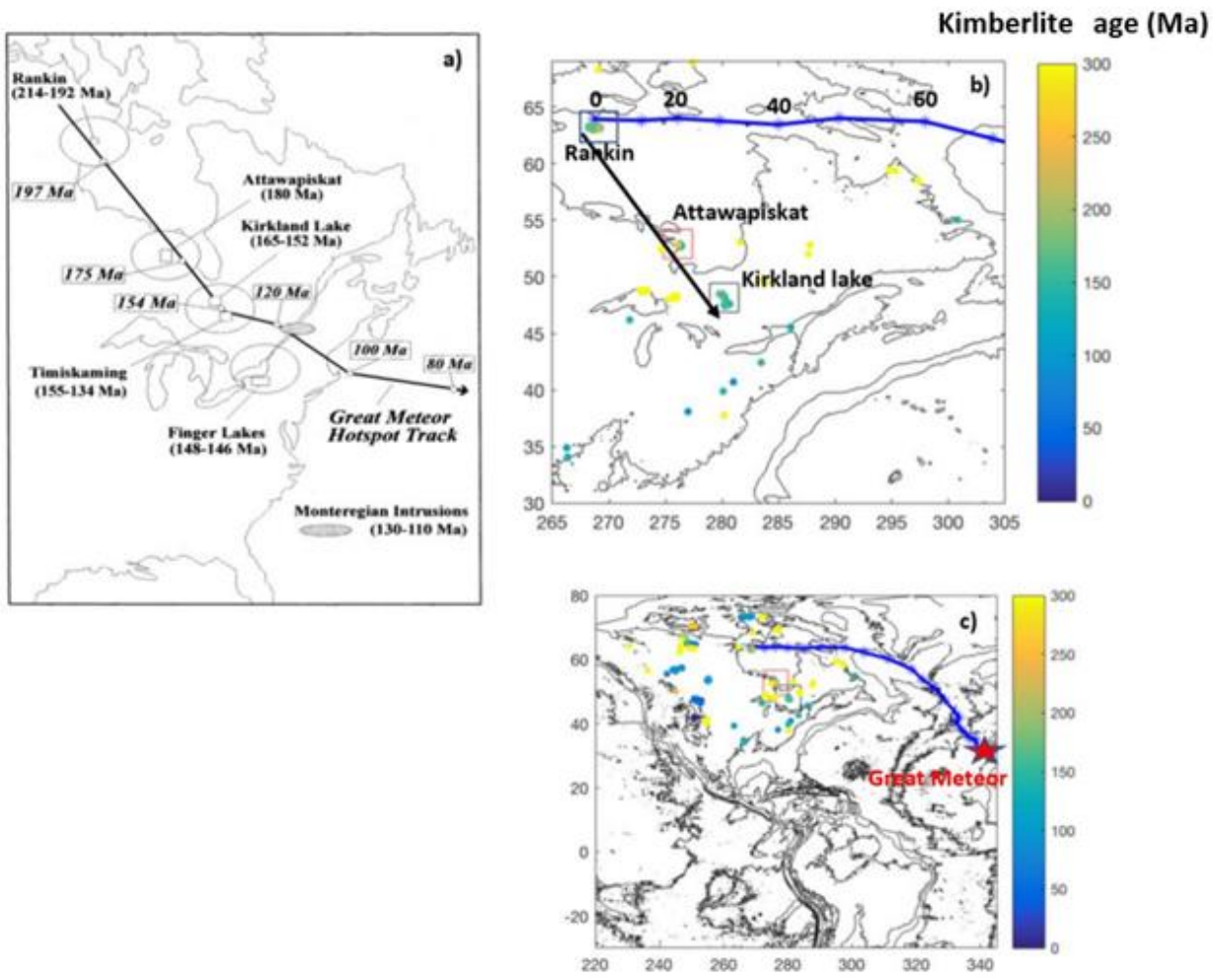

Figure 5.20. Great Meteor hotspot track and the emplacement of Rankin, Attawapiskat, and Kirkland Lake kimberlites.

a) Scenario proposed by Heaman and Kjarsgaard (2000) in which the Great Meteor plume would be at the origin of these kimberlite emplacements. The kimberlite ages are reported. b) Our modeling of the hotspot track that would be at the origin of the emplacement of the Rankin kimberlites (blue line). The ages reported above this track are the time that separates these points from the Rankin emplacement, in millions of years. c) Same as b but considering a larger geographical area, encompassing the present-day location of the Great Meteor plume (red star, from King and Adam, 2014). Computation done with Merdith et al. (2021) rotation poles.

This Great Meteor example shows that computations with recent datasets (e.g., Merdith et al., 2021) do not confirm the hypothesis proposed by Heaman and Kjarsgaard (2000). Other authors, such as Chu et al. (2013), have been invoking the ascent of a plume in the emplacement of kimberlites. Chu et al. (2013) think that there might be a hidden hotspot track in the lower lithosphere of the eastern United States. They use the USArray, a seismic observation network, to image the structures in the lithosphere of the eastern United States. They find that the residual temperature, composition, and P-wave anomalies show that a mantle plume has been interacting with the lithosphere and modified its thermal and mechanical structure. Moreover, Chu et al. (2013) plot a trajectory over the North American plate, which indicates the relative motion between the mantle and the lithosphere. This trajectory encompasses the hotspot track as well as other kimberlites.

However, as indicated by the title of the Chu et al. (2013) paper states, i.e. “the hidden hotspot,” it is difficult to see the surface signature of plumes on the complex North American continental lithosphere. Therefore, it is difficult to test in a systematic way if plumes are likely to entrain kimberlites to the surface. Our results and the literature review points more to the unlikeness of this hypothesis.

Moreover, it is known that mantle plumes can drift. Arnould et al. (2020) model mantle plumes by using spherical models of the mantle convecting. Figure 5.21 shows the percentages of plumes that are stable plumes, slow drifting plumes, and fast drifting plumes. Arnould et al. (2020) show that the fraction of plumes moving less than 0.5 cm per year is greater than 25%. Arnould et al. (2020) also say that a hotspot reference frame, in which the mantle plumes are relatively fixed as the plates move over them, can be defined by choosing the hotspots carefully. Furthermore, their model, which is based on excess temperatures, high speeds, buoyancy, and

heat fluxes of the mantle plumes, shows that plumes have a deflection of less than 10˚. Nevertheless, it is still difficult to prove that the entrainment of kimberlites may have been facilitated by plumes.

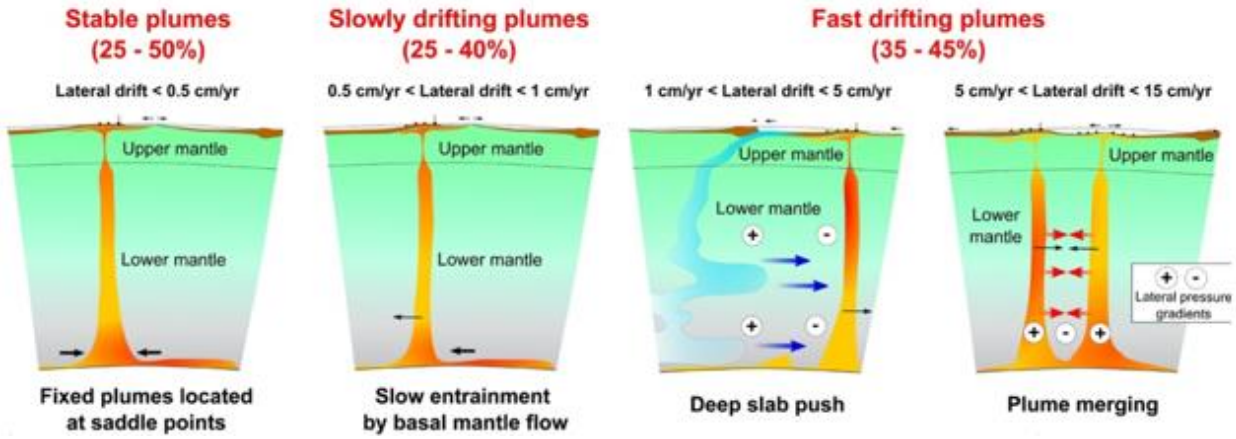

Figure 5.21. The illustration from Arnould et al. (2020) of how plumes drift and the percentages of plumes from the global number of plumes that are related to the different types of plume drifts.

5.5. Temporal evolution between the kimberlites and the mantle

Kimberlites are relatively rare ultramafic igneous rocks that are commonly found within Archean cratons. The distribution of kimberlites over the North American continent is, therefore, puzzling as these kimberlites are emplaced on thick Archean cratonic lithosphere, as well as on thinner Proterozoic lithosphere (Figures 4.5 and 4.6). Kimberlite ages vary between a few million years and 660 Ma (Figure 5.1)

From our results, it seems clear that there is a temporal evolution in the backtracked locations of the kimberlites. The backtracked locations of kimberlites with ages between 110 and 300 Ma correlate with the LLSVPs located below the North Atlantic (Figures 5.3 and 5.8), while the backtracked locations of kimberlites older than 110 Ma correlate with the Pacific LLSVPs (Figures 5.5 and 5.10). The emplacement of the older kimberlites (ages 110-660 Ma) seems to be connected with a deeper mantle source. Indeed, their backtracked positions correlate with the LLSVP locations (Figures 5.3-5.6, 5.8-5.11), and previous studies have already suggested a connection between LLSVPs and kimberlites (Torsvik et al., 2014; Giuliani et al., 2020). However, the studies of the geochemical signature of kimberlites constrain the origin of kimberlites to be sublithospheric. Besides this, several hypotheses have been proposed in the literature to explain the emplacement of kimberlites: mantle plumes (Heaman and Kjarsgaard, 2000), slab-derived fluids (Currie and Beaumont , 2011), LLSVPs (Torsvik et al., 2014; Giuliani et al., 2020), and edge-driven convection (EDC hereafter) (e.g., Kempton et al., 2019). In our present study, the emplacement mechanism appears to have changed with time. EDC seems to be the mechanism that facilitated the generation of the youngest kimberlites in North America (ages < 110 Ma) (Figures 5.18 and 5.19).

When looking at the backtracked location of kimberlites in the Pacific and at their corresponding ages (Figure 4.2), we observe a westward increase of the kimberlites ages. This observation is in agreement with the hypothesis that the kimberlite emplacement is related to deep mantle sources. The westward increase of ages is due to the drift of the North American lithosphere over a fixed mantle source: the LLSVPs. This could also account for the 300-350 Ma quiet period during which no kimberlites have been emplaced over the North American lithosphere. During this period, the lithospheric plate was probably moving from the Pacific LLSVPs towards the North Atlantic LLSVPs. As no buoyant source was bringing kimberlites to the surface, no kimberlites were emplacement during this period.

In the future, it would be interesting to study the temporal evolution of the geochemical signature of the kimberlites, in order to see if there are significant differences between the kimberlites emplaced over the Atlantic LLSVPs and the ones emplaced over the Pacific LLSVPs. Although geochemical studies of kimberlites do exist (e.g., Giuliani) they do not investigate the temporal evolution of the kimberlites' geochemical signature.

Chapter 6 - Conclusion

In Giuliani et al. (2020), it is shown that kimberlites might have come from a long-time storage in the mantle because they contain the component PREMA which many ocean island basalts have and the chemical signatures of PREMA have close similarities with bulk silicate Earth. In addition, Giuliani et al. (2020) show that kimberlites have close connection to the LLSVPs because the depleted kimberlites are backtracked to the locations above the mantle in the LLSVP regions. Such arguments by Tappe et al. (2018), Woodhead et al. (2019), and Giuliani et al. (2020) lead to the thinking that the chemical signature of some of the kimberlites could have originated from the LLSVPs. Tappe et al. (2018), Woodhead et al. (2019), and Giuliani et al. (2020) show using Sr, Nd, and Hf ratios that kimberlites can have depleted mantle sources which are stored in large mantle reservoirs. Kimberlites with depleted mantle signatures might show the evolution of the mantle during an early stage. Partial melting of mantle plumes is also known to generate ocean island basalts (Giuliani et al., 2020). Therefore, it can be inferred that LLSVPs can be a mechanism that brings kimberlite melts closer to the surface. Applying a method of using kinematic models to reconstruct the present-day locations of kimberlites to their locations of emplacement has shown correlations to different possible mechanisms of bringing kimberlite magma to the surface.

In order to provide new insights into the phenomena involved in kimberlite emplacement on the North American continent, we compute the loci of the kimberlites by using the latitudes and longitudes that are found in the Faure et al. (2010) database and by using the rotation poles provided by a new kinematic model (Merdith et al., 2021). We compare the backtracked locations with the location of LLSVPs in the lower mantle, constrained from two widely used tomography models: the SEMUCB-WM1 model, developed by French and

Romanowicz (2014), and the SAVANI model, developed by Auer et al. (2014). We also consider how edge-driven convection may have influenced kimberlite emplacement by investigating the correlation between the present-day kimberlite locations and gradients in the lithosphere-asthenosphere boundary (LAB). For the LAB, we consider the CAM2016 model, developed by Priestley et al. (2019), and the LITHO1.0 model, developed by Pasyanos et al. (2014).

From our reconstructions from kinematic modeling and comparison of the backtracked locations and present-day locations of kimberlites with geophysical models, we find that the phenomena involved in kimberlite emplacement changed over time. Edge-driven convection seems to be the phenomenon that facilitated the emplacement of the youngest kimberlites (ages < 110 Ma), whereas emplacement of the older kimberlites (ages 110-660 Ma) seems to be associated with deep mantle sources, such as the LLSVPs. Indeed when examining the correspondence of the lateral LLSVP data to the Earth'surface, the backtracked positions of the kimberlites show a strong correlation with the LLSVPs. The spatial correlation between the LLSVPs and kimberlite emplacements seem to show that kimberlite melts could have been generated in the mantle above the LLSVPs below the Atlantic Ocean during 110-300 Ma. Similarly for the kimberlites with backtracked locations at the current-day position of the Pacific Ocean basin, the deep mantle that lied in the LLSVP below the Pacific Ocean could have been associated with creating the kimberlite magma. Moreover, the deep mantle associated with kimberlites having ages of 350-400 Ma could now be residing beneath the eastern Pacific as an LLSVPs, while the older ones (ages 400-660 Ma) have been emplaced over the western Pacific LLSVPs. Such patterns are in agreement with the hypothesis that at least some kimberlites are related to deep mantle sources. As the locations of the kimberlites backtracked

to the Pacific Ocean basin show a spatio-temporal age pattern over the LLSVPs, the results seem consistent with mantle having fixed sources with the North American plate drifting over it. Whereas for now, where in the depth on the mantle these fixed sources lie cannot really be determined, in the future, it would be interesting to investigate whether there are geochemical signatures that distinguish kimberlites that may be associated with LLSVPs versus those associated with edge-driven convection. It would also be interesting to examine whether there are significant differences between the kimberlites emplaced over the Atlantic LLSVPs and the ones emplaced over the Pacific LLSVPs.

References

Adam, C., King, S. D., Vidal, V., Rabinowicz, M., Jalobeanu, A., & Yoshida, M. (2015). Variation of the subsidence parameters, effective thermal conductivity, and mantle dynamics. *Earth and Planetary Science Letters*, *426*, 130–142. doi: 10.1016/j.epsl.2015.06.025

Altamimi, Z., Rebischung, P., Métivier, L., & Collilieux, X. (2016). ITRF2014: A new release of the International Terrestrial Reference Frame modeling nonlinear station motions. *Journal of Geophysical Research: Solid Earth*, *121*(8), 6109–6131. doi: 10.1002/2016JB013098

Arnould, M., Coltice, N., Flament, N., & Mallard, C. (2020). Plate tectonics and mantle controls on plume dynamics. *Earth and Planetary Science Letters*, *547*. doi: 10.1016/j.epsl.2020.116439

Artemieva, I. M. (2009). The continental lithosphere: Reconciling thermal, seismic, and petrologic data. *Lithos*, *109*(1-2), 23–46. doi: 10.1016/j.lithos.2008.09.015

Auer, L., Boschi, L., Becker, T. W., Nissen-Meyer, T., & Giardini, D. (2014). Savani: A variable resolution whole-mantle model of anisotropic shear velocity variations based on multiple data sets. *Journal of Geophysical Research: Solid Earth*, *119*(4), 3006–3034. doi: 10.1002/2013JB010773

Ballmer, M. D., Conrad, C. P., Smith, E. I., & Johnsen, R. (2015). Intraplate volcanism at the edges of the Colorado Plateau sustained by a combination of triggered edge-driven convection and shear-driven upwelling. *Geochemistry, Geophysics, Geosystems*, *16*(2), 366–379. doi: 10.1002/2014GC005641

Barnett, W., Jelsma, H., Watkeys, M., Freeman, L., & Bloem, A. (2013). How Structure and Stress Influence Kimberlite Emplacement. In D. G. Pearson, H. S. Grütter, J. W. Harris, B. A. Kjarsgaard, H. O'Brien, N. V. C. Rao, & S. Sparks (Eds.), *Proceedings of 10th International Kimberlite Conference* (pp. 51–65). Springer India. doi: 10.1007/978-81-322-1173-0_4

Boyden, J., Müller, R. D., Gurnis, M., Torsvik, T. H., Clark, J. A., Turner, M., Ivey-Law, H., Watson, R. J., & Cannon, J. S. (2011). Next-generation plate-tectonic reconstructions using GPlates. In G.R. Keller, & C. Baru (Eds.), In *Geoinformatics: Cyberinfrastructure for the Solid Earth Sciences*(pp.95-114). Cambridge: Cambridge University Press.

Burke, K. (2011). Plate Tectonics, the Wilson Cycle, and Mantle Plumes: Geodynamics from the Top. *Annual Review of Earth and Planetary Sciences*, *39*(1), 1–29. doi: 10.1146/annurev-earth-040809-152521

Chu, R., Leng, W., Helmberger, D. V., & Gurnis, M. (2013). Hidden hotspot track beneath the eastern United States. *Nature Geoscience*, *6*(11), 963-966. doi: 10.1038/ngeo1949

Courtillot, V., Davaille, A., Besse, J., & Stock, J. (2003). Three distinct types of hotspots in the Earth's mantle. *Earth and Planetary Science Letters*, *205*(3), 295–308. doi: 10.1016/S0012-821X(02)01048-8

Cox, A., & Hart, R. B. (1986). *Plate tectonics: How it works*. Blackwell Scientific Publications, Inc.

Crough, S. T. (1981). Mesozoic hotspot epeirogeny in eastern North America. *Geology*, *9*(1), 2–6. doi: 10.1130/0091-7613(1981)9<2:MHEIEN>2.0.CO;2

Crough, S. T., Morgan, W. J., & Hargraves, R. B. (1980). Kimberlites: Their relation to mantle hotspots. *Earth and Planetary Science Letters*, *50*(1), 260–274. doi: 10.1016/0012-821X(80)90137-5

Currie, C. A., & Beaumont, C. (2011). Are diamond-bearing Cretaceous kimberlites related to low-angle subduction beneath western North America? *Earth and Planetary Science Letters*, *303*(1), 59–70. doi: 10.1016/j.epsl.2010.12.036

Davaille, A. (1999). Simultaneous generation of hotspots and superswells by convection in a heterogeneous planetary mantle. *Nature*, *402*(6763), 756-760. doi: 10.1038/45461

Davaille, A., & Romanowicz, B. (2020). Deflating the LLSVPs: Bundles of mantle thermochemical plumes rather than thick stagnant "piles." *Tectonics*, *39*(10), e2020TC006265. doi: 10.1029/2020TC006265

Davies, D. R., Goes, S., & Lau, H. C. P. (2015). Thermally dominated deep mantle LLSVPs: A review. In A. Khan & F. Deschamps (Eds.), *The Earth's Heterogeneous Mantle: A Geophysical, Geodynamical, and Geochemical Perspective* (pp. 441–477). Springer International Publishing. doi: 10.1007/978-3-319-15627-9_14

DeMets, C., Gordon, R. G., & Argus, D. F. (2010). Geologically current plate motions. *Geophysical Journal International*, *181*(1), 1–80. doi: 10.1111/j.1365-246X.2009.04491.x

Domeier, M., Van der Voo, R., & Torsvik, T. H. (2012). Paleomagnetism and Pangea: The road to reconciliation. *Tectonophysics*, *514–517*, 14–43. doi: 10.1016/j.tecto.2011.10.021

Doubrovine, P. V., Steinberger, B., & Torsvik, T. H. (2012). Absolute plate motions in a reference frame defined by moving hot spots in the Pacific, Atlantic, and Indian oceans. *Journal of Geophysical Research: Solid Earth*, *117*(B9). doi: 10.1029/2011JB009072

Doubrovine, P. V., Steinberger, B., & Torsvik, T. H. (2016). A failure to reject: Testing the correlation between large igneous provinces and deep mantle structures with EDF statistics. *Geochemistry, Geophysics, Geosystems*, *17*(3), 1130–1163. doi: 10.1002/2015GC006044

Dziewonski, A. M., Lekic, V., & Romanowicz, B. A. (2010). Mantle anchor structure: An argument for bottom up tectonics. *Earth and Planetary Science Letters*, *299*(1), 69–79. doi: 10.1016/j.epsl.2010.08.013

England, P., & Houseman, G. (1984). On the geodynamic setting of kimberlite genesis. *Earth and Planetary Science Letters*, *67*(1), 109–122. doi: 10.1016/0012-821X(84)90043-8

Faure, S. (2010). *World kimberlites CONSOREM database.* Université du Québec à Montréal. http://www.consorem.ca.

Flament, N. (2010). Secular cooling of the solid Earth, emergence of the continents, and evolution of Earth's external envelopes. *University of Sydney and University of Lyon*.

Foley, S. F. (2011). A reappraisal of redox melting in the Earth's mantle as a function of tectonic setting and time. *Journal of Petrology*, *52*(7–8), 1363–1391. doi: 10.1093/petrology/egq061

Francis, D., & Patterson, M. (2009). Kimberlites and aillikites as probes of the continental lithospheric mantle. *Lithos*, *109*(1), 72–80. doi: 10.1016/j.lithos.2008.05.007

French, S. W., & Romanowicz, B. A. (2014). Whole-mantle radially anisotropic shear velocity structure from spectral-element waveform tomography. *Geophysical Journal International*, *199*(3), 1303–1327. doi: 10.1093/gji/ggu334

Ganne, J., & Feng, X. (2017). Primary magmas and mantle temperatures through time. *Geochemistry, Geophysics, Geosystems*, *18*(3), 872–888. doi: 10.1002/2016GC006787

Garnero, E. J., Kennett, B., & Loper, D. E. (2005). Studies of the Earth's deep interior—eighth symposium. *Physics of the Earth and Planetary Interiors*, *153*(1), 1–2. doi: 10.1016/j.pepi.2005.08.003

Giuliani, A., Jackson, M. G., Fitzpayne, A., & Dalton, H. (2020). Remnants of early Earth differentiation in the deepest mantle-derived lavas. *Proceedings of the National Academy of Sciences*, *118*(1). doi: 10.1073/pnas.2015211118

Golovin, A. V., Sharygin, I. S., Kamenetsky, V. S., Korsakov, A. V., & Yaxley, G. M. (2018). Alkali-carbonate melts from the base of cratonic lithospheric mantle: Links to kimberlites. *Chemical Geology*, *483*, 261–274. doi: 10.1016/j.chemgeo.2018.02.016

Grégoire, M., Rabinowicz, M., & Janse, A. J. A. (2006). Mantle mush compaction: A key to understand the mechanisms of concentration of kimberlite melts and initiation of swarms of kimberlite dykes. *Journal of Petrology*, *47*(3), 631–646. doi: 10.1093/petrology/egi090

Heaman, L., Kjarsgaard, B., & Creaser, R. (2003). The timing of kimberlite magmatism in North America: Implications for global kimberlite genesis and diamond exploration. *Lithos*, *71*(2), 153–184. doi: 10.1016/j.lithos.2003.07.005

Heaman, L. M., & Kjarsgaard, B. A. (2000). Timing of eastern North American kimberlite magmatism: Continental extension of the Great Meteor hotspot track? *Earth and Planetary Science Letters*, *178*(3), 253–268. doi: 10.1016/S0012-821X(00)00079-0

Heaman, L. M., Pell, J., Grütter, H. S., & Creaser, R. A. (2015). U–Pb geochronology and Sr/Nd isotope compositions of groundmass perovskite from the newly discovered Jurassic Chidliak kimberlite field, Baffin Island, Canada. *Earth and Planetary Science Letters*, *415*, 183–199. doi: 10.1016/j.epsl.2014.12.056

Hofmann, A. W. (1988). Chemical differentiation of the Earth: The relationship between mantle, continental crust, and oceanic crust. *Earth and Planetary Science Letters*, *90*(3), 297–314. doi: 10.1016/0012-821X(88)90132-X

Ito, G., & van Keken, P. E. (2007). Hotspots and melting anomalies. *Treatise on Geophysics*, 7, 371-436.

Jellinek, A. M., & Manga, M. (2004). Links between long-lived hot spots, mantle plumes, D″, and plate tectonics. *Reviews of Geophysics*, *42*(3). doi: 10.1029/2003RG000144

Jollands, M. C., Hanger, B. J., Yaxley, G. M., Hermann, J., & Kilburn, M. R. (2018). Timescales between mantle metasomatism and kimberlite ascent indicated by diffusion profiles in garnet crystals from peridotite xenoliths. *Earth and Planetary Science Letters*, *481*, 143–153. doi: 10.1016/j.epsl.2017.10.021

Kellogg, L. H., Hager, B. H., & Hilst, R. D. van der. (1999). Compositional Stratification in the Deep Mantle. *Science*, *283*(5409), 1881-1884. doi: 10.1126/science.283.5409.1881

Kempton, P. D., Rogers, K., & Brueseke, M. E. (2019). Windows into the Cretaceous mantle of the North American midcontinent—Kimberlites of Riley County, Kansas. In M. K. Schulmeister & J. S. Aber (Eds.), *Exploring Extreme and Unusual Geology in the Stable Midcontinent: Field Excursions for the 2019 GSA South-Central, North-Central, and Rocky Mountain Sections Joint Meeting* (Vol. 52, p. 0). Geological Society of America. doi: 10.1130/2019.0052(03)

King, S. D., & Adam, C. (2014). Hotspot swells revisited. *Physics of the Earth and Planetary Interiors*, *235*, 66–83. doi: 10.1016/j.pepi.2014.07.006

King, S. D., & Anderson, D. L. (1998). Edge-driven convection. *Earth and Planetary Science Letters*, *160*(3), 289–296. doi: 10.1016/S0012-821X(98)00089-2

Kjarsgaard, B. A., Heaman, L. M., Sarkar, C., & Pearson, D. G. (2017). The North America mid-Cretaceous kimberlite corridor: Wet, edge-driven decompression melting of an OIB-type deep mantle source. *Geochemistry, Geophysics, Geosystems*, *18*(7), 2727–2747. doi: 10.1002/2016GC006761

Kopylova, M. G., & Caro, G. (2004). Mantle xenoliths from the southeastern Slave Craton: Evidence for chemical zonation in a thick, cold lithosphere. *Journal of Petrology*, *45*(5), 1045–1067. doi: 10.1093/petrology/egh003

Kreemer, C., Blewitt, G., & Klein, E. C. (2014). A geodetic plate motion and Global Strain Rate Model. *Geochemistry, Geophysics, Geosystems*, *15*(10), 3849–3889. doi: 10.1002/2014GC005407

Kreielkamp, P., Stein, C., & Hansen, U. (2022). LLSVPs of primordial origin: Implications for the evolution of plate tectonics. *Earth and Planetary Science Letters*, *579*. doi: 10.1016/j.epsl.2021.117357

Liu, J., Brin, L. E., Graham Pearson, D., Bretschneider, L., Luguet, A., van Acken, D., Kjarsgaard, B., Riches, A., & Mišković, A. (2018). Diamondiferous Paleoproterozoic mantle roots beneath Arctic Canada: A study of mantle xenoliths from Parry Peninsula and Central Victoria Island. *Geochimica et Cosmochimica Acta*, *239*, 284–311. doi: 10.1016/j.gca.2018.08.010

Manjón-Cabeza Córdoba, A., & Ballmer, M. D. (2021). The role of edge-driven convection in the generation of volcanism – Part 1: A 2D systematic study. *Solid Earth*, *12*(3), 613–632. doi: 10.5194/se-12-613-2021

Matthews, K. J., Maloney, K. T., Zahirovic, S., Williams, S. E., Seton, M., & Müller, R. D. (2016). Global plate boundary evolution and kinematics since the late Paleozoic. *Global and Planetary Change*, *146*, 226–250. doi: 10.1016/j.gloplacha.2016.10.002

McNamara, A. K. (2019). A review of large low shear velocity provinces and ultra low velocity zones. *Tectonophysics*, *760*, 199–220. doi: 10.1016/j.tecto.2018.04.015

Merdith, A. S., Williams, S. E., Collins, A. S., Tetley, M. G., Mulder, J. A., Blades, M. L., Young, A., Armistead, S. E., Cannon, J., Zahirovic, S., & Müller, R. D. (2021). Extending full-plate tectonic models into deep time: Linking the Neoproterozoic and the Phanerozoic. *Earth-Science Reviews*, *214*(103477). doi: 10.1016/j.earscirev.2020.103477

Mitchell, R. (2008). Advances in kimberlite geology and petrology. *Memoir*, *66*, 423–461.

Mitchell, R. H. (1991). Kimberlites and lamproites: Primary sources of diamond. *Geoscience Canada*, *18*.

Müller, R. D., Cannon, J., Qin, X., Watson, R. J., Gurnis, M., Williams, S., Pfaffelmoser, T., Seton, M., Russell, S. H. J., & Zahirovic, S. (2018). GPlates: Building a virtual Earth through deep time. *Geochemistry, Geophysics, Geosystems*, *19*(7), 2243–2261. doi: 10.1029/2018GC007584

Müller, R. D., Seton, M., Zahirovic, S., Williams, S. E., Matthews, K. J., Wright, N. M., Shephard, G. E., Maloney, K. T., Barnett-Moore, N., Hosseinpour, M., Bower, D. J., & Cannon, J. (2016). Ocean basin evolution and global-scale plate reorganization events since Pangea breakup. *Annual Review of Earth and Planetary Sciences*, *44*(1), 107–138. doi: 10.1146/annurev-earth-060115-012211

Müller, R. D., Zahirovic, S., Williams, S. E., Cannon, J., Seton, M., Bower, D. J., Tetley, M. G., Heine, C., Le Breton, E., Liu, S., Russell, S. H. J., Yang, T., Leonard, J., & Gurnis, M. (2019). A global plate model including lithospheric deformation along major rifts and orogens since the Triassic. *Tectonics*, *38*(6), 1884–1907. doi: 10.1029/2018TC005462

Mulyukova, E., Steinberger, B., Dabrowski, M., & Sobolev, S. V. (2015). Survival of LLSVPs for billions of years in a vigorously convecting mantle: Replenishment and destruction of chemical anomaly. *Journal of Geophysical Research: Solid Earth*, *120*(5), 3824–3847. doi: 10.1002/2014JB011688

Niu, Y. (2018). Origin of the LLSVPs at the base of the mantle is a consequence of plate tectonics – A petrological and geochemical perspective. *Geoscience Frontiers*, *9*(5), 1265–1278. doi: 10.1016/j.gsf.2018.03.005

Niu, Y., & O'Hara, M. J. (2003). Origin of ocean island basalts: A new perspective from petrology, geochemistry, and mineral physics considerations. *Journal of Geophysical Research: Solid Earth*, *108*(B4). doi: 10.1029/2002JB002048

Pasyanos, M. E., Masters, T. G., Laske, G., & Ma, Z. (2014). LITHO1.0: An updated crust and lithospheric model of the Earth. *Journal of Geophysical Research: Solid Earth*, *119*(3), 2153–2173. doi: 10.1002/2013JB010626

Pearson, D. G., Woodhead, J., & Janney, P. E. (2019). Kimberlites as geochemical probes of Earth's mantle. *Elements*, *15*(6), 387–392. doi: 10.2138/gselements.15.6.387

Pell, J. A., & Ijewliw, O. J. (2003). Kimberlites, melnoites and look-alikes in British Columbia, Canada. *International Kimberlite Conference: Extended Abstracts*, *8*. doi: 10.29173/ikc3127

Priestley, K., McKenzie, D., & Ho, T. (2018). A lithosphere-asthenosphere boundary—A global model derived from multi-mode surface wave tomography and petrology. *Lithospheric discontinuities*. 111-123. doi: 10.1002/9781119249740.ch6

Russell, J. K., Porritt, L. A., Lavallée, Y., & Dingwell, D. B. (2012). Kimberlite ascent by assimilation-fuelled buoyancy. *Nature*, *481*(7381). doi: 10.1038/nature10740

Sleep, N. H. (1990). Monteregian hotspot track: A long-lived mantle plume. *Journal of Geophysical Research: Solid Earth*, *95*(B13), 21983–21990. doi: 10.1029/JB095iB13p21983

Smit, K., & Shirey, S. (2019). Kimberlites: Earth's diamond delivery system. *Gems and Gemology*, *55*, 270–276.

Stamm, N., & Schmidt, M. W. (2017). Asthenospheric kimberlites: Volatile contents and bulk compositions at 7 GPa. *Earth and Planetary Science Letters*, *474*, 309–321. doi: 10.1016/j.epsl.2017.06.037

Stern, R. J., Leybourne, M. I., & Tsujimori, T. (2016). Kimberlites and the start of plate tectonics. *Geology*, *44*(10), 799–802. doi: 10.1130/G38024.1

Stracke, A., Willig, M., Genske, F., Béguelin, P., & Todd, E. (2022). Chemical geodynamics insights from a machine learning approach. *Geochemistry, Geophysics, Geosystems*, *23*(10). doi: 10.1029/2022GC010606

Tappe, S., Brand, N. B., Stracke, A., van Acken, D., Liu, C. Z., Strauss, H., Wu, F. Y., Luguet, A., & Mitchell, R. H. (2017). Plates or plumes in the origin of kimberlites: U/Pb perovskite and Sr-Nd-Hf-Os-C-O isotope constraints from the Superior craton (Canada). *Chemical Geology*, *455*, 57–83. doi: 10.1016/j.chemgeo.2016.08.019

Tappe, S., Dongre, A., Liu, C. Z., & Wu, F. Y. (2018). “Premier” evidence for prolonged kimberlite pipe formation and its influence on diamond transport from deep Earth. *Geology*, *46*, 843–846. doi: 10.1130/G45097.1

Tappe, S., Kjarsgaard, B. A., Kurszlaukis, S., Nowell, G. M., & Phillips, D. (2014). Petrology and Nd–Hf isotope geochemistry of the Neoproterozoic Amon kimberlite sills, Baffin Island (Canada): Evidence for deep mantle magmatic activity linked to supercontinent cycles. *Journal of Petrology*, *55*(10), 2003–2042. doi: 10.1093/petrology/egu048

Tappe, S., Smart, K., Torsvik, T., Massuyeau, M., & de Wit, M. (2018). Geodynamics of kimberlites on a cooling Earth: Clues to plate tectonic evolution and deep volatile cycles. *Earth and Planetary Science Letters*, *484*, 1–14. doi: 10.1016/j.epsl.2017.12.013

Torsvik, T. H., Steinberger, B., Ashwal, L. D., Doubrovine, P. V., & Trønnes, R. G. (2016). Earth evolution and dynamics—a tribute to Kevin Burke. *Canadian Journal of Earth Sciences*, *53*(11), 1073–1087. doi: 10.1139/cjes-2015-0228

Torsvik, T. H., & Van der Voo, R. (2002). Refining Gondwana and Pangea palaeogeography: Estimates of Phanerozoic non-dipole (octupole) fields. *Geophysical Journal International*, *151*(3), 771–794. doi: 10.1046/j.1365-246X.2002.01799.x

Torsvik, T. H., van der Voo, R., Doubrovine, P. V., Burke, K., Steinberger, B., Ashwal, L. D., Trønnes, R. G., Webb, S. J., & Bull, A. L. (2014). Deep mantle structure as a reference frame for movements in and on the Earth. *Proceedings of the National Academy of Sciences*, *111*(24), 8735–8740. doi: 10.1073/pnas.1318135111

Torsvik, T. H., Van der Voo, R., Preeden, U., Mac Niocaill, C., Steinberger, B., Doubrovine, P. V., van Hinsbergen, D. J. J., Domeier, M., Gaina, C., Tohver, E., Meert, J. G., McCausland, P. J. A., & Cocks, L. R. M. (2012). Phanerozoic polar wander,

palaeogeography and dynamics. *Earth-Science Reviews*, *114*(3), 325–368. doi: 10.1016/j.earscirev.2012.06.007

Tozer, B., Sandwell, D. T., Smith, W. H. F., Olson, C., Beale, J. R., & Wessel, P. (2019). Global bathymetry and topography at 15 arc sec: SRTM15+. *Earth and Space Science*, *6*(10), 1847–1864. doi: 10.1029/2019EA000658

Wilson, L., & Head, J. W. (2007). An integrated model of kimberlite ascent and eruption. *Nature*, *447*(7140), 53-57. doi: 0.1038/nature05692

Woodhead, J., Hergt, J., Giuliani, A., Maas, R., Phillips, D., Pearson, D. G., & Nowell, G. (2019). Kimberlites reveal 2.5-billion-year evolution of a deep, isolated mantle reservoir. *Nature*, *573*, 578-581. doi: 10.1038/s41586-019-1574-8

Yaxley, G. M., Berry, A. J., Rosenthal, A., Woodland, A. B., & Paterson, D. (2017). Redox preconditioning deep cratonic lithosphere for kimberlite genesis – evidence from the central Slave Craton. *Scientific Reports*, *7*(1). doi: 10.1038/s41598-017-00049-3

Young, A., Flament, N., Maloney, K., Williams, S., Matthews, K., Zahirovic, S., & Müller, R. D. (2019). Global kinematics of tectonic plates and subduction zones since the late Paleozoic Era. *Geoscience Frontiers*, *10*(3), 989–1013. doi: 10.1016/j.gsf.2018.05.011

Zindler, A., & Hart, S. (1986). Chemical geodynamics. *Annual Review of Earth and Planetary Sciences*, *14*(1), 493–571. doi: 10.1146/annurev.ea.14.050186.002425

Appendix A - Table of kimberlite locations, rock types, minimum and maximum kimberlites ages, and sources

Rock types :

1- Kimberlite
2- Lamproite
3- Ultramafic Lamprophyre (UML)
4- Melilitite
5- Lamprophyre
6- Mafic Lamprophyre
7- Kimberlite and Lamproite

Volcanics and Lamproites

Table A.1. Table showing kimberlite locations, rock types, minimum and maximum ages, and sources.

Longitude	Latitude	Rock type	Minimum age (Ma)	Maximum age (Ma)	Sources
-129.478	64.241	1	428	462	Faure et al. (2010)
-117.717	55.459	1	65	85	Faure et al. (2010)
-117.715	55.454	1	69	87	Faure et al. (2010)
-115.873	56.702	1	86	94	Faure et al. (2010)
-115.872	56.862	1	86	104	Faure et al. (2010)
-115.865	56.831	1	86	105	Faure et al. (2010)
-115.864	56.704	1	86	95	Faure et al. (2010)
-115.751	56.777	1	86	103	Faure et al. (2010)
-115.662	56.784	1	86	98	Faure et al. (2010)
-115.657	56.656	1	86	89	Faure et al. (2010)
-115.646	56.894	1	84	90	Faure et al. (2010)
-115.641	56.896	1	84	90	Faure et al. (2010)
-115.636	56.974	1	83	93	Faure et al. (2010)
-115.633	56.978	1	86	101	Faure et al. (2010)
-115.632	56.939	1	83	89	Faure et al. (2010)
-115.608	56.92	1	86	102	Faure et al. (2010)
-115.51	56.656	1	86	106	Faure et al. (2010)

-115.423	56.848	1	86	97	Faure et al. (2010)
-115.131	56.984	1	86	100	Faure et al. (2010)
-115.123	56.974	1	86	99	Faure et al. (2010)
-115.013	56.341	1	86	88	Faure et al. (2010)
-114.969	50.092	1	235	246	Faure et al. (2010)
-114.87	56.843	1	86	96	Faure et al. (2010)
-114.855	56.947	1	86	107	Faure et al. (2010)
-114.842	56.955	1	86	90	Faure et al. (2010)
-114.826	56.915	1	86	92	Faure et al. (2010)
-113.833	62.14	1	440.6	442.2	Faure et al. (2010)
-113.478	57.338	1	71.5	73.3	Faure et al. (2010)
-113.46	57.37	1	68.7	71.9	Faure et al. (2010)
-113.375	64.33	1	450	450	Faure et al. (2010)
-113.358	63.466	1	459	463	Faure et al. (2010)
-113.299	63.558	1	448.2	452.6	Faure et al. (2010)
-113.292	63.521	1	435.4	435.4	Faure et al. (2010)
-113.286	57.323	1	73.1	78.5	Faure et al. (2010)
-113.242	57.343	1	86	91	Faure et al. (2010)
-113.202	67.139	1	170	170	Faure et al. (2010)
-113.182	57.307	1	77.8	81	Faure et al. (2010)
-113.088	57.442	1	86	93	Faure et al. (2010)
-113.041	57.254	1	70.5	74.7	Faure et al. (2010)
-112.95	66.554	1	607	619	Faure et al. (2010)
-112.886	66.56	1	613	613	Faure et al. (2010)
-112.883	57.196	1	76.8	78.4	Faure et al. (2010)
-112.777	67.164	1	170	170	Faure et al. (2010)
-111.51	65.273	1	51.8	52.4	Faure et al. (2010)
-111.467	66.014	1	172.8	174.4	Faure et al. (2010)
-111.105	64.65	1	56.4	61	Faure et al. (2010)
-111.099	64.648	1	59	63.2	Faure et al. (2010)
-111.041	64.864	1	47	74	Faure et al. (2010)
-111.034	64.56	1	47	74	Faure et al. (2010)
-111.022	65.025	1	56	100.5	Faure et al. (2010)
-111.019	64.976	1	47	74	Faure et al. (2010)
-111.016	65.153	1	47	74	Faure et al. (2010)
-111.014	65.001	1	47	74	Faure et al. (2010)
-111.008	65.024	1	47	74	Faure et al. (2010)
-110.994	65.136	1	47	74	Faure et al. (2010)
-110.988	65.019	1	47	74	Faure et al. (2010)
-110.99	65.168	1	47	74	Faure et al. (2010)
-110.981	64.886	1	59.3	60.1	Faure et al. (2010)
-110.978	64.891	1	58.2	61.2	Faure et al. (2010)
-110.967	64.686	1	47	74	Faure et al. (2010)

-110.963	65.002	1	47	74	Faure et al. (2010)
-110.919	64.882	1	47	74	Faure et al. (2010)
-110.913	64.471	1	47	74	Faure et al. (2010)
-110.908	64.902	1	60.5	67.3	Faure et al. (2010)
-110.901	64.499	1	47	74	Faure et al. (2010)
-110.896	64.498	1	47	74	Faure et al. (2010)
-110.895	65.034	1	47	74	Faure et al. (2010)
-110.895	64.569	1	47	74	Faure et al. (2010)
-110.893	64.464	1	47	74	Faure et al. (2010)
-110.889	64.892	1	47	74	Faure et al. (2010)
-110.862	63.609	1	516.1	529.9	Faure et al. (2010)
-110.826	64.893	1	47	74	Faure et al. (2010)
-110.818	63.636	1	540	540	Faure et al. (2010)
-110.802	63.591	1	550	550	Faure et al. (2010)
-110.79	64.931	1	47	74	Faure et al. (2010)
-110.774	64.514	1	47	74	Faure et al. (2010)
-110.772	64.477	1	47	74	Faure et al. (2010)
-110.769	64.51	1	47	74	Faure et al. (2010)
-110.75	64.489	1	47	74	Faure et al. (2010)
-110.728	63.593	1	516	529.8	Faure et al. (2010)
-110.693	64.634	1	47	74	Faure et al. (2010)
-110.68	64.658	1	54.8	56.1	Faure et al. (2010)
-110.659	64.846	1	51.1	53.1	Faure et al. (2010)
-110.66	64.682	1	45.4	58.6	Faure et al. (2010)
-110.654	64.757	1	47	74	Faure et al. (2010)
-110.643	64.849	1	47	74	Faure et al. (2010)
-110.606	64.716	1	52.4	56	Faure et al. (2010)
-110.6	64.723	1	52.4	54.2	Faure et al. (2010)
-110.586	64.726	1	52.6	59.4	Faure et al. (2010)
-110.581	64.737	1	52.1	54.1	Faure et al. (2010)
-110.551	64.725	1	46	55.6	Faure et al. (2010)
-110.543	64.697	1	58.5	76.7	Faure et al. (2010)
-110.537	64.851	1	53.2	63.4	Faure et al. (2010)
-110.513	64.861	1	47	74	Faure et al. (2010)
-110.505	64.778	1	49.8	53.2	Faure et al. (2010)
-110.47	64.909	1	47	74	Faure et al. (2010)
-110.468	64.74	1	57.5	59.3	Faure et al. (2010)
-110.45	64.913	1	47	74	Faure et al. (2010)
-110.447	64.918	1	47	74	Faure et al. (2010)
-110.383	65.022	1	47	74	Faure et al. (2010)
-110.422	64.812	1	47	74	Faure et al. (2010)
-110.413	64.934	1	47	74	Faure et al. (2010)
-110.378	64.674	1	52	53.6	Faure et al. (2010)

-110.355	64.468	1	47	74	Faure et al. (2010)
-110.352	64.696	1	46.2	48	Faure et al. (2010)
-110.35	64.954	1	47	74	Faure et al. (2010)
-110.347	64.715	1	43.9	46.5	Faure et al. (2010)
-110.344	64.704	1	47	48	Faure et al. (2010)
-110.311	64.403	1	47	74	Faure et al. (2010)
-110.311	64.458	1	47	74	Faure et al. (2010)
-110.308	64.72	1	45.9	49.1	Faure et al. (2010)
-110.292	64.465	1	47	74	Faure et al. (2010)
-110.29	64.469	1	53.6	57.8	Faure et al. (2010)
-110.278	64.488	1	47	74	Faure et al. (2010)
-110.261	64.438	1	47	74	Faure et al. (2010)
-110.262	64.433	1	47	74	Faure et al. (2010)
-110.255	64.753	1	46.7	49.3	Faure et al. (2010)
-110.245	64.484	1	54.9	55.5	Faure et al. (2010)
-110.237	64.5	1	54.8	56.2	Faure et al. (2010)
-110.233	64.502	1	54.5	56.7	Faure et al. (2010)
-110.228	64.504	1	47	74	Faure et al. (2010)
-110.222	64.548	1	51	60.6	Faure et al. (2010)
-110.201	64.825	1	57.1	61.9	Faure et al. (2010)
-110.181	64.4	1	47	74	Faure et al. (2010)
-110.177	64.561	1	54.8	56.2	Faure et al. (2010)
-110.172	64.641	1	62.7	75.5	Faure et al. (2010)
-110.169	64.835	1	61.3	66.5	Faure et al. (2010)
-110.167	64.821	1	64.4	72	Faure et al. (2010)
-110.149	64.747	1	45.8	50	Faure et al. (2010)
-110.148	64.349	1	47	74	Faure et al. (2010)
-110.147	64.829	1	67.9	81.5	Faure et al. (2010)
-110.144	64.35	1	47	74	Faure et al. (2010)
-110.142	64.584	1	50.7	52.3	Faure et al. (2010)
-110.139	64.758	1	47	74	Faure et al. (2010)
-110.137	70.569	1	256	286	Faure et al. (2010)
-110.134	64.727	1	47	74	Faure et al. (2010)
-110.111	64.616	1	64	75	Faure et al. (2010)
-110.126	64.483	1	47	74	Faure et al. (2010)
-110.124	64.783	1	47	74	Faure et al. (2010)
-110.111	64.737	1	53.6	55.6	Faure et al. (2010)
-110.109	64.803	1	46.4	49.2	Faure et al. (2010)
-110.104	64.697	1	47	74	Faure et al. (2010)
-110.106	64.764	1	47	74	Faure et al. (2010)
-110.103	70.558	1	256	286	Faure et al. (2010)
-110.099	64.473	1	47	74	Faure et al. (2010)
-110.105	64.548	1	56.7	60.1	Faure et al. (2010)

-110.105	64.534	1	57.9	64.7	Faure et al. (2010)
-110.096	70.555	1	256	286	Faure et al. (2010)
-110.078	64.489	1	47	74	Faure et al. (2010)
-110.056	64.476	1	47	74	Faure et al. (2010)
-110.037	64.593	1	52.9	56.7	Faure et al. (2010)
-110.017	64.456	1	47	74	Faure et al. (2010)
-110.013	64.449	1	47	74	Faure et al. (2010)
-110.002	64.451	1	47	74	Faure et al. (2010)
-110.006	64.594	1	47	74	Faure et al. (2010)
-110.001	70.807	1	256	286	Faure et al. (2010)
-109.995	64.442	1	47	74	Faure et al. (2010)
-109.98	64.856	1	73	73	Faure et al. (2010)
-109.963	64.808	1	47	74	Faure et al. (2010)
-109.964	70.795	1	256	286	Faure et al. (2010)
-109.954	64.807	1	47	74	Faure et al. (2010)
-109.953	70.52	1	256	286	Faure et al. (2010)
-109.951	64.826	1	71	71	Faure et al. (2010)
-109.938	70.516	1	256	286	Faure et al. (2010)
-109.933	70.787	1	256	286	Faure et al. (2010)
-109.928	64.354	1	47	74	Faure et al. (2010)
-109.92	64.795	1	47	74	Faure et al. (2010)
-109.917	64.408	1	47	74	Faure et al. (2010)
-109.894	64.704	1	70.5	70.5	Faure et al. (2010)
-109.88	70.778	1	256	286	Faure et al. (2010)
-109.874	70.499	1	256	286	Faure et al. (2010)
-109.885	64.7	1	47	74	Faure et al. (2010)
-109.862	64.542	1	47	74	Faure et al. (2010)
-109.857	64.314	1	47	74	Faure et al. (2010)
-109.857	64.318	1	47	74	Faure et al. (2010)
-109.854	64.411	1	70.5	76.9	Faure et al. (2010)
-109.852	64.306	1	47	74	Faure et al. (2010)
-109.85	64.322	1	47	74	Faure et al. (2010)
-109.849	64.845	1	72	72	Faure et al. (2010)
-109.834	70.493	1	256	286	Faure et al. (2010)
-109.823	64.417	1	47	74	Faure et al. (2010)
-109.823	64.435	1	47	74	Faure et al. (2010)
-109.817	64.785	1	47	74	Faure et al. (2010)
-109.817	64.326	1	74	74	Faure et al. (2010)
-109.816	64.333	1	75	75	Faure et al. (2010)
-109.814	70.74	1	256	286	Faure et al. (2010)
-109.81	70.486	1	256	286	Faure et al. (2010)
-109.8	70.484	1	256	286	Faure et al. (2010)
-109.796	64.728	1	73	73	Faure et al. (2010)

-109.788	70.752	1	256	286	Faure et al. (2010)
-109.785	70.478	1	256	286	Faure et al. (2010)
-109.779	64.888	1	47	74	Faure et al. (2010)
-109.778	70.74	1	256	286	Faure et al. (2010)
-109.759	70.473	1	256	286	Faure et al. (2010)
-109.711	70.717	1	256	286	Faure et al. (2010)
-109.71	64.706	1	47	74	Faure et al. (2010)
-109.67	70.704	1	256	286	Faure et al. (2010)
-109.644	70.694	1	256	286	Faure et al. (2010)
-109.635	64.454	1	47	74	Faure et al. (2010)
-109.629	64.45	1	47	74	Faure et al. (2010)
-109.624	70.687	1	256	286	Faure et al. (2010)
-109.617	64.432	1	47	74	Faure et al. (2010)
-109.609	64.436	1	47	74	Faure et al. (2010)
-109.546	64.459	1	47	74	Faure et al. (2010)
-109.495	64.537	1	47	74	Faure et al. (2010)
-109.487	64.536	1	47	74	Faure et al. (2010)
-109.468	64.458	1	47	74	Faure et al. (2010)
-109.449	64.435	1	47	74	Faure et al. (2010)
-109.448	64.328	1	47	74	Faure et al. (2010)
-109.389	64.325	1	47	74	Faure et al. (2010)
-109.372	64.325	1	47	74	Faure et al. (2010)
-109.361	64.328	1	47	74	Faure et al. (2010)
-109.355	64.431	1	47	74	Faure et al. (2010)
-109.347	63.37	1	485	541	Faure et al. (2010)
-109.293	64.443	1	47	74	Faure et al. (2010)
-109.241	64.43	1	47	74	Faure et al. (2010)
-109.239	70.233	1	256	286	Faure et al. (2010)
-109.215	63.433	1	550	550	Faure et al. (2010)
-91.363	63.081	1	170	228	Faure et al. (2010)
-109.208	63.435	1	542.2	542.2	Faure et al. (2010)
-109.212	63.445	1	550	550	Faure et al. (2010)
-109.146	70.199	1	254	273.8	Faure et al. (2010)
-109.133	64.634	1	47	74	Faure et al. (2010)
-109.123	70.194	1	256	290	Faure et al. (2010)
-109.108	70.197	1	256	286	Faure et al. (2010)
-109.106	70.188	1	256	286	Faure et al. (2010)
-109.084	64.584	1	47	74	Faure et al. (2010)
-91.668	63.165	1	170	228	Faure et al. (2010)
-108.892	63.495	1	485.4	541	Faure et al. (2010)
-109.021	70.185	1	253	286	Faure et al. (2010)
-108.991	70.153	1	256	286	Faure et al. (2010)
-108.809	64.669	1	47	74	Faure et al. (2010)

-105.196	53.43	1	91	97	Faure et al. (2010)
-105.196	53.418	1	98	101	Faure et al. (2010)
-105.193	53.425	1	98	101	Faure et al. (2010)
-105.192	53.403	1	98	101	Faure et al. (2010)
-105.08	53.476	1	98	101	Faure et al. (2010)
-105.07	53.574	1	98	101	Faure et al. (2010)
-105.064	53.465	1	98	101	Faure et al. (2010)
-105.058	53.474	1	98	101	Faure et al. (2010)
-104.969	53.436	1	98	101	Faure et al. (2010)
-104.964	53.489	1	98	101	Faure et al. (2010)
-104.959	53.476	1	98	101	Faure et al. (2010)
-104.955	53.444	1	98	101	Faure et al. (2010)
-104.934	53.362	1	98	101	Faure et al. (2010)
-104.93	53.4	1	98	101	Faure et al. (2010)
-104.918	53.393	1	98	101	Faure et al. (2010)
-104.91	53.408	1	98	101	Faure et al. (2010)
-104.905	53.409	1	98	101	Faure et al. (2010)
-104.905	53.272	1	98	101	Faure et al. (2010)
-104.909	53.44	1	98	101	Faure et al. (2010)
-104.902	53.401	1	98	101	Faure et al. (2010)
-104.9	53.365	1	98	101	Faure et al. (2010)
-104.897	53.296	1	98	101	Faure et al. (2010)
-104.891	53.29	1	98	101	Faure et al. (2010)
-104.89	53.305	1	98	101	Faure et al. (2010)
-104.891	53.285	1	98	101	Faure et al. (2010)
-104.881	53.351	1	98	101	Faure et al. (2010)
-104.875	53.276	1	98	101	Faure et al. (2010)
-104.876	53.39	1	98	101	Faure et al. (2010)
-104.872	53.374	1	98	101	Faure et al. (2010)
-104.87	53.38	1	98	101	Faure et al. (2010)
-104.865	53.306	1	98	101	Faure et al. (2010)
-104.87	53.396	1	98	101	Faure et al. (2010)
-104.87	53.267	1	98	101	Faure et al. (2010)
-104.859	53.303	1	98	101	Faure et al. (2010)
-104.858	53.336	1	98	101	Faure et al. (2010)
-104.858	53.341	1	98	101	Faure et al. (2010)
-104.857	53.346	1	98	101	Faure et al. (2010)
-104.854	53.703	1	98	101	Faure et al. (2010)
-104.852	53.986	1	98	101	Faure et al. (2010)
-104.864	53.259	1	98	101	Faure et al. (2010)
-104.841	53.976	1	98	101	Faure et al. (2010)
-104.842	53.331	1	98	101	Faure et al. (2010)
-104.839	53.296	1	98	101	Faure et al. (2010)

-104.835	53.308	1	98	101	Faure et al. (2010)
-104.83	53.206	1	98	101	Faure et al. (2010)
-104.82	53.293	1	98	101	Faure et al. (2010)
-104.826	53.341	1	98	101	Faure et al. (2010)
-104.818	53.284	1	98	101	Faure et al. (2010)
-104.817	53.245	1	98	101	Faure et al. (2010)
-104.815	53.238	1	98	101	Faure et al. (2010)
-104.81	53.269	1	98	101	Faure et al. (2010)
-104.808	53.292	1	98	101	Faure et al. (2010)
-104.81	53.278	1	98	101	Faure et al. (2010)
-104.803	53.262	1	98	101	Faure et al. (2010)
-104.801	53.237	1	98	101	Faure et al. (2010)
-104.798	53.259	1	98	101	Faure et al. (2010)
-104.798	53.36	1	98	101	Faure et al. (2010)
-104.79	53.258	1	91	97	Faure et al. (2010)
-104.789	53.23	1	91	97	Faure et al. (2010)
-104.79	53.289	1	91	97	Faure et al. (2010)
-104.788	53.251	1	91	97	Faure et al. (2010)
-104.785	53.285	1	91	97	Faure et al. (2010)
-104.784	53.274	1	91	97	Faure et al. (2010)
-104.777	53.265	1	91	97	Faure et al. (2010)
-104.774	53.224	1	102	105	Faure et al. (2010)
-104.766	53.576	1	91	97	Faure et al. (2010)
-104.748	53.231	1	91	97	Faure et al. (2010)
-104.677	53.511	1	91	97	Faure et al. (2010)
-104.676	53.508	1	91	97	Faure et al. (2010)
-104.669	53.511	1	91	97	Faure et al. (2010)
-104.662	53.507	1	91	97	Faure et al. (2010)
-104.653	53.5	1	91	97	Faure et al. (2010)
-104.632	53.491	1	91	97	Faure et al. (2010)
-104.625	53.484	1	91	97	Faure et al. (2010)
-104.623	53.474	1	91	97	Faure et al. (2010)
-104.609	53.471	1	91	97	Faure et al. (2010)
-104.608	53.482	1	91	97	Faure et al. (2010)
-104.601	53.479	1	91	97	Faure et al. (2010)
-94.091	73.118	1	94	103	Faure et al. (2010)
-94.083	72.833	1	94	98	Faure et al. (2010)
-94.031	73.134	1	94	98	Faure et al. (2010)
-93.9	72.86	1	94	98	Faure et al. (2010)
-93.288	73.503	1	94	103	Faure et al. (2010)
-92.927	73.334	1	94	98	Faure et al. (2010)
-92.572	73.315	1	94	103	Faure et al. (2010)
-92.556	73.467	1	94	103	Faure et al. (2010)

-92.379	73.369	1	94	98	Faure et al. (2010)
-92.315	73.472	1	94	98	Faure et al. (2010)
-92.168	73.575	1	94	103	Faure et al. (2010)
-91.987	73.285	1	94	103	Faure et al. (2010)
-91.984	73.303	1	94	103	Faure et al. (2010)
-91.967	73.291	1	94	103	Faure et al. (2010)
-91.884	63.183	1	170	228	Faure et al. (2010)
-91.914	73.304	1	94	103	Faure et al. (2010)
-91.905	73.294	1	94	103	Faure et al. (2010)
-91.878	73.308	1	94	103	Faure et al. (2010)
-91.877	73.301	1	94	103	Faure et al. (2010)
-91.875	73.303	1	94	103	Faure et al. (2010)
-91.116	63.18	1	170	228	Faure et al. (2010)
-91.854	73.303	1	94	103	Faure et al. (2010)
-91.014	63.141	1	170	228	Faure et al. (2010)
-91.349	62.948	1	170	228	Faure et al. (2010)
-91.363	62.998	1	170	228	Faure et al. (2010)
-91.349	62.954	1	170	228	Faure et al. (2010)
-91.347	62.941	1	170	228	Faure et al. (2010)
-91.315	62.918	1	170	228	Faure et al. (2010)
-91.305	63.003	1	170	228	Faure et al. (2010)
-91.14	63.024	1	170	228	Faure et al. (2010)
-91.06	63.006	1	170	228	Faure et al. (2010)
-90.931	63.072	1	170	228	Faure et al. (2010)
-90.965	73.475	1	94	103	Faure et al. (2010)
-90.957	73.52	1	94	98	Faure et al. (2010)
-90.905	63.068	1	170	228	Faure et al. (2010)
-90.88	63.192	1	170	228	Faure et al. (2010)
-90.844	63.084	1	170	2228	Faure et al. (2010)
-90.86	63.057	1	214	214	Faure et al. (2010)
-90.806	63.226	1	170	228	Faure et al. (2010)
-90.748	63.036	1	170	228	Faure et al. (2010)
-88.28	73.244	1	419.2	443.4	Faure et al. (2010)
-88.275	73.245	1	419.2	443.4	Faure et al. (2010)
-88.27	73.246	1	419.2	443.4	Faure et al. (2010)
-88.14	73.334	1	419.2	443.4	Faure et al. (2010)
-88.134	73.308	1	419.2	443.4	Faure et al. (2010)
-88.134	73.268	1	419.2	443.4	Faure et al. (2010)
-88.084	73.323	1	419.2	443.4	Faure et al. (2010)
-87.234	48.838	1	1800	1800	Faure et al. (2010)
-87.494	73.087	1	419.2	419.2	Faure et al. (2010)
-86.722	48.805	8	1800	1800	Faure et al. (2010)
-87.023	48.643	1	400	400	Faure et al. (2010)

-86.643	48.744	1	1800	1800	Faure et al. (2010)
-85.355	52.426	1	1060	1140	Faure et al. (2010)
-84.749	47.958	5	2680	2740	Faure et al. (2010)
-84.353	48.084	1	1090	1104	Faure et al. (2010)
-84.344	48.085	1	1090	1104	Faure et al. (2010)
-84.273	48.317	5	2680	2740	Faure et al. (2010)
-84.186	48.17	5	2680	2740	Faure et al. (2010)
-84.122	48.17	5	2680	2740	Faure et al. (2010)
-84.118	48.165	5	2680	2740	Faure et al. (2010)
-83.998	48.342	5	2680	2740	Faure et al. (2010)
-83.987	48.183	5	2680	2740	Faure et al. (2010)
-83.913	52.836	1	136	192	Faure et al. (2010)
-83.905	52.834	1	136	193	Faure et al. (2010)
-83.897	52.846	1	174.8	179.2	Faure et al. (2010)
-83.893	52.844	1	256	256	Faure et al. (2010)
-83.887	52.826	1	179	179	Faure et al. (2010)
-83.885	52.832	1	176	176	Faure et al. (2010)
-83.878	52.827	1	180	180	Faure et al. (2010)
-83.85	52.842	1	136	194	Faure et al. (2010)
-83.841	52.79	1	170	170	Faure et al. (2010)
-83.838	52.793	1	170	170	Faure et al. (2010)
-83.81	52.778	1	136	195	Faure et al. (2010)
-83.861	69.164	1	600	600	Faure et al. (2010)
-83.802	52.76	1	136	196	Faure et al. (2010)
-83.788	52.764	1	136	197	Faure et al. (2010)
-83.822	52.741	1	136	198	Faure et al. (2010)
-83.768	52.89	1	136	203	Faure et al. (2010)
-83.755	52.613	1	136	199	Faure et al. (2010)
-83.782	52.697	1	136	191	Faure et al. (2010)
-83.724	52.66	1	136	200	Faure et al. (2010)
-83.721	52.666	1	136	201	Faure et al. (2010)
-83.684	69.173	1	600	600	Faure et al. (2010)
-83.595	52.761	1	136	202	Faure et al. (2010)
-83.611	52.76	1	136	204	Faure et al. (2010)
-83.475	69.094	1	600	600	Faure et al. (2010)
-83.44	69.204	1	600	600	Faure et al. (2010)
-83.316	69.172	1	600	600	Faure et al. (2010)
-83.096	69.13	1	600	600	Faure et al. (2010)
-82.867	69.06	1	600	600	Faure et al. (2010)
-82.643	68.964	1	600	600	Faure et al. (2010)
-80.195	48.463	1	154	154	Faure et al. (2010)
-80.218	48.473	1	165	165	Faure et al. (2010)
-80.185	48.483	1	149.3	154.9	Faure et al. (2010)

-79.951	48.477	1	153	153	Faure et al. (2010)
-79.951	48.477	1	146	146	Faure et al. (2010)
-79.914	48.282	1	155.5	155.5	Faure et al. (2010)
-79.909	48.215	1	155.6	155.6	Faure et al. (2010)
-79.884	48.236	1	158.1	159.9	Faure et al. (2010)
-79.88	48.22	1	156.9	156.9	Faure et al. (2010)
-79.877	48.251	1	158.9	158.9	Faure et al. (2010)
-79.835	48.142	1	155.3	155.3	Faure et al. (2010)
-79.801	48.282	1	155.4	156.6	Faure et al. (2010)
-79.801	47.473	1	134	134	Faure et al. (2010)
-79.772	47.452	1	153.7	153.7	Faure et al. (2010)
-79.751	48.116	1	150.4	154.8	Faure et al. (2010)
-79.756	48.124	1	150.4	154.8	Faure et al. (2010)
-79.759	47.49	1	142	142	Faure et al. (2010)
-79.745	47.452	1	136.2	141.4	Faure et al. (2010)
-79.717	47.479	1	155	155	Faure et al. (2010)
-79.707	47.471	1	152	152	Faure et al. (2010)
-79.678	47.437	1	154	154	Faure et al. (2010)
-79.505	47.641	1	124	126	Faure et al. (2010)
-79.372	47.569	1	136	142	Faure et al. (2010)
-78.405	53.028	1	600	658	Faure et al. (2010)
-76.585	49.684	1	1074	1122	Faure et al. (2010)
-76.144	49.442	1	1087	1121	Faure et al. (2010)
-76.133	49.502	1	1100	1100	Faure et al. (2010)
-73.91	45.504	6	126	126	Faure et al. (2010)
-72.384	51.992	1	547.4	554.4	Faure et al. (2010)
-72.234	52.82	1	492	552	Faure et al. (2010)
-72.197	52.822	7	631	631	Faure et al. (2010)
-72.189	52.811	1	638.5	642.5	Faure et al. (2010)
-65.145	59.473	1	580.4	587.6	Faure et al. (2010)
-65.126	59.469	1	535	565	Faure et al. (2010)
-64.69	59.368	1	580	580	Faure et al. (2010)
-62.7	58.56	1	1143	1375	Faure et al. (2010)
-62.635	58.352	1	1243	1275	Faure et al. (2010)
-59.211	55.019	1	145	197	Faure et al. (2010)
-123.747	56.45	3	322	341	Faure et al. (2010)
-76.143	49.433	1	1075	1167	Faure et al. (2010)
-109.32	47.654	1	47	52	Faure et al. (2010)
-109.315	47.796	1	47	52	Faure et al. (2010)
-109.289	47.785	1	47	52	Faure et al. (2010)
-109.279	47.826	1	47	52	Faure et al. (2010)
-109.241	47.8	1	47	52	Faure et al. (2010)
-109.213	47.544	1	47	52	Faure et al. (2010)

-109.205	47.8	1	47	52	Faure et al. (2010)
-109.164	47.789	1	47	52	Faure et al. (2010)
-109.106	47.776	1	47	52	Faure et al. (2010)
-109.082	47.821	1	47	52	Faure et al. (2010)
-109.06	47.779	1	47	52	Faure et al. (2010)
-109.011	47.648	1	47	52	Faure et al. (2010)
-109.003	47.852	1	47	52	Faure et al. (2010)
-108.991	47.878	1	47	52	Faure et al. (2010)
-108.952	47.799	1	47	52	Faure et al. (2010)
-108.952	47.855	1	47	52	Faure et al. (2010)
-108.948	47.898	1	47	52	Faure et al. (2010)
-108.906	47.861	1	47	52	Faure et al. (2010)
-108.865	47.831	1	47	52	Faure et al. (2010)
-108.852	47.865	1	47	52	Faure et al. (2010)
-108.729	47.816	1	47	52	Faure et al. (2010)
-108.725	47.132	2	50	50	Faure et al. (2010)
-108.699	47.847	1	46	51	Faure et al. (2010)
-108.697	47.848	1	45.5	50.5	Faure et al. (2010)
-108.442	47.841	1	47	52	Faure et al. (2010)
-108.394	47.846	1	47	52	Faure et al. (2010)
-107.279	46.413	2	50	50	Faure et al. (2010)
-107.092	47.303	2	27	27	Faure et al. (2010)
-107.043	46.581	2	50	50	Faure et al. (2010)
-106.903	46.663	2	50	50	Faure et al. (2010)
-105.613	40.393	1	377	395	Faure et al. (2010)
-105.562	40.857	1	600	600	Faure et al. (2010)
-105.453	40.982	1	377	395	Faure et al. (2010)
-105.45	40.985	1	377	395	Faure et al. (2010)
-105.449	40.978	1	377	395	Faure et al. (2010)
-105.444	40.986	1	377	395	Faure et al. (2010)
-105.442	40.889	1	614.5	614.5	Faure et al. (2010)
-105.439	40.89	1	614.5	614.5	Faure et al. (2010)
-105.436	40.891	1	612.4	616.6	Faure et al. (2010)
-105.429	40.996	1	377	395	Faure et al. (2010)
-105.43	40.995	1	377	395	Faure et al. (2010)
-105.428	40.998	1	377	395	Faure et al. (2010)
-105.425	40.998	1	377	395	Faure et al. (2010)
-105.423	40.998	1	377	395	Faure et al. (2010)
-105.421	40.998	1	377	395	Faure et al. (2010)
-105.419	40.999	1	377	395	Faure et al. (2010)
-105.417	40.999	1	377	395	Faure et al. (2010)
-105.414	40.996	1	377	395	Faure et al. (2010)
-105.415	40.997	1	377	395	Faure et al. (2010)

-105.411	40.995	1	377	395	Faure et al. (2010)
-105.405	40.996	1	377	395	Faure et al. (2010)
-105.404	40.994	1	377	395	Faure et al. (2010)
-105.402	41.03	1	354	500	Faure et al. (2010)
-105.401	41.03	1	377	395	Faure et al. (2010)
-105.389	41.003	1	377	395	Faure et al. (2010)
-105.387	41.002	1	377	395	Faure et al. (2010)
-105.386	41.002	1	354	500	Faure et al. (2010)
-105.386	40.869	1	354	409	Faure et al. (2010)
-105.385	41.008	1	377	395	Faure et al. (2010)
-105.384	41.027	1	354	500	Faure et al. (2010)
-105.382	41.006	1	377	395	Faure et al. (2010)
-105.382	41.028	1	354	500	Faure et al. (2010)
-105.378	41.004	1	377	395	Faure et al. (2010)
-105.376	41.002	1	377	395	Faure et al. (2010)
-105.373	41	1	377	395	Faure et al. (2010)
-105.371	40.872	1	354	409	Faure et al. (2010)
-105.368	40.869	1	354	500	Faure et al. (2010)
-105.35	40.935	1	377	395	Faure et al. (2010)
-105.349	40.932	1	354	500	Faure et al. (2010)
-105.349	40.88	1	354	409	Faure et al. (2010)
-105.345	40.933	1	377	395	Faure et al. (2010)
-105.316	40.974	1	377	395	Faure et al. (2010)
-105.316	40.013	1	523	780	Faure et al. (2010)
-96.723	39.43	1	100	108	Faure et al. (2010)
-93.675	34.033	2	140	140	Faure et al. (2010)
-93.665	34.036	2	87	101	Faure et al. (2010)
-93.663	34.038	2	87	101	Faure et al. (2010)
-93.653	34.043	2	87	101	Faure et al. (2010)
-93.652	34.049	2	95	100	Faure et al. (2010)
-93.652	34.049	2	95	100	Faure et al. (2010)
-93.65	34.046	2	87	101	Faure et al. (2010)
-93.648	34.047	2	87	101	Faure et al. (2010)
-88.177	46.175	1	144	550	Faure et al. (2010)
-82.996	38.126	1	87	91	Faure et al. (2010)
-82.981	38.128	1	87	91	Faure et al. (2010)
-79.917	39.893	1	144	195	Faure et al. (2010)
-79.844	37.771	1	458.4	470	Faure et al. (2010)
-79.045	40.708	1	84	94	Faure et al. (2010)
-76.535	42.455	1	146	146	Faure et al. (2010)
-105.146	41.564	1	400	410.6	Faure et al. (2010)
-105.161	41.591	1	380	380	Faure et al. (2010)
-109.348	41.649	2	3	3	Faure et al. (2010)

-108.954	41.821	2	0.96	0.96	Faure et al. (2010)
-108.96	41.84	2	0.92	0.92	Faure et al. (2010)
-109.182	41.979	2	2.19	2.19	Faure et al. (2010)
-108.943	41.981	2	1.77	1.77	Faure et al. (2010)
-108.789	41.879	2	0.8	0.8	Faure et al. (2010)
-108.871	41.861	2	0.89	0.89	Faure et al. (2010)
-109	41.919	2	0.9	3	Faure et al. (2010)
-109.032	41.841	2	0.96	0.96	Faure et al. (2010)
-83.31	69.172	1	600	600	Faure et al. (2010)
-93.759	34.937	2	106	106	Faure et al. (2010)
-95.262	63.882	5	1832	1832	Faure et al. (2010)
-83.698	52.661	1	136	196	Faure et al. (2010)
-91.665	63.348	1	170	228	Faure et al. (2010)
-91.037	63.219	1	170	228	Faure et al. (2010)
-90.983	63.186	1	170	228	Faure et al. (2010)
-90.98	63.185	1	170	228	Faure et al. (2010)
-91.17	63.179	1	170	228	Faure et al. (2010)
-91.166	63.159	1	170	228	Faure et al. (2010)
-91.077	63.174	1	170	228	Faure et al. (2010)
-91.478	63.045	1	170	228	Faure et al. (2010)
-91.442	63.01	1	170	228	Faure et al. (2010)
-91.425	63.004	1	170	228	Faure et al. (2010)
-91.34	63.049	1	170	228	Faure et al. (2010)
-91.021	63.128	1	170	228	Faure et al. (2010)
-91.008	63.137	1	170	228	Faure et al. (2010)
-91.025	63.142	1	170	228	Faure et al. (2010)
-90.995	63.15	1	170	228	Faure et al. (2010)
-90.969	63.148	1	170	228	Faure et al. (2010)
-90.934	63.147	1	170	228	Faure et al. (2010)
-91.224	63.128	1	170	228	Faure et al. (2010)
-91.419	63.051	1	170	228	Faure et al. (2010)
-113.008	57.396	1	86	93	Faure et al. (2010)
-91.074	63.352	1	170	228	Faure et al. (2010)
-91.364	63.26	1	170	228	Faure et al. (2010)
-90.822	63.054	1	170	228	Faure et al. (2010)
-90.881	63.053	1	170	228	Faure et al. (2010)
-90.862	63.068	1	170	228	Faure et al. (2010)
-91.227	63.042	1	170	228	Faure et al. (2010)
-91.265	62.967	1	170	228	Faure et al. (2010)
-91.301	62.973	1	170	228	Faure et al. (2010)
-91.312	62.988	1	170	228	Faure et al. (2010)
-91.402	62.929	1	170	228	Faure et al. (2010)
-91.729	63.159	1	170	228	Faure et al. (2010)

-91.683	63.18	1	170	228	Faure et al. (2010)
-91.307	63.122	1	170	228	Faure et al. (2010)
-91.162	63.119	1	170	228	Faure et al. (2010)
-91.172	63.134	1	170	228	Faure et al. (2010)
-91.208	63.118	1	170	228	Faure et al. (2010)
-91.379	63.061	1	170	228	Faure et al. (2010)
-91.371	63.068	1	170	228	Faure et al. (2010)
-114.909	56.86	1	86	96	Faure et al. (2010)
-91.201	63.142	1	170	228	Faure et al. (2010)
-90.931	68.281	1	540	540	Faure et al. (2010)
-114.913	56.862	1	86	96	Faure et al. (2010)
-83.95	52.8803	1	175.9	178.5	Heaman and Kjarsgaard (2000)
-83.93333	52.8595	1	178.3	181.5	Heaman and Kjarsgaard (2000)
-83.9419	52.86515	1	177.2	181.6	Heaman and Kjarsgaard (2000)
-83.9419	52.86515	1	173.9	177.5	Heaman and Kjarsgaard (2000)
-79.87783	48.25336	1	155.2	162.6	Heaman and Kjarsgaard (2000)
-79.88068	48.22144	1	154.4	159.4	Heaman and Kjarsgaard (2000)
-79.88392	48.23677	1	155.1	156.9	Heaman and Kjarsgaard (2000)
-79.80105	48.28182	1	155.4	156.6	Heaman and Kjarsgaard (2000)
-79.91759	48.28433	1	153.4	157.6	Heaman and Kjarsgaard (2000)
-79.71725	47.47855	1	153.9	156.9	Heaman and Kjarsgaard (2000)
-79.70608	47.47415	1	149.6	154	Heaman and Kjarsgaard (2000)
-80.18266	48.48354	1	149.3	154.9	Heaman and Kjarsgaard (2000)
-80.19516	48.46321	1	152.2	154.8	Heaman and Kjarsgaard (2000)
-80.19	48.44	1	162	167.4	Heaman and Kjarsgaard (2000)
-79.75913	48.12033	1	150.4	154.8	Heaman and Kjarsgaard (2000)
-79.84407	48.13741	1	154	156.6	Heaman and Kjarsgaard (2000)
-79.92929	48.20841	1	153.6	157.6	Heaman and Kjarsgaard (2000)
-79.74492	47.45929	1	136.2	141.4	Heaman and Kjarsgaard (2000)

-79.95118	48.47708	1	150.8	156	Heaman and Kjarsgaard (2000)
-79.95118	48.47708	1	142.9	148.9	Heaman and Kjarsgaard (2000)
-79.76611	47.55021	1	151.9	155.5	Heaman and Kjarsgaard (2000)
-79.79247	47.46822	1	132.4	135.4	Heaman and Kjarsgaard (2000)
-79.68166	47.44247	1	151.2	156	Heaman and Kjarsgaard (2000)
-79.75855	47.48981	1	139.1	144.7	Heaman and Kjarsgaard (2000)
-81.7575	50.43694	4	151.2	152.4	Heaman and Kjarsgaard (2000)
-81.9	50.33333	3	233.4	237.8	Heaman and Kjarsgaard (2000)
-76.82639	44.40556	3	173.7	177.7	Heaman and Kjarsgaard (2000)
-79.3669	47.57212	1	135.7	148.9	Heaman and Kjarsgaard (2000)
-76.54889	42.49444	3	144.5	150.5	Heaman and Kjarsgaard (2000)
-76.53167	42.45833	1	144.1	147.9	Heaman and Kjarsgaard (2000)
-76.621524	42.530088	1	110	130	Bailey and Lupulescu (2015)
-76.525449	42.457201	1	143	149	Bailey and Lupulescu (2015)
-76.3434	42.934657	1	110	130	Bailey and Lupulescu (2015)
-76.13761	43.055924	1	110	130	Bailey and Lupulescu (2015)
-76.080749	43.04928	1	110	130	Bailey and Lupulescu (2015)
-74.741392	43.019719	1	145	150	Bailey and Lupulescu (2015)
-108.58918	47.006483	1	18	215	Carlson et al. (2004)
-108.58918	47.8511	1	49	2463	Carlson et al. (2004)
-68.76704	56.41953	1	n/a	1880	Tappe et al. (2018)
-68.81321	56.48383	1	n/a	1873	Tappe et al. (2018)
-82.52083	49.44104	1	n/a	1842	Tappe et al. (2018)
-105.4533	40.8433	1	n/a	1350	Tappe et al. (2018)
-85.4041	52.46339	1	n/a	1123	Tappe et al. (2018)
-86.67367	48.83751	1	n/a	1085	Tappe et al. (2018)
-85.257604	53.07604	1	n/a	1076.2	Tappe et al. (2018)
-76.141	49.42466	1	n/a	1000	Tappe et al. (2018)
-81.7351	46.6422	1	n/a	975	Tappe et al. (2018)
-88.163	46.0494	1	n/a	793	Tappe et al. (2018)
-78.5633	52.90068	1	n/a	790	Tappe et al. (2018)
-80.215843	70.696097	1	n/a	672.7	Tappe et al. (2018)
-80.063409	70.501524	1	n/a	655	Tappe et al. (2018)
-109.3461	63.3697	1	n/a	650	Tappe et al. (2018)

-72.197522	52.822961	1	n/a	631.6	Tappe et al. (2018)
-105.5344	40.8664	1	n/a	614.5	Tappe et al. (2018)
-112.993941	66.557162	1	n/a	613	Tappe et al. (2018)
-105.7014	40.8908	1	n/a	600	Tappe et al. (2018)
-109.70854	64.70535	1	n/a	590	Tappe et al. (2018)
-65.11748	59.47747	1	n/a	584	Tappe et al. (2018)
-113.36772	63.46607	1	n/a	574	Tappe et al. (2018)
-59.1698	55.22023	1	n/a	570	Tappe et al. (2018)
-71.24841	48.46632	1	n/a	568	Tappe et al. (2018)
-72.39706	51.97688	1	n/a	550.9	Tappe et al. (2018)
-65.13667	59.465	1	n/a	550	Tappe et al. (2018)
-65.18417	59.44375	1	n/a	550	Tappe et al. (2018)
-109.22687	63.43061	1	n/a	549	Tappe et al. (2018)
-86.139937	66.560385	1	n/a	546	Tappe et al. (2018)
-109.19962	63.44174	1	n/a	542	Tappe et al. (2018)
-109.2082	63.43537	1	n/a	539	Tappe et al. (2018)
-113.21469	67.13947	1	n/a	535	Tappe et al. (2018)
-84.279334	72.229496	1	n/a	535	Tappe et al. (2018)
-109.2122	63.4454	1	n/a	531	Tappe et al. (2018)
-83.390028	69.283497	1	n/a	530	Tappe et al. (2018)
-83.299431	69.269235	1	n/a	530	Tappe et al. (2018)
-110.8565	63.608118	1	n/a	523	Tappe et al. (2018)
-72.231282	52.819206	1	n/a	522	Tappe et al. (2018)
-113.66028	64.20248	1	n/a	500	Tappe et al. (2018)
-113.60254	64.2194	1	n/a	480	Tappe et al. (2018)
-110.15822	63.570439	1	n/a	470	Tappe et al. (2018)
-113.152883	67.01286	1	n/a	467	Tappe et al. (2018)
-113.69101	63.70822	1	n/a	461	Tappe et al. (2018)
-113.29473	63.55704	1	n/a	450.4	Tappe et al. (2018)
-113.73111	63.69148	1	n/a	448	Tappe et al. (2018)
-113.80564	62.13837	1	n/a	441.4	Tappe et al. (2018)
-129.50134	64.23105	1	n/a	437	Tappe et al. (2018)
-113.29149	63.51669	1	n/a	435.4	Tappe et al. (2018)
-105.5186	40.3289	1	n/a	404	Tappe et al. (2018)
-90.2014	37.7439	1	n/a	397	Tappe et al. (2018)
-116.96274	51.70222	1	n/a	391	Tappe et al. (2018)
-90.3153	37.8178	1	n/a	388	Tappe et al. (2018)
-90.1981	37.7347	1	n/a	385	Tappe et al. (2018)
-105.47	41.0056	1	n/a	377	Tappe et al. (2018)
-123.75083	56.41852	1	n/a	334	Tappe et al. (2018)
-105.2067	41.6497	1	n/a	326	Tappe et al. (2018)
-110.1415	70.541995	1	n/a	300	Tappe et al. (2018)
-88.3667	37.5344	1	n/a	288	Tappe et al. (2018)

-109.123889	70.193355	1	n/a	286	Tappe et al. (2018)
-82.9833	38.1	1	n/a	286	Tappe et al. (2018)
-109.108501	70.188941	1	n/a	276	Tappe et al. (2018)
-83	38.1167	1	n/a	270	Tappe et al. (2018)
-109.145304	70.198493	1	n/a	257	Tappe et al. (2018)
-109.02131	70.184736	1	n/a	256	Tappe et al. (2018)
-88.3333	37.4417	1	n/a	252	Tappe et al. (2018)
-109.853599	70.728122	1	n/a	251	Tappe et al. (2018)
-109.921304	70.766087	1	n/a	247	Tappe et al. (2018)
-114.99736	50.08749	1	n/a	241	Tappe et al. (2018)
-81.91783	50.32182	1	n/a	235.6	Tappe et al. (2018)
-91.117596	63.174743	1	n/a	227	Tappe et al. (2018)
-91.01	63.13	1	n/a	224	Tappe et al. (2018)
-90.978073	63.181524	1	n/a	222	Tappe et al. (2018)
-91.403857	62.879697	1	n/a	214	Tappe et al. (2018)
-91.3	62.91	1	n/a	204	Tappe et al. (2018)
-91.34	62.94	1	n/a	199	Tappe et al. (2018)
-91.34	62.94	1	n/a	198	Tappe et al. (2018)
-90.836315	63.337216	1	n/a	197	Tappe et al. (2018)
-91.922993	62.972727	1	n/a	196.2	Tappe et al. (2018)
-90.85	63.06	1	n/a	195	Tappe et al. (2018)
-90.88	63.19	1	n/a	191	Tappe et al. (2018)
-90.99	63.14	1	n/a	191	Tappe et al. (2018)
-91.012719	63.13459	1	n/a	189	Tappe et al. (2018)
-88.1035	46.1031	1	n/a	186	Tappe et al. (2018)
-90.74	63.03	1	n/a	185	Tappe et al. (2018)
-91.35	62.99	1	n/a	184	Tappe et al. (2018)
-91.72	63.15	1	n/a	183	Tappe et al. (2018)
-91.015006	63.134942	1	n/a	183	Tappe et al. (2018)
-91.35	62.99	1	n/a	181	Tappe et al. (2018)
-83.913601	52.879115	1	n/a	180	Tappe et al. (2018)
-83.933389	52.85872	1	n/a	179.9	Tappe et al. (2018)
-83.95413	52.88295	1	n/a	177.2	Tappe et al. (2018)
-111.78325	65.95674	1	n/a	177	Tappe et al. (2018)
-76.8274	44.40542	1	n/a	176	Tappe et al. (2018)
-83.93949	52.864978	1	n/a	175.7	Tappe et al. (2018)
-111.945724	66.115167	1	n/a	175	Tappe et al. (2018)
-111.875058	66.062685	1	n/a	174	Tappe et al. (2018)
-91.35	62.94	1	n/a	173	Tappe et al. (2018)
-77.12634	44.04897	1	n/a	173	Tappe et al. (2018)
-111.478682	65.995845	1	n/a	172	Tappe et al. (2018)
-91.029555	63.210672	1	n/a	171	Tappe et al. (2018)
-112.33272	66.1588	1	n/a	170	Tappe et al. (2018)

-111.94295	65.97477	1	n/a	169	Tappe et al. (2018)
-65.107733	59.362	1	n/a	164.7	Tappe et al. (2018)
-79.88704	48.21613	1	n/a	159	Tappe et al. (2018)
-79.93399	48.14807	1	n/a	158	Tappe et al. (2018)
-83.883106	52.820813	1	n/a	158	Tappe et al. (2018)
-110.56114	64.46717	1	n/a	156.9	Tappe et al. (2018)
-66.56490311	64.49408198	1	n/a	156.7	Tappe et al. (2018)
-79.87783	48.25336	1	n/a	156	Tappe et al. (2018)
-79.88147	48.22049	1	n/a	156	Tappe et al. (2018)
-66.30810511	64.22240612	1	n/a	156	Tappe et al. (2018)
-79.80198	48.27919	1	n/a	156	Tappe et al. (2018)
-83.825125	52.91698	1	n/a	156	Tappe et al. (2018)
-79.92503	48.28375	1	n/a	156	Tappe et al. (2018)
-65.95924999	64.27447537	1	n/a	155.9	Tappe et al. (2018)
-79.91554	48.20754	1	n/a	155.6	Tappe et al. (2018)
-79.72031	47.47854	1	n/a	155.4	Tappe et al. (2018)
-79.89163	47.52334	1	n/a	155.3	Tappe et al. (2018)
-79.8817	48.23437	1	n/a	155	Tappe et al. (2018)
-76.5183	42.5333	1	n/a	155	Tappe et al. (2018)
-74.733333	43.018889	1	n/a	154	Tappe et al. (2018)
-79.76648	47.45513	1	n/a	153.7	Tappe et al. (2018)
-79.68363	47.44286	1	n/a	153.6	Tappe et al. (2018)
-66.24803326	64.23728329	1	n/a	152.8	Tappe et al. (2018)
-79.75788	48.11649	1	n/a	152.6	Tappe et al. (2018)
-66.26522194	64.1261961	1	n/a	152.1	Tappe et al. (2018)
-80.19558	48.46821	1	n/a	152.1	Tappe et al. (2018)
-79.7065	47.47447	1	n/a	152	Tappe et al. (2018)
-66.1352725	64.32054223	1	n/a	151.8	Tappe et al. (2018)
-79.84004	48.14145	1	n/a	151	Tappe et al. (2018)
-66.02273893	64.20354985	1	n/a	150.6	Tappe et al. (2018)
-66.5227981	64.35414811	1	n/a	150.5	Tappe et al. (2018)
-66.11728167	64.25283914	1	n/a	150.4	Tappe et al. (2018)
-77	42.5	1	n/a	150	Tappe et al. (2018)
-79.9667	39.9667	1	n/a	150	Tappe et al. (2018)
-65.803753	64.70356	1	n/a	149.8	Tappe et al. (2018)
-66.556433	64.255239	1	n/a	149.5	Tappe et al. (2018)
-66.23362403	64.37799796	1	n/a	149.1	Tappe et al. (2018)

-65.794279	64.663498	1	n/a	148.1	Tappe et al. (2018)
-66.20357967	64.3159216	1	n/a	147.7	Tappe et al. (2018)
-66.3464395	64.2781534	1	n/a	147.5	Tappe et al. (2018)
-76.5467	42.4936	1	n/a	147.5	Tappe et al. (2018)
-66.0724563	64.32778671	1	n/a	147.3	Tappe et al. (2018)
-66.11756553	64.25757566	1	n/a	147.3	Tappe et al. (2018)
-66.35041074	64.23767532	1	n/a	146.4	Tappe et al. (2018)
-66.33409176	64.26499804	1	n/a	146.3	Tappe et al. (2018)
-76.4883	42.4442	1	n/a	146	Tappe et al. (2018)
-76.453	42.4102	1	n/a	146	Tappe et al. (2018)
-76.5239	42.4583	1	n/a	146	Tappe et al. (2018)
-79.95282	48.47693	1	n/a	145.9	Tappe et al. (2018)
-66.15980891	64.15095264	1	n/a	145.6	Tappe et al. (2018)
-66.52961576	64.32174635	1	n/a	145.4	Tappe et al. (2018)
-66.3537966	64.25053956	1	n/a	145.2	Tappe et al. (2018)
-66.35215478	64.24244303	1	n/a	144.8	Tappe et al. (2018)
-66.2180684	64.2269664	1	n/a	144.5	Tappe et al. (2018)
-66.1091478	64.220605	1	n/a	143.5	Tappe et al. (2018)
-66.1985567	64.17995241	1	n/a	143.4	Tappe et al. (2018)
-66.37887189	64.26284359	1	n/a	143.4	Tappe et al. (2018)
-66.3859479	64.2511326	1	n/a	143.4	Tappe et al. (2018)
-79.75855	47.48981	1	n/a	141.9	Tappe et al. (2018)
-66.2034038	64.1630481	1	n/a	141.4	Tappe et al. (2018)
-76.535	42.5522	1	n/a	141	Tappe et al. (2018)
-73.90896	45.50629	1	n/a	140	Tappe et al. (2018)
-76.6367	42.55	1	n/a	140	Tappe et al. (2018)
-66.1976127	64.1848614	1	n/a	139.1	Tappe et al. (2018)
-79.7419	47.46061	1	n/a	138.8	Tappe et al. (2018)
-66.20200642	64.18192498	1	n/a	138.4	Tappe et al. (2018)
-79.79	47.4674	1	n/a	133.9	Tappe et al. (2018)
-76.0733	42.9744	1	n/a	130	Tappe et al. (2018)
-77	42.5	1	n/a	128	Tappe et al. (2018)
-79.51606	47.64732	1	n/a	126.6	Tappe et al. (2018)
-79.36562	47.56768	1	n/a	126	Tappe et al. (2018)
-79.50955	47.64229	1	n/a	125	Tappe et al. (2018)
-76.3436	42.9344	1	n/a	125	Tappe et al. (2018)

-76.6133	42.5333	1	n/a	120	Tappe et al. (2018)
-96.9225	39.3052	1	n/a	115	Tappe et al. (2018)
-96.7244	39.3414	1	n/a	112	Tappe et al. (2018)
-93.96468	72.85241	1	n/a	105	Tappe et al. (2018)
-96.8614	39.3283	1	n/a	104	Tappe et al. (2018)
-104.77005	53.22399	1	n/a	103.9	Tappe et al. (2018)
-92.01266	73.35224	1	n/a	101	Tappe et al. (2018)
-104.81112	53.26886	1	n/a	101	Tappe et al. (2018)
-104.8224	53.28706	1	n/a	101	Tappe et al. (2018)
-104.87493	53.39014	1	n/a	101	Tappe et al. (2018)
-104.90493	53.40054	1	n/a	101	Tappe et al. (2018)
-90.980338	73.460655	1	n/a	100	Tappe et al. (2018)
-104.83153	53.20506	1	n/a	100	Tappe et al. (2018)
-104.80114	53.26003	1	n/a	100	Tappe et al. (2018)
-91.973372	73.349858	1	n/a	99	Tappe et al. (2018)
-92.017356	73.341768	1	n/a	99	Tappe et al. (2018)
-90.99275	73.511817	1	n/a	99	Tappe et al. (2018)
-92.183276	73.559657	1	n/a	99	Tappe et al. (2018)
-92.013086	73.352888	1	n/a	99	Tappe et al. (2018)
-104.79114	53.25611	1	n/a	99	Tappe et al. (2018)
-105.06926	53.57245	1	n/a	99	Tappe et al. (2018)
-91.9808	73.35273	1	n/a	98	Tappe et al. (2018)
-92.98438	73.32639	1	n/a	98	Tappe et al. (2018)
-104.78523	53.28576	1	n/a	98	Tappe et al. (2018)
-92.01693	73.34112	1	n/a	97	Tappe et al. (2018)
-90.99241	73.51116	1	n/a	96	Tappe et al. (2018)
-94.088638	73.129004	1	n/a	96	Tappe et al. (2018)
-104.81533	53.23745	1	n/a	96	Tappe et al. (2018)
-104.86559	53.26999	1	n/a	95	Tappe et al. (2018)
-104.83715	53.29605	1	n/a	95	Tappe et al. (2018)
-104.9117	53.40913	1	n/a	95	Tappe et al. (2018)
-96.8203	39.49	1	n/a	95	Tappe et al. (2018)
-94.08804	73.12837	1	n/a	94	Tappe et al. (2018)
-106.11242	53.39732	1	n/a	94	Tappe et al. (2018)
-79.0333	40.6667	1	n/a	89	Tappe et al. (2018)
-115.118	56.811	1	n/a	88	Tappe et al. (2018)
-92.18283	73.559	1	n/a	88	Tappe et al. (2018)
-115.72103	56.89814	1	n/a	88	Tappe et al. (2018)
-115.708484	56.815762	1	n/a	88	Tappe et al. (2018)
-115.70723	56.8158	1	n/a	87	Tappe et al. (2018)
-115.72512	56.85007	1	n/a	86	Tappe et al. (2018)
-115.658053	56.830363	1	n/a	81	Tappe et al. (2018)
-109.81582	64.78504	1	n/a	80	Tappe et al. (2018)

-112.87312	57.19045	1	n/a	77.6	Tappe et al. (2018)
-105.3011	39.9794	1	n/a	77	Tappe et al. (2018)
-113.30698	57.307	1	n/a	75.8	Tappe et al. (2018)
-117.71285	55.45415	1	n/a	75	Tappe et al. (2018)
-110.15695	64.8282	1	n/a	74.7	Tappe et al. (2018)
-109.89258	64.7037	1	n/a	74	Tappe et al. (2018)
-109.853	64.41037	1	n/a	73.9	Tappe et al. (2018)
-109.97901	64.85546	1	n/a	73	Tappe et al. (2018)
-113.04445	57.27128	1	n/a	72.6	Tappe et al. (2018)
-113.47853	57.32986	1	n/a	72.4	Tappe et al. (2018)
-109.79504	64.72735	1	n/a	72	Tappe et al. (2018)
-109.94964	64.82602	1	n/a	71	Tappe et al. (2018)
-113.47844	57.35248	1	n/a	70.9	Tappe et al. (2018)
-110.039867	70.792246	1	n/a	69.1	Tappe et al. (2018)
-110.16388	64.81908	1	n/a	68.2	Tappe et al. (2018)
-110.54142	64.6963	1	n/a	67.5	Tappe et al. (2018)
-110.66019	64.84696	1	n/a	64.1	Tappe et al. (2018)
-115.100229	56.784168	1	n/a	64	Tappe et al. (2018)
-110.910387	64.906798	1	n/a	63.9	Tappe et al. (2018)
-110.18075	64.83597	1	n/a	63.9	Tappe et al. (2018)
-110.105179	64.535788	1	n/a	61.3	Tappe et al. (2018)
-111.09908	64.64795	1	n/a	61.1	Tappe et al. (2018)
-115.846466	56.686029	1	n/a	60	Tappe et al. (2018)
-115.903407	56.659858	1	n/a	60	Tappe et al. (2018)
-110.981788	64.890201	1	n/a	59.7	Tappe et al. (2018)
-110.978715	64.895415	1	n/a	59.7	Tappe et al. (2018)
-110.2092	64.82316	1	n/a	59.5	Tappe et al. (2018)
-111.114774	64.652869	1	n/a	58.7	Tappe et al. (2018)
-110.46828	64.73994	1	n/a	58.5	Tappe et al. (2018)
-110.10473	64.549476	1	n/a	58.4	Tappe et al. (2018)
-110.538778	64.85443	1	n/a	58.3	Tappe et al. (2018)
-110.232524	64.504234	1	n/a	56	Tappe et al. (2018)
-110.172967	64.560803	1	n/a	56	Tappe et al. (2018)
-110.30897	64.717	1	n/a	56	Tappe et al. (2018)
-110.2357	64.5114	1	n/a	55.8	Tappe et al. (2018)
-110.290123	64.470622	1	n/a	55.7	Tappe et al. (2018)
-110.23556	64.49888	1	n/a	55.5	Tappe et al. (2018)
-110.222152	64.549817	1	n/a	55.3	Tappe et al. (2018)
-110.235139	64.491861	1	n/a	55.2	Tappe et al. (2018)
-110.046406	64.592467	1	n/a	54.8	Tappe et al. (2018)
-110.11896	64.73351	1	n/a	54.7	Tappe et al. (2018)
-110.59875	64.71792	1	n/a	53.3	Tappe et al. (2018)
-110.6031	64.7173	1	n/a	53.3	Tappe et al. (2018)

-110.5867	64.7352	1	n/a	53.1	Tappe et al. (2018)
-110.58425	64.72438	1	n/a	53	Tappe et al. (2018)
-110.376076	64.676697	1	n/a	52.8	Tappe et al. (2018)
-110.14136	64.58625	1	n/a	52.1	Tappe et al. (2018)
-111.51267	65.27664	1	n/a	52.1	Tappe et al. (2018)
-110.66637	64.68186	1	n/a	52	Tappe et al. (2018)
-108.5175	47.9153	1	n/a	52	Tappe et al. (2018)
-110.5051	64.78104	1	n/a	51.5	Tappe et al. (2018)
-108.4783	46.9236	1	n/a	51.4	Tappe et al. (2018)
-110.55127	64.72333	1	n/a	51.1	Tappe et al. (2018)
-108.9638	47.8888	1	n/a	51	Tappe et al. (2018)
-108.5628	46.9842	1	n/a	50.3	Tappe et al. (2018)
-108.5867	47.0075	1	n/a	50.2	Tappe et al. (2018)
-108.5714	47.0961	1	n/a	50	Tappe et al. (2018)
-110.25105	64.75179	1	n/a	48	Tappe et al. (2018)
-110.2217	47.6375	1	n/a	48	Tappe et al. (2018)
-108.6908	47.8539	1	n/a	48	Tappe et al. (2018)
-110.6556	64.7224	1	n/a	47.9	Tappe et al. (2018)
-110.12602	64.81724	1	n/a	47.8	Tappe et al. (2018)
-110.345396	64.717961	1	n/a	45.2	Tappe et al. (2018)
-76	42.5	1	n/a	136	Crough et al. (1980)
-74.5	42.9	1	n/a	146	Crough et al. (1980)
-79.5	48	1	n/a	151	Crough et al. (1980)
-97	40	1	n/a	115	Crough et al. (1980)
-96	37.7	1	n/a	90	Crough et al. (1980)
-93	34.2	1	n/a	97	Crough et al. (1980)
-108.5	48	1	n/a	45	Crough et al. (1980)
-110	37	1	n/a	31	Crough et al. (1980)

Appendix B - Comparison between the backtracked kimberlite locations using several recent kinematic models

In this appendix, we compare the backtracked kimberlite positions using three recent kinetic models, developed by Merdith et al. (2021), Young et al. (2019), and Müller et al. (2019).

The three models are built with different data and reference frames. Merdith et al. (2021) use paleomagnetic data and geologic data and a paleomagnetic reference frame. Young et al. (2019) use paleopoles and apparent polar wander paths and both paleomagnetic reference frame and a moving hotspot reference frame. Müller et al. (2019) use geological data and geophysical data and a mantle reference frame. Further descriptions about these three models are in section 3.2.

The backtracked locations computed with the model developed by Merdith et al. (2021) is displayed in Figure B.1. This model allows us to reconstruct the tectonic plate motions over the last 1,000 Ma. The oldest kimberlites emplaced over the North American continent are about 660 Ma (Faure et al., 2010). The backtracked locations computed with the model developed by Young et al. (2019) and Müller et al. (2019) are displayed in Figures B2 and B3, respectively. The kinematic model developed by Young et al. (2019) allows us to reconstruct the tectonic plate motions during the last 410 Ma, while the one developed by Müller et al. (2019) provides the motion of the tectonic plates during the last 250 m.y. only. In Figures B.2 and B.3, we retained the kimberlite ages color scale used in Figure B.1 (where the kimberlite ages vary between 0 and 660 Ma), to allow a better visual comparison between the three models.

In these three models, we can see that the backtracked kimberlite locations vary spatially. The backtracked positions of the young kimberlites (ages < 100 Ma) are located over the current-day

location of the North American plate, according to the three considered models. For ages 150-250 Ma, the backtracked locations are on the present-day location of the Eurasian plate, between the Mid-Atlantic ridge and the westernmost part of the continental Eurasian and African plates. Only one kimberlite has an age between 250 and 350 Ma. Its backtracked location falls in the present-day location of the north of Brazil, according to the models of Merdith et al. (2021) and Young et al. (2019). Müller et al. (2019) only predicts the plate motion up to 250 Ma. For ages 350-660 Ma, the backtracked kimberlites are located on the present-day locations of South America and geographical region of the Pacific Ocean. Although the three considered kinematic models do not provide the same location for the backtracked kimberlites locations, they provide a similar spatial-temporal evolution. In Chapters 4 and 5, we discuss mainly the results obtained with the model developed by Merdith et al. (2021), as it is an update of the model developed by Young et al. (2019) and Müller et al. (2019), and it allows us to go farther back in time.

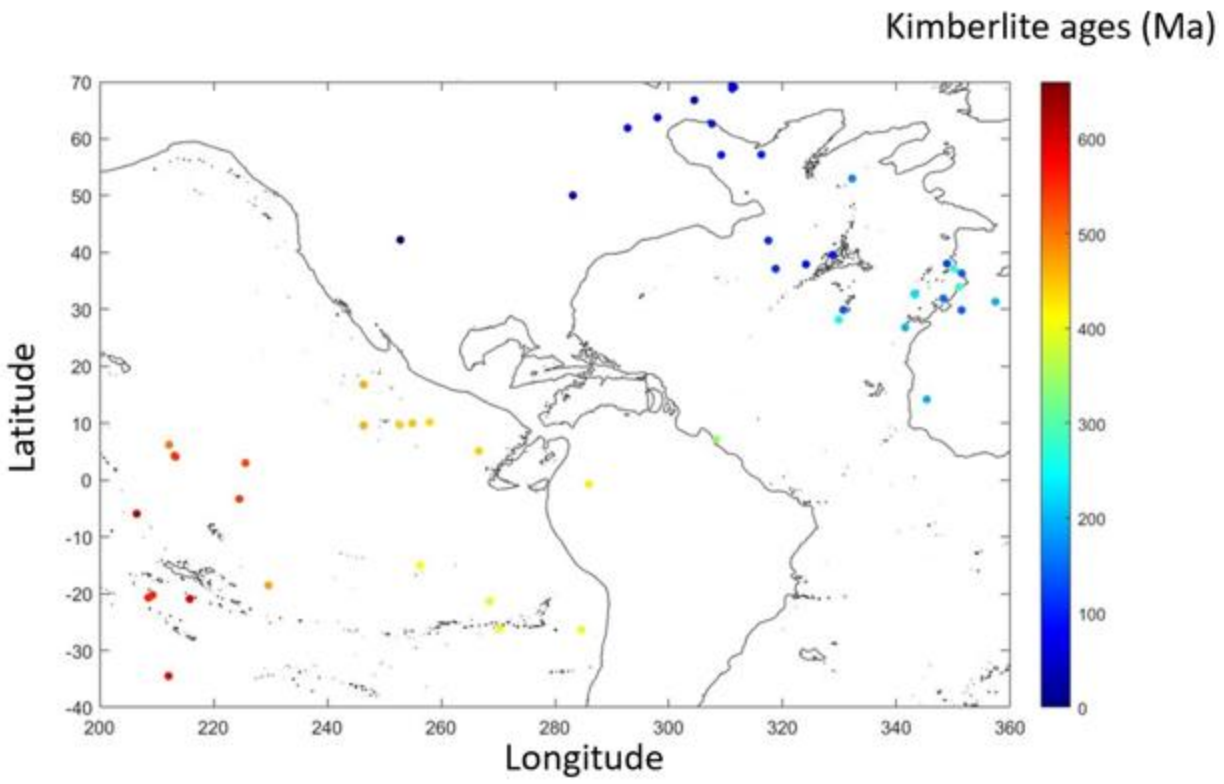

Figure B.1. Backtracked kimberlite locations computed with the rotation poles of Merdith et al. (2021).

The computation has been done with GPlates software (GPlates 2.3, EarthByte, 2021). The kimberlite ages are taken from Faure et al. (2010) and vary between 0 and 660 Ma.

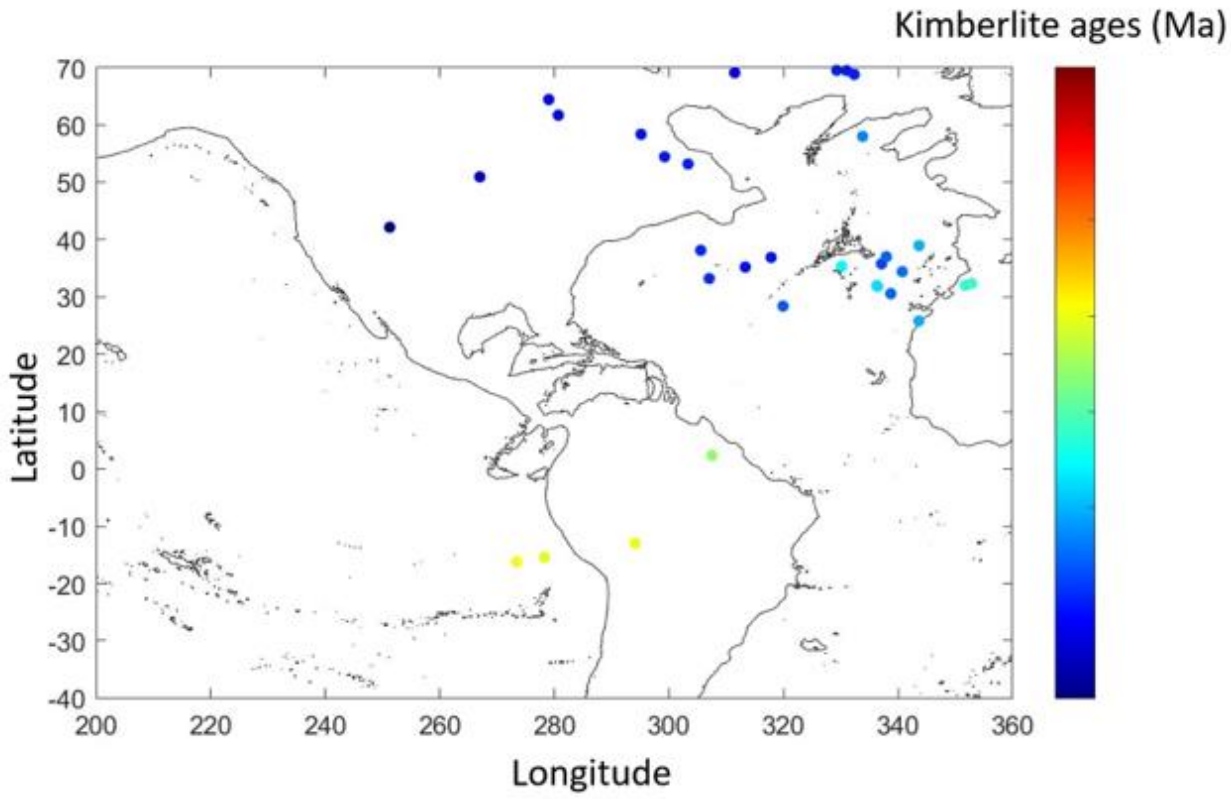

Figure B.2. Backtracked kimberlite locations computed with the rotation poles of Young et al. (2019).

The computation has been done with GPlates software (GPlates 2.3, EarthByte, 2021). The kimberlite ages are taken from Faure et al. (2010) and the kimberlite ages vary between 0 and 410 Ma. Young et al. (2019) model only allows the reconstruction for kimberlites that are 410 Ma or younger. We kept the color scale used in Figure B1 to allow an easier visual comparison between the models.

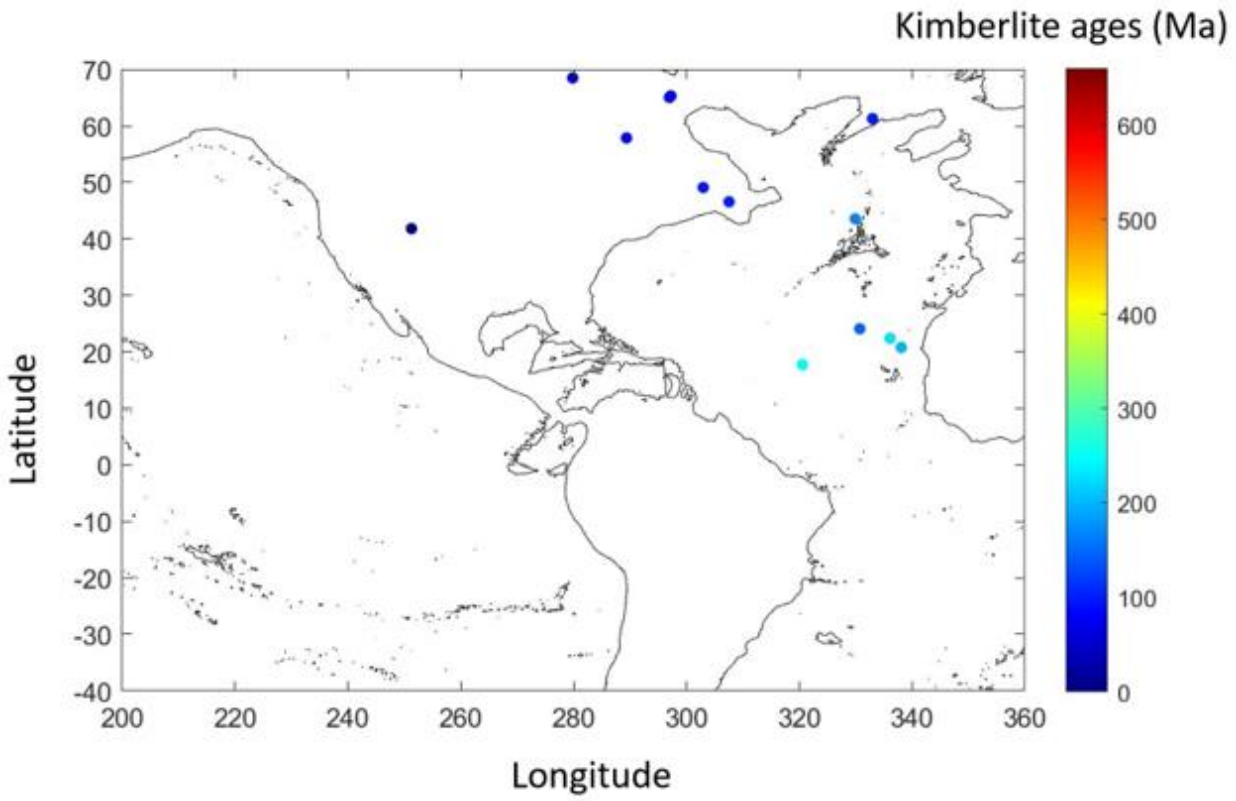

Figure B.3. Backtracked kimberlite locations computed with the rotation poles of Müller et al. (2019).

The computation has been done with GPlates software (GPlates 2.3, EarthByte, 2021). The kimberlite ages are taken from Faure et al. (2010) and the kimberlite ages vary between 0 and 410 Ma. Müller et al. (2019) model only allows the reconstruction for kimberlites that are 250 Ma or younger. We kept the color scale used in Figure B1 to allow an easier visual comparison between the models.

Appendix C - Matlab script for the seismic tomography model, SEMUCB-WM1 by French and Romanowicz (2014)

The following is a Matlab script that we developed for the seismic tomography SEMUCB-WM1 by French and Romanowicz (2014).

```
clear
close all

load C:/Users/esthe/OneDrive/Documents/backtrack2122/Tomography_check/bathymetry.mat
%   Name        Size                Bytes  Class     Attributes
%
%   bt        900x1800            6480000  single
%   xbt         1x1800              14400  double
%   ybt         1x900                7200  double
%xbt=x2; ybt=y2; bt=topo_new;
%clear x2 y2 topo_new

kimberlites=load('lon_lat_agemin_agemax.dat');
xk=kimberlites(:,1); yk=kimberlites(:,2);

% % french
load mat_french.mat
% %dT_mat      drho_mat    dvs_french  x2 y2 z2
% %z2:  -11

%vary depths
for k=20:120
%
show(:,:)=dvs_french(:,:,k);


figure(101)
contourf(x2,y2,show,50,'Linestyle','none')
colorbar
C0=([-10 10]);

caxis(C0)
toto=jet; %-> rgbs
%toto(1,:)=0.7;
%toto2=toto;
toto2=toto(end:-1:1,:);
colormap(toto2)
colorbar
hold on
plot(xk,yk,'k*')
plot(360-96.6,39.2,'ws')

axis equal
```

```
axis([220 320 0 80 ]) %swell only
title('dvs french 2013')
xlabel(z2(k)) % Esther

coef2=1e-9;
value=0;
V=[ value value]
contour(xbt,ybt,bt*coef2,V,'k','Linewidth',0.5)

pause
end
```

Appendix D - Matlab script for the LAB model, CAM2016 by Priestley et al. (2018)

The following is the Matlab script that we developed for the LAB model, CAM2016 by Priestley et al. (2018).

```
clear
close all



% Te lithos 1
%     lower_crust_top_depth2 middle_crust_bottom_depth2 middle_crust_top_depth2
upper_crust_bottom_depth2 ...
% upper_crust_top_depth2 lat lon2

%Te=lid_bottom_depth2'-lid_top_depth2';

load C:/Users/esthe/OneDrive/Documents/backtrack2122/cam2016_v2/lab.mat
%   lab          90x180            129600  double
%   lat_lab      90x1                 360  single
%   lon_lab       1x180              1440  double
%
lat=double(lat_lab);
lon2=double(lon_lab);
Te=double(lab);


% kimberlites ages from Faure 2010
C:/Users/esthe/OneDrive/Documents/Research/Matlab_data_Summer21/plots7_28_21/Faure_v4
.dat
% 1- long 2- lat 3-type 4- age min 5-age max
lonW_F=Faure_v4(:,1);
lonE_F=Faure_v4(:,1)+360;
lat_F=Faure_v4(:,2);
age_min_F=Faure_v4(:,4);
age_max_F=Faure_v4(:,5);
n=length(Faure_v4)



figure(98)
clf
contourf(lon2,lat,Te,100,'Linestyle','none')
toto=jet;
toto2=toto(end:-1:1,:);
colormap(toto2)
%tototocolormap lines added
colorbar
```

```
hold on
plot(lonE_F,lat_F,'k*')
axis equal
axis([220 320 12 83])
title('Te(km)(CAM2016)')



for ii=1:n

    vec_te(ii)=interp2(lon2,lat,Te,lonE_F(ii),lat_F(ii));

end


figure(13)
clf
plot(vec_te,age_max_F,'k*')
xlabel('Te (km)')
ylabel('age(Ma)')
```

Appendix E - Matlab script for the LAB model, LITHO1.0 by Pasyanos et al. (2014)

The following is the Matlab script that we developed for the LAB model, LITHO1.0 by Pasyanos et al. (2014).

```
clear
close all



% Te lithos 1
load C:/Users/esthe/OneDrive/Documents/backtrack2122/lith_thick/lithos1_360.mat
lid_top_depth2 lower_crust_bottom_depth2 ...
%     lower_crust_top_depth2 middle_crust_bottom_depth2 middle_crust_top_depth2
upper_crust_bottom_depth2 ...
% upper_crust_top_depth2 lat lon2

%Te=lid_bottom_depth2'-lid_top_depth2';
Te=lid_bottom_depth2';


% kimberlites ages from Faure 2010
load
C:/Users/esthe/OneDrive/Documents/backtrack2122/Matlab_data_Summer21/plots7_28_21/Fau
re_v4.dat
% 1- long 2- lat 3-type 4- age min 5-age max
lonW_F=Faure_v4(:,1);
lonE_F=Faure_v4(:,1)+360;
lat_F=Faure_v4(:,2);
age_min_F=Faure_v4(:,4);
age_max_F=Faure_v4(:,5);
n=length(Faure_v4)



figure(98)
clf
contourf(lon2,lat,Te, 100, 'Linestyle','none')
hold on
toto=jet;
toto2=toto(end:-1:1,:);
colormap(toto2)
colorbar

plot(lonE_F,lat_F,'k*')
axis equal
axis([220 320 12 83])
title('Te(km)(lithos1)')
```

```
for ii=1:n

    vec_te(ii)=interp2(lon2,lat,Te,lonE_F(ii),lat_F(ii));

end


figure(13)
clf
plot(vec_te,age_max_F,'k*')
xlabel('Te (km)')
ylabel('age(Ma)')
```

Appendix F - Matlab script for the LAB gradient according to CAM2016 model

The following is the Matlab script that we developed for the LAB gradient according to CAM2016 model by Priestley et al. (2018).

```
clear
close all

load C:/Users/esthe/OneDrive/Documents/backtrack2122/cam2016_v2/lab.mat
x2=lon_lab; y2=lat_lab; z2=1; dvs2= lab ;

[FX,FY] = gradient(lab);
nx=size(FX,2)
ny=size(FX,1)

for i=1:nx
    for j=1:ny
        var1=abs(FX(j,i));  var2=abs(FY(j,i));
        clear vec1
        vec1 =[var1 var2];
        var3 =max(vec1);
        Ftot(j,i)=var3;
    end
end


[xbt,ybt,bt]=grdread2('C:/Users/esthe/OneDrive/Documents/backtrack2122/cam2016_v2/bt_
tot_12m_v3.grd');
% kimberlites ages from Faure 2010
load
C:/Users/esthe/OneDrive/Documents/Research/Matlab_data_Summer21/plots7_28_21/Faure_v4
.dat
% 1- long 2- lat 3-type 4- age min 5-age max
lonW_F=Faure_v4(:,1);
lonE_F=Faure_v4(:,1)+360;
lat_F=Faure_v4(:,2);
age_min_F=Faure_v4(:,4);
age_max_F=Faure_v4(:,5);
n=length(Faure_v4)


clear show

show(:,:)=Ftot;
figure(112)
clf
contourf(x2,y2,show,100,'Linestyle','none')
```

```
C0=([0 20]);
caxis(C0)
toto=jet;
toto2=toto(end:-1:1,:);
colormap(toto2)
colorbar
hold on


V=[ 0 2500]
contour(xbt,ybt,bt,V,'k-','Linewidth',1)

plot(lonE_F,lat_F,'w*')

title('FXy lab CAM2016')
hold on
axis equal
axis([ 220 305 24 80 ])
```

Appendix G - Matlab script for the LAB gradient according to LITHO1.0 model

The following is the Matlab script that we developed for the LAB gradient according to LITHO1.0 model by Pasyanos et al. (2014).

```
clear
close all

load C:/Users/esthe/OneDrive/Documents/backtrack2122/lith_thick/lithos1_360.mat
x2=lon2; y2=lat; z2=lid_bottom_depth2'; dvs2=asthenospheric_mantle_top_depth2;

[FX,FY] = gradient(lid_bottom_depth2');
nx=size(FX,2)
ny=size(FX,1)

for i=1:nx
    for j=1:ny
        var1=abs(FX(j,i));  var2=abs(FY(j,i));
        clear vec1
        vec1 =[var1 var2];
        var3 =max(vec1);
        Ftot(j,i)=var3;
    end
end


[xbt,ybt,bt]=grdread2('C:/Users/esthe/OneDrive/Documents/backtrack2122/cam2016_v2/bt_
tot_12m_v3.grd');
% kimberlites ages from Faure 2010

load
C:/Users/esthe/OneDrive/Documents/Research/Matlab_data_Summer21/plots7_28_21/Faure_v4
.dat
% 1- long 2- lat 3-type 4- age min 5-age max
lonW_F=Faure_v4(:,1);
lonE_F=Faure_v4(:,1)+360;
lat_F=Faure_v4(:,2);
age_min_F=Faure_v4(:,4);
age_max_F=Faure_v4(:,5);
n=length(Faure_v4)


clear show

show(:,:)=Ftot;
figure(112)
clf
contourf(x2,y2,show,100,'Linestyle','none')
```

```
C0=([0 20]);
caxis(C0)
toto=jet;
toto2=toto(end:-1:1,:);
colormap(toto2)
colorbar
hold on


V=[ 0 2500]
contour(xbt,ybt,bt,V,'k-','Linewidth',1)

plot(lonE_F,lat_F,'w*')

title('FXy lab LITHOS1')
hold on
axis equal
axis([ 220 305 24 80 ])
```